MODELING THE INFLUENCE OF NOZZLE-GENERATED TURBULENCE ON DIESEL SPRAYS

A Dissertation
Presented to
The Academic Faculty

by

Gina M. Magnotti

In Partial Fulfillment
of the Requirements for the Degree
Doctor of Philosophy in the
Woodruff School of Mechanical Engineering

Georgia Institute of Technology
August 2017

Modeling the Influence of Nozzle-Generated Turbulence on Diesel Sprays

Approved by:

Dr. Caroline L. Genzale, Advisor
School of Mechanical Engineering
Georgia Institute of Technology

Dr. S. Mostafa Ghiaasiaan
School of Mechanical Engineering
Georgia Institute of Technology

Dr. Marc K. Smith
School of Mechanical Engineering
Georgia Institute of Technology

Dr. Donald R. Webster
School of Civil and Environmental Engineering
Georgia Institute of Technology

Dr. Sibendu Som
Energy Systems Division
Argonne National Laboratory

Date Approved: June 28, 2017

To Brandon

For his advice, patience, support, friendship and unconditional love.

ACKNOWLEDGMENTS

These past six years as a graduate student at Georgia Tech have been some of the most challenging yet rewarding experiences of my life. I am grateful to all of the people who have enriched my graduate school experience.

I would first like to thank my advisor, Dr. Caroline Genzale, for taking a chance on me in the spring of 2011 and hiring me as one of your first PhD students. Since then, I have learned a lot from you both professionally and personally. Because of your support, I have been able to take advantage of many opportunities throughout my PhD career. I hope to be able to do the same for my own students in the future.

I would also like to thank the members of my thesis committee, Prof. Mostafa Ghiaasiaan, Prof. Marc Smith, and Prof. Donald Webster, for their time and support in providing feedback on my research. Both in the classroom and in the context of my thesis, I have learned a lot from these faculty members at Georgia Tech.

I am especially grateful for the help and guidance provided by Dr. Sibendu Som from Argonne National Laboratory as both an external member of my thesis committee and mentor. I have learned so much from your probing questions regarding spray modeling results and their implications, and it is taught me how to be a better researcher and life-long learner. I would also like to acknowledge Dr. Chris Powell, Dr. Alan Kastengren, Dr. Daniel Duke and Dr. Katie Matusik from Argonne for the insight and expertise you all have shared with me about x-ray and spray diagnostics. I am also beyond thankful for the x-ray experimental data you provided that was used throughout this thesis.

A special thanks goes to Prof. Michael Brear, and his PhD students, Farzad Poursadegh and Samuel Wiseman, for hosting me at the University of Melbourne in Australia. The conversations we have had regarding computed tomography and

supercritical sprays have shaped the way I think about spray measurements. Although my time at UniMelb was short, I am so grateful for that experience.

In no particular order, I would like to thank the friends and colleagues from the Ben Zinn Combustion Lab who have enriched my life, both technically and personally: Thomas Furlong, Dr. Mike Tree, Dr. Zachary Falgout, Dr. Jackie O'Connor, Dr. Prabhakar Venkateswaran, Dr. Chris Foley, Dr. Matt Quinlan, Dr. Vishal Acharya, Aimee Williams, Hussain Zaheer, Maxwell Tannenbaum, Dr. Dorrin Jarrahbashi, Sayop Kim, Yoontak Kim, Gabrielle Martinez, and Boni Yraguen.

A special shout-out goes to Dr. Benjamin Knox, one of co-founding members of the SPhERe Lab. Thank you for providing the technical and emotional support required to get through grad school, but most of all, thank you for your friendship. And no, I am still not sorry for leaving you "stranded" at the Atlanta airport back in 2011.

Last but not least, words cannot describe how lucky I am to have the family and loved ones that I have in my life. Your love, prayers and encouragement have made all the difference. It is because of all of you that I am *where* I am today and I am *who* I am today. Thank you for everything.

TABLE OF CONTENTS

LIST OF TABLES

LIST OF FIGURES

LIST OF SYMBOLS

Abbreviations

APS Advanced Photon Source

$aTDC$ After top-dead center

$bTDC$ Before top-dead center

CAD Crank angle degree

CDM Continuum droplet model

CFD Computational fluid dynamics

DDM Discrete droplet model

DNS Direct numerical simulation

ECN Engine Combustion Network

KH Kelvin-Helmholtz

KH–ACT Kelvin-Helmholtz Aerodynamic Cavitation Turbulence

LES Large-eddy simulation

LTC Low temperature combustion

LVF Liquid volume fraction

$PDPA$ Phase-Doppler particle analysis

$PISO$ Pressure-Implicit Split Operator

$RANS$ Reynolds-Averaged Navier-Stokes

ROI Rate-of-injection

RT Rayleigh-Taylor

SMD Sauter mean diameter

SMD_i Initial Sauter mean diameter formed from turbulent breakup process

SMR Sauter mean radius

SOI Start of injection

TDC Top-dead center

TIM Transverse integrated mass

$USAXS$ Ultra-small angle x-ray scattering

XRR X-ray radiography

Greek Symbols

α_{ext} Attenuation coefficient

Δ Characteristic dimension of measurement volume

$\dot{\rho_i}^s$ Spray source term due to evaporation

$\dot{\rho}^s$ Spray source term due to evaporation

ϵ Turbulent dissipation rate

ϵ_0 Dissipation rate at the nozzle exit

κ Thermal conductivity

κ_t Turbulent thermal conductivity

Λ_{KH} Wavelength at maximum growth rate

μ_f Dynamic liquid viscosity

Ω Maximum wave growth rate

ω Growth rate

Ω_{RT} Growth rate of Rayleigh-Taylor instability wave

ρ Gas-phase density

ρ_f Liquid density

ρ_g Ambient gas density

σ Surface tension

τ Optical thickness, Viscous stress tensor

τ^+ Symmetric component of transverse τ distribution

τ^- Asymmetric component of transverse τ distribution

τ_T Reynolds stress tensor

τ_t Turbulent time scale

τ_{KH} KH characteristic breakup time

τ_{RT} Rayleigh-Taylor breakup time scale

Roman Symbols

$\bar{U}_0$ Average jet exit velocity

$\boldsymbol{F^s}$ Source term due to body forces, momentum exchange due to evaporation, and drag force exerted on the droplets

$\boldsymbol{U_d}$ Droplet velocity vector

$\boldsymbol{U_g'}$ Turbulent fluctuating component of the gas-phase velocity

$\boldsymbol{x}$ Position vector

$\dot{Q}^s$ Spray source term due to evaporation

$\mathcal{V}$ Volume of computational cell

$\mathcal{Y}$ Random number between zero and one

$\overline{\pi\, d^3/6}$ Number weighted mean droplet volume

$\overline{C_{ext}}$ Number-weighted mean extinction cross-section

$\overline{M}$ Projected density

f Droplet distribution function

a Radius of the jet

b Impact parameter

B_0 KH breakup droplet size constant

B_1 KH time constant

b_{crit} Critical impact parameter

c_f Specific heat of the liquid-phase

C_μ Model constant from standard k-ϵ turbulence model

C_{ext} Extinction cross-section

C_{RT} Rayleigh-Taylor empirical model constant

C_{sa} Empirical constant for aerodynamic enhanced breakup

C_{si} Empirical constant for droplet size at onset of breakup

D Molecular diffusivity

d_j Injector nozzle diameter

D_t Turbulent diffusivity

d_{inlet} Nozzle orifice inlet diameter

d_{outlet} Nozzle orifice outlet diameter

e Specific internal energy

e_d Internal energy of the liquid-phase

h_i Specific enthalpy of species i

I Transmitted intensity

I_o Incident intensity

I_{scat} Scattered x-ray light intensity

K Turbulent kinetic energy, Nozzle K-factor

k Wavenumber

K_0 Turbulent kinetic energy at the nozzle exit

K_c Nozzle form factor

k_{RT} Wavenumber of most unstable Rayleigh-Taylor wave

L Length of injector nozzle orifice

l_e Eddy length

l_i Characteristic length scale of droplet-forming eddy

L_t Turbulent length scale

N Number of droplets

n Number of collision events

Oh Ohnesorge number

p Pressure

$P(S)$ Probability of a given symmetry factor

P_n Probability of n collisions occurring

q X-ray scattering vector

R Specific gas constant

r Droplet radius

r_c Radius of "child" droplet

r_{RT} Rayleigh-Taylor stable droplet size

Re_f Liquid Reynolds number

S Symmetry factor

S_i Sensitivity of centerline SMD distribution to changes in parameter i

T Taylor number

T_d Droplet temperature

t_d Turbulence correlation time

T_g Ambient gas temperature

U_g Gas-phase velocity

U_{rel} Relative velocity between the liquid and gas phases

V_{liq} Liquid volume

v_{li} Radial velocity of an eddy of size l_i

We_g Gas Weber number

We_{bounce} Bouncing collision parameter

We_{coll} Collision Weber number

Y_i Mass fraction of species i

Z Compressibility factor

z Illumination path-length through droplet field

SUMMARY

Predictive engine simulations are key for rapidly exploring and optimizing the design of cleaner burning and more fuel efficient engines. Injection strategies in advanced engine concepts are resulting in the injection and atomization of fuel under a wide range of operating conditions in order to meet stringent emission regulations. However, the physics governing the breakup of an injected liquid fuel jet into droplets under these conditions have not been well studied or experimentally characterized to date. In the sprays literature, three agents have been proposed as the likely mechanisms contributing to primary atomization in diesel sprays, namely the aerodynamic growth of waves on the fuel jet surface, turbulence generated in the injector nozzle, and cavitation. If computational design tools are to be used to guide the use of direct injection strategies for cleaner and more fuel efficient engines, the physics underpinning the role of these primary atomization mechanisms must be better understood to ensure the development of predictive simulations of fuel-air mixing and vaporization within the engine. Thus, the central aim of this thesis is to improve the physical representation of spray breakup physics within today's engine simulation packages.

The work presented in this thesis investigates the role of the proposed physical mechanisms on the primary atomization process in diesel sprays. In order to advance current understanding of spray breakup, the dynamic and geometric factors contributing to cavitation were suppressed so that primary atomization due to aerodynamics and nozzle-generated turbulence could be studied in isolation. In the absence of sufficiently resolved images to visualize the primary atomization process under diesel-relevant conditions, droplet sizing spray measurements are needed to characterize the outcomes of the spray breakup process. Therefore, a new experimental methodology, called the scattering absorption measurement ratio technique, was

developed and applied in a high-pressure spray chamber to characterize the average size of droplets formed from the spray breakup process. This experimental data, in conjunction with x-ray measurements from the Advanced Photon Source at Argonne National Laboratory, have been used to assess predictions from existing spray breakup models.

Comparison between predicted and measured drop size distributions revealed that a spray atomization model, premised on droplet formation from the growth of aerodynamically induced instabilities, could capture experimentally observed sensitivities and features in the measured droplet size distributions under conventional diesel engine conditions. However, for injection into relatively lower ambient density environments, aerodynamic breakup models could not accurately predict the initial rate of droplet size decrease in the near-nozzle region, suggesting that other mechanisms, such as turbulence generated inside the nozzle, likely augment and enhance the primary breakup process.

Evaluation of newly available droplet sizing measurements under low ambient density conditions allowed for the turbulence-induced breakup process to be studied, while minimizing the influence of aerodynamic inertial forces on the spray. Although several turbulence-induced breakup models have been proposed in the literature, the scaling of droplet sizes with the integral length scale, assumed in the majority of turbulent breakup models, was found to be inconsistent with the experimentally observed trends in droplet size along the spray centerline. However, empirical correlations describing droplets formed from eddies within the inertial sub-range of the turbulence spectrum were better able to capture the measured sensitivities in droplet size to changes in ambient and injection conditions. These findings informed recommendations for an improved hybrid spray breakup model, capable of representing both aerodynamic and turbulent breakup mechanisms in the atomization of non-cavitating diesel sprays.

CHAPTER 1

INTRODUCTION

1.1 Motivation

Compression ignition engines, namely the diesel engine, have remained the preferred power source for ground-based transportation due to their high performance in terms of thermal efficiency and power output. However, due to the nature of the non-premixed combustion process where high peak temperatures and locally rich mixtures are formed, diesel engines suffer from high levels of NOx and particulate matter production. With increasingly stringent emission standards for NOx and particulate matter, currently regulated up to 12% and 2% of their 1990 levels [1], respectively, both in-cylinder combustion control strategies and aftertreatment management systems must be employed.

In order to control emissions directly within the engine combustion chamber or within the exhaust stream, fuel injection timing with respect to top dead center (TDC) has been utilized as an important tool to control fuel-air mixing and auto-ignition processes, and thereby pollutant formation. Diesel particulate aftertreatment systems often rely on post-injections late in the cycle during the expansion stroke, between 60-130 crank angle degrees (CAD) after TDC (aTDC), in order to control the thermodynamic state and chemical composition of the exhaust stream as needed to regenerate the system [2]. However, due to the added expense and complexity of these systems, in-cylinder methods have been explored to directly minimize the production of emissions. Low temperature combustion (LTC) concepts are a large class of advanced combustion strategies that leverage direct in-cylinder control of emissions. As opposed to conventional diesel operation with fuel injections near

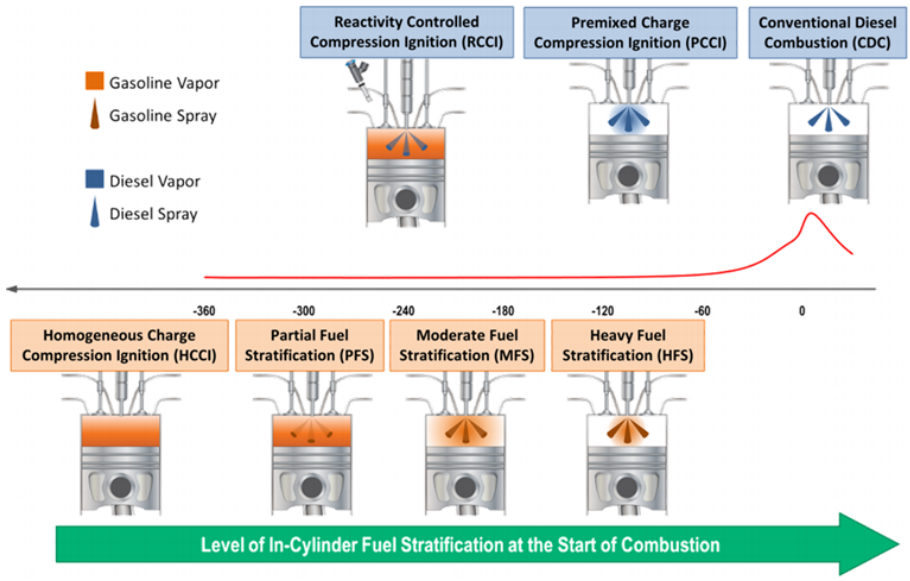

Figure 1.1: *Range of advanced compression ignition combustion strategies using gasoline and/or diesel fuel to achieve low temperature combustion [5]. Combustion strategies are ordered according to their respective fuel injection timing with respect to top dead center (0 CAD).*

TDC, LTC concepts utilize fuel injections earlier in the engine cycle, either during the intake or compression stroke between 20-300 CAD before TDC (bTDC), as shown in Figure 1.1. Controlled timing of the start of injection (SOI) with respect to TDC allows for premixing while in-cylinder temperatures are still low [3–5]. As a result, for future engines, fuel injections can be expected to occur over a wide range of conditions throughout the cycle to meet emissions regulations.

However, our understanding of the physics controlling fuel injection and spray development, and their effect on combustion and ultimately pollutant formation, has been predominantly focused under conventional diesel operating conditions near TDC, which are characterized by high temperature, T_g, and density, ρ_g, in-cylinder environments. In order to characterize the vaporization process for diesel sprays, Siebers developed a scaling law for the maximum penetration distance of liquid-phase fuel, more commonly referred to as the liquid length [6]. By applying gas jet theory to a simplified model of a fuel spray, as schematically shown in Figure 1.2, a scaling law was developed for the liquid length that accounted for the influence of injector, fuel and

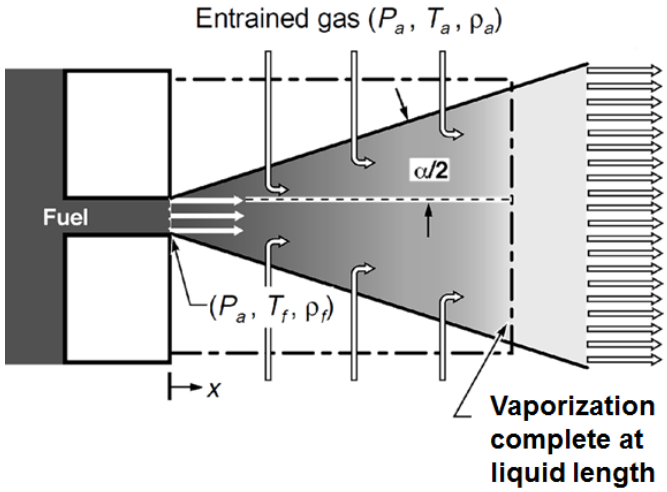

Figure 1.2: *Schematic of Sieber's dense gas jet model, modified from [6] to represent the scaling of liquid length.*

ambient conditions on vaporization. Comparison between liquid length measurements for a range of fuels, injection and in-cylinder conditions [7] and scaling law predictions revealed good agreement under conventional diesel conditions, as shown in the gray region of Figure 1.3. Because Siebers' gas jet model predictions of mixing-controlled vaporization showed good agreement with the experimental measurements for fuel injection near TDC, vaporization was convincingly hypothesized to be controlled by turbulent mixing, or entrainment, of hot ambient gases with the liquid fuel spray, as opposed to atomization or heat and mass transfer at droplet interfaces [6]. However, as the SOI is advanced or retarded with respect to TDC to conditions with relatively lower ρ_g, as shown in the yellow region of Figure 1.3, larger discrepancies are seen between Siebers' scaling law and the experimental data. One proposed hypothesis for these discrepancies is that the details of droplet breakup affect vaporization rates at low ρ_g conditions (ρ_g less than $\sim 7\,\mathrm{kg/m^3}$) [6,8]. Therefore, atomization processes may control vaporization within the range of in-cylinder conditions relevant to LTC strategies.

If computational design tools are to be used to guide the use of direct injection strategies for cleaner and more fuel efficient engines, the physics underpinning atom-

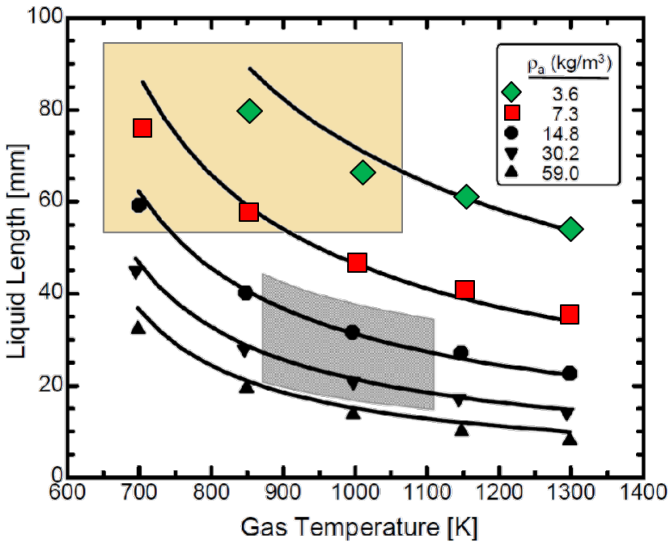

Figure 1.3: *Comparison of Sieber's dense gas jet model predictions with diesel spray liquid length measurements, modified from [6].*

ization must be better understood to ensure the development of accurate models and predictive simulations of fuel-air mixing and vaporization within the engine. However, the fuel injection and spray breakup processes for engine computational fluid dynamics (CFD) simulations are a challenging computational problem due to the multi-phase, multi-physics, and multi-scale nature of the flow. Several modeling approaches have been used to represent the liquid and gas phases and the exchange of mass, momentum and energy, but the most commonly employed method for engine simulations is the Lagrangian-Eulerian framework, as shown in Figure 1.4. In this method, the gas phase is resolved on the Eulerian grid while the liquid phase is modeled by tracking discrete parcels and their evolution using a Lagrangian formulation. Using the "blob" injection method developed by Reitz and Diwakar [9], the injection event is represented by a train of discrete injected parcels which start with a droplet size on the order of the nozzle diameter. Each computational parcel statistically represents a number of droplets, N, that share identical droplet properties (size, temperature, etc) [10]. Because the liquid phase is not directly resolved on the grid, there is a need to employ sub-models to represent the unresolved physics, such

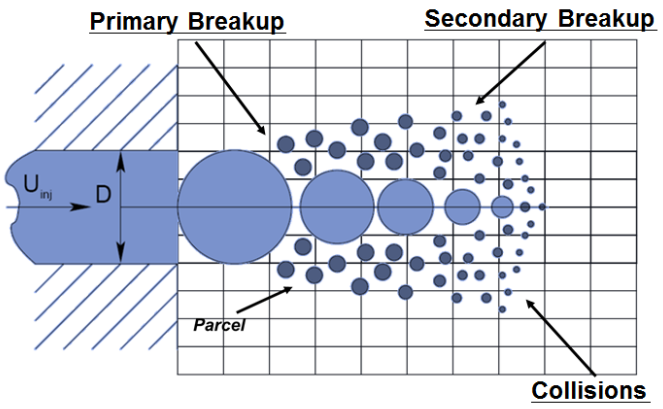

Figure 1.4: *A Lagrangian-Eulerian modeling framework is used to describe the spray formation process, where the gas phase is resolved on the grid and the liquid phase is represented with Lagrangian computational parcels.*

as primary and secondary break up, coalescence, evaporation, etc.

It is uncertain whether existing atomization and spray breakup models, historically developed to study conventional diesel operation, can be directly applied within engine CFD simulations to study and explore new advanced engine concepts. The most widely employed spray breakup model used within nearly all engine CFD codes, such as KIVA [11], Fluent [12], CONVERGE [13] and OpenFOAM [14], assumes that the growth of hydrodynamic instabilities, formed due to the velocity difference at the liquid-gas interface of a fuel spray, is the sole mechanism driving the primary breakup process [15–17]. It stands to reason that aerodynamic inertial and drag forces should strongly influence the spray breakup process when ρ_g is relatively large, as is the case for fuel injection near TDC. However, as ρ_g decreases for injections earlier in the cycle, such as those employed in advanced combustion engines, aerodynamic inertial forces are expected to decrease, bringing into question if aerodynamic-induced spray breakup should still remain the dominant mechanism. Indeed, if the fuel injection timing is sufficiently advanced such that in-cylinder ambient densities approach atmospheric conditions, recent measurements have shown that spray breakup characteristics scale with turbulence properties at the injector nozzle exit [18], suggesting that

turbulence formed within the injector may govern the spray breakup process under such conditions. Therefore, when computationally investigating injection strategies ranging from early to late cycle fuel injection timings, it seems unlikely that a spray model assuming a single breakup mechanism would be capable of yielding reliable predictions to guide design evaluation and optimization. A key premise of this thesis is that a hybrid spray breakup modeling approach, that considers the contributions of several influential breakup mechanisms for the conditions of interest, is needed for use in design evaluation and optimization. This thesis aims to re-assess the appropriateness of the physics underlying existing spray breakup models for the range of conditions relevant for current and future engine design, and determine pathways towards improving these models.

The remainder of this chapter details the physical processes that govern fuel injection and spray formation under engine-relevant conditions, and reviews previous experimental and computational investigations characterizing different primary atomization mechanisms within the sprays literature. This knowledge is then used to 1) identify existing knowledge gaps in the physical mechanisms driving spray breakup for diesel sprays and 2) serve as a foundation for the spray modeling and experimental approaches utilized in this thesis.

1.2 Background and Literature Review

The development of a spray under engine-relevant conditions, as illustrated in Figure 1.5, can be divided into four different processes: injection, spray formation and atomization, ambient entrainment, and vaporization. The order of events leading to combustion of the air-fuel mixture includes development of a turbulent, possibly cavitating, flow within the injector, primary breakup of a liquid jet into droplets, secondary breakup of droplets into smaller droplets, and simultaneous entrainment of air and vaporization of fuel until critical air-fuel ratio and temperature conditions

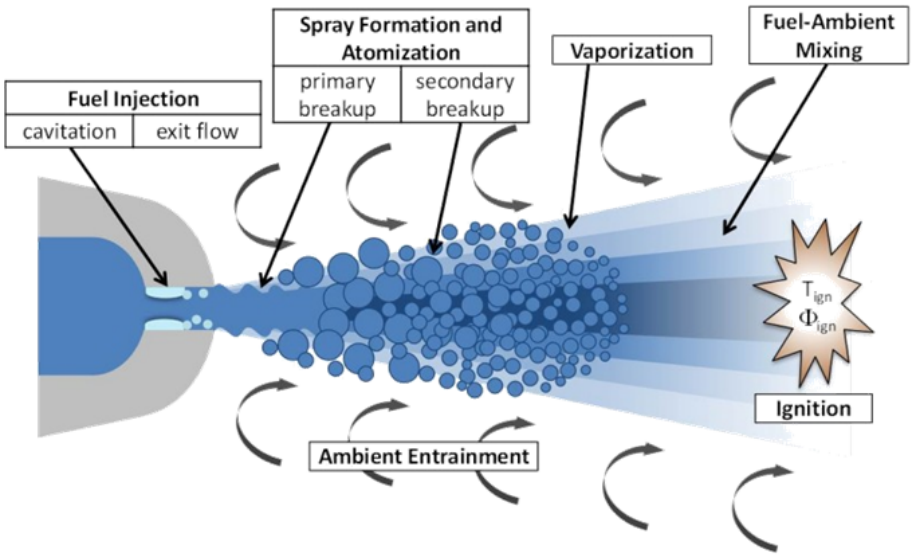

Figure 1.5: *Physical processes influencing fuel spray development in a direct injection engine-relevant environment [19].*

are achieved for ignition and combustion. The mechanisms of spray breakup are important to understand because they determine critical parameters, such as spray geometry, initial droplet size and number distribution, and serve as initial conditions for vaporization and subsequent downstream processes. However, the spray formation process is difficult to analyze both computationally and experimentally due to the multi-scale, multi-dimensional and multi-physics nature of the problem.

In order to appreciate the challenges associated with studying the spray breakup process under engine-relevant conditions, this section outlines the historical development of theoretical, computational and experimental efforts focused on the study of spray atomization. First, the theoretical basis of different physical processes believed to govern the primary breakup of a fuel spray will be presented. Next, the experimental techniques and spray measurements that have informed the fundamental basis of atomization and development of spray breakup models will be discussed. Then, commonly employed spray breakup models in current engine CFD codes will be reviewed. Finally, remaining key research questions for the formulation of a diesel spray model, capable of representing the spray formation process over a broad range of injection

and ambient conditions, will be identified.

1.2.1 Spray Breakup Theory

Current understanding of diesel spray breakup was developed from the body of research centered on the breakup of low-velocity round liquid jets [20–27]. Depending of the relative velocity of the liquid jet with respect to the ambient gas, the breakup of a liquid jet is governed by different physical mechanisms [15,28,29]. As shown in the jet breakup regime diagram developed by Reitz [29] in Figure 1.6, four main regimes of spray breakup are observed: Rayleigh, first wind-induced, second wind-induced, and atomization. In an effort to gain insight into the spray breakup process within the atomization regime, Reitz and Bracco sought a unifying theory to explain the spray breakup characteristics of the Rayleigh, first and second wind-induced regimes [15]. They hypothesized that if the aerodynamic effects are the dominant factor for the stability of a jet with a Reynolds number beyond that of the second wind-induced regime, as suggested by the experimental work by Castleman [28], then an extension of such a framework could help provide insight into the dominant forces governing breakup within the atomization regime.

Assuming that the dominant mechanism driving the spray breakup process within the Rayleigh, First and Second Wind-Induced regimes was the growth of disturbances due to hydrodynamic instabilities [30], Reitz and Bracco evaluated the linear stability of a round liquid jet issuing into a quiescent gaseous environment[16, 31]. Figure 1.7 provides a schematic of the modeled primary breakup process proposed by Reitz. The stability analysis yields a dispersion relation,

$$\omega^2 + 2\nu_f k^2 \omega F_1(ka) = \frac{\sigma k a}{\rho_f a^3} F_2(ka) + \frac{\rho_g}{\rho_f}(U-c)^2 k^2 F_3(ka) \tag{1.1}$$

which relates the growth rate, ω, of an initial linear perturbation of wavenumber $k = 2\pi/\lambda$, traveling with phase-velocity c, to jet and ambient properties. The dis-

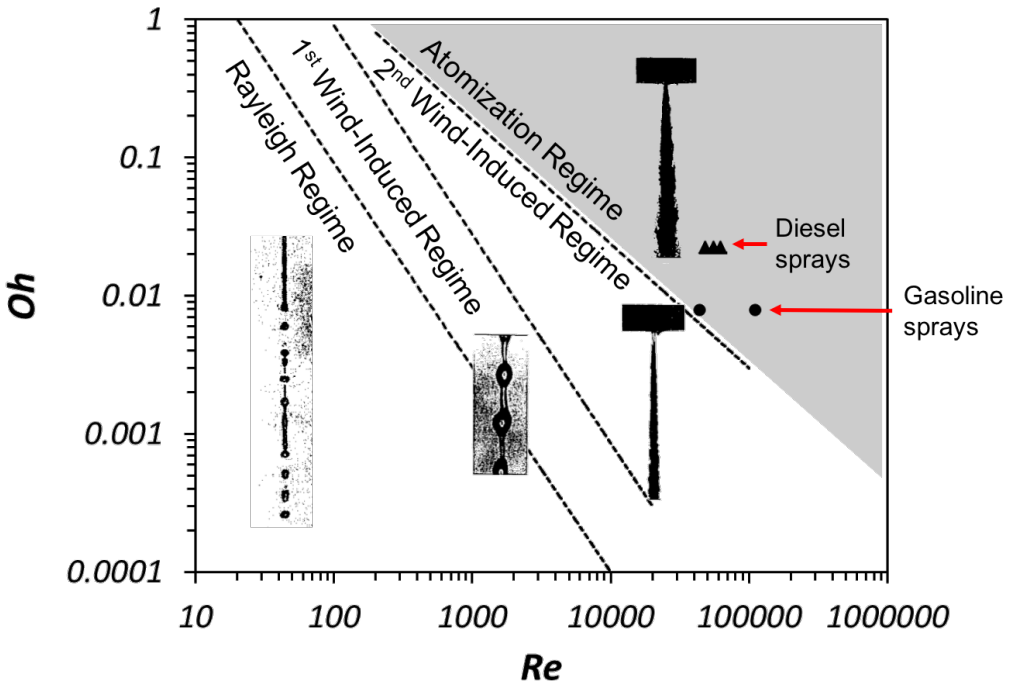

Figure 1.6: *Four main regimes of round jet breakup (adapted from [15]), namely the Rayleigh regime, the first wind-induced regime, the second wind-induced regime, and the atomization regime. Fuel sprays are characterized by high Re_f and therefore typically reside within the atomization regime.*

persion relation defines the stability of the jet in terms of non-dimensional ratios, F_i of modified Bessel functions of the first and second kind, which depend on k and the radius of the jet, a. The jet and ambient properties can be formulated in terms of non-dimensional numbers, such as the gas Weber number, We_g, liquid Reynolds number, Re_f, and Ohnesorge number, Oh,

$$We_g = \frac{\rho_g U_{rel}^2 a}{\sigma} \tag{1.2}$$

$$Oh = \frac{\sqrt{We_f}}{Re_f} = \frac{\mu_f}{\sqrt{\rho_f \sigma a}} \tag{1.3}$$

where ρ_g and ρ_f are the gas and liquid densities, respectively, U_{rel} is the relative velocity between the liquid and gas phases, σ is the surface tension, and μ_f is the

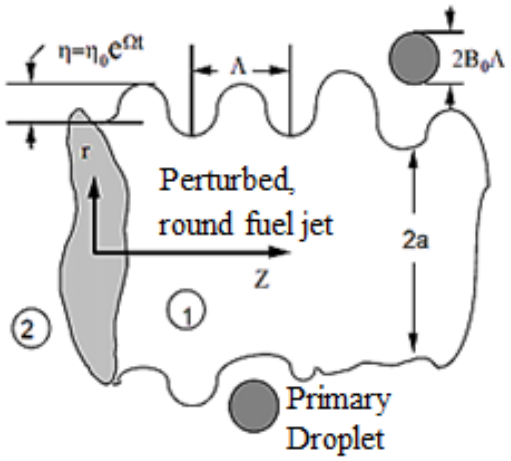

Figure 1.7: *Schematic depicting primary breakup of a liquid fuel jet due to the aerodynamic growth of waves, modified from [15].*

dynamic liquid viscosity. We_g is an indicator of the relative importance of gas inertia to surface tension, whereas Oh is an indicator of the relative importance of viscous forces to both liquid inertial and surface tension forces.

Once the stability criteria of the jet is determined from evaluation of the dispersion relation (Equation 1.1), salient characteristics of the spray can be identified for the three breakup regimes. For low velocity jets within the Rayleigh regime, as shown in Figure 1.6, a low Reynolds number jet will undergo a capillary-instability, where the destabilizing nature of the capillary pinching overcomes the stabilizing surface tension forces, and results in the formation of droplets that are larger than the diameter of the jet [15]. When the Reynolds number of the jet is increased, breakup occurs within the first wind-induced regime, as shown in Figure 1.6. Under these conditions, relative velocities between the liquid and gas phases increase to the point where aerodynamic inertial and drag forces becomes important. Growing disturbances distort the jet to form ligaments, upon which aerodynamic forces can act to form droplets on the order of the jet diameter or smaller. Further increases in the jet Reynolds number results in breakup within the second wind-induced regime, as depicted in Figure 1.6, where hydrodynamic instabilities grow on the liquid-gas interface and ultimately lead to

the formation of droplets even smaller than those produced in the first wind-induced regime. For high Reynolds number jets, such as gasoline and diesel sprays, breakup occurs within the atomization regime, as shown in Figure 1.6, and results in the formation of droplet much smaller than the jet diameter.

Within the atomization regime, conditions which are relevant for fuel sprays in direct injection engines, the dominant mechanisms driving the spray breakup process are unknown and have remained a major open question within the sprays research community. Several sources of jet breakup have been proposed, including liquid supply oscillations [32], cavitation [33, 34], velocity profile re-arrangement due to the changing boundary conditions at the nozzle exit [35–37], turbulence generated in the nozzle [38–40], and the growth of aerodynamic-induced disturbances [27, 28, 41]. To test the ability of these proposed mechanisms to characterize jet breakup in the atomization regime, Reitz performed a set of experiments to image the spray and study its response to changes in fuel viscosity, nozzle geometries, injection and ambient conditions [29]. 14 different single hole nozzles were used, each with a nozzle diameter of 340 μm but varying internal geometries, as characterized by the length-to-diameter ratio (L/d_j) and inlet radius of curvature of the nozzle, in order to evaluate a range of nozzle exit flow conditions. A sample image is shown in Figure 1.8. Due to the coarse resolution of the camera, the breakup process could not be directly imaged and evaluated. As a result, the behavior of the spray was defined using the diameter of the jet at the nozzle exit and the divergence angle of the spray.

Out of the five evaluated mechanisms, none of them were able to explain all of the experimentally observed trends. Breakup induced from liquid supply oscillations was discounted as a potential breakup mechanism because breakup of the jet was found to occur even when the liquid injection pressure was held constant. Velocity profile re-arrangement was reasoned not to be a contributing atomization mechanism because laminar nozzle exit flow conditions were found to be the most stable. However,

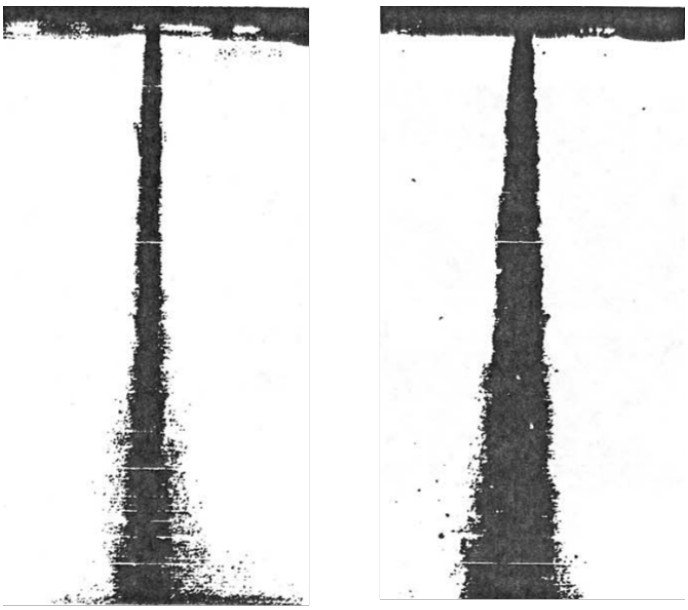

Figure 1.8: *Sample images of sprays from the seminal work by Reitz [29], detailing the influence of turbulent flow development within the nozzle on the general spray characteristics. A nozzle with fully-developed turbulent flow ($L/d_j = 85$) is shown in (a) while a nozzle with flow transitioning from laminar to turbulent ($L/d_j = 10.1$) is shown in (b).*

aerodynamic-induced breakup was able to explain the majority of the spray behavior, with the exception of nozzle geometry effects. The theoretical basis of aerodynamic-induced breakup was evaluated through comparison with the measured divergence of the spray, θ. The theoretical divergence of the spray was related to the initial flight path of a droplet formed,

$$tan\,\theta = \frac{v}{u} \tag{1.4}$$

with axial and transverse components of velocity, u and v, respectively. Using surface wave growth theory to define the droplet velocity components in terms of the growth rate and wavelength of the fasting growing wave, good agreement was achieved between the measured and predicted trends, although calibration of the model was required for every nozzle considered.

Based on the observed trends of the spray with respect to changes in nozzle L/d_j

and inlet radius of curvature, Reitz reasoned that nozzle-generated cavitation and turbulence likely augment the aerodynamic breakup process [29]. Although no single mechanism could explain all of the experimentally observed trends, a hybrid spray breakup mechanism including the influence of aerodynamics, cavitation and turbulence was thought to well describe breakup within the atomization regime.

Although the seminal work from Reitz demonstrated the likelihood of aerodynamics, turbulence and cavitation influencing the breakup process in diesel sprays, none of these mechanisms have been directly observed in diesel sprays under engine-relevant conditions. As a result, existing scalings in the literature describing aerodynamic, turbulence- and cavitation-induced breakup have only been indirectly validated through their ability within a spray simulation to predict experimentally observed trends in spray penetration [17, 42, 43], spreading angle [44, 45] and far-field droplet size distributions [31, 43, 45]. In order to improve fundamental understanding of the physics underpinning spray breakup and their appropriate scalings under diesel-relevant conditions, this thesis systematically suppresses the dynamic and geometric factors contributing to cavitation inception so that aerodynamic- and turbulence-induced breakup can be studied in isolation. Improvements to the physical representation of aerodynamic- and turbulence-driven spray atomization processes will help construct a hybrid spray breakup model, capable of representing non-cavitating diesel spray formation under a broad range of conditions expected in future engines. The remainder of this section details current understanding of the theory underpinning the aerodynamic and turbulent breakup mechanisms.

1.2.1.1 Aerodynamic Breakup

Using aerodynamic breakup theory, Reitz was able to explain many of the experimentally observed responses of the spreading of the spray to changes in fuel viscosity, injection and ambient conditions [29]. These conclusions were only possible by devel-

oping a relationship between the surface wave growth theory and the droplet formation process. Building off the work of Ranz [41], Reitz postulated that the maximum wave growth rate and the corresponding wavelength characterize the fastest growing waves on the liquid surface, and that these waves are ultimately responsible for primary breakup of the liquid jet. The size of the droplet formed during primary breakup was assumed to be proportional to the size of the fastest growing wave. To characterize the fastest growing waves, the dispersion relation defined in Equation 1.1 was solved numerically. The solutions, presented in Figure 1.9, predicted a non-dimensional wave growth rate, $\omega\sqrt{\rho_f a^3/\sigma}$ in terms of a non-dimensional wavelength, $\rho_g U_{rel}^2 \lambda/\sigma$, for a set of We_g and Oh conditions. The results indicate that there is a maximum wave growth rate, $\omega = \Omega$, which occurs at a wavelength of $\lambda = \Lambda_{KH}$. Curve fits of the numerical solutions to Equation 1.1 for the maxium growth rate, Ω, and corresponding wavelength, Λ_{KH}, were generated as functions of We for both phases, Oh and Taylor number, T, defined below:

$$\frac{\Lambda_{KH}}{a} = 9.02\frac{\left(1+0.45\sqrt{Oh}\right)\left(1+0.4T^{0.7}\right)}{\left(1+0.87We_g^{1.67}\right)^{0.6}} \tag{1.5}$$

$$\Omega\left[\frac{\rho_f a^3}{\sigma}\right]^{0.5} = \frac{\left(0.34+0.38We_g^{1.5}\right)}{\left(1+Oh\right)\left(1+1.4T^{0.6}\right)} \tag{1.6}$$

$$T = Oh\sqrt{We_g} = \frac{\mu_f U_{rel}}{\sigma}\sqrt{\frac{\rho_g}{\rho_f}} \tag{1.7}$$

where T represents the contributions of viscosity, surface tension and the relative inertia of the ambient gas and the liquid jet. For a given condition, if the relative velocity of the liquid and gas phases is known, the expected aerodynamic droplet size and breakup timescale can be determined.

The robustness of the aerodynamic wave growth theory is ultimately limited by its inability to capture geometric nozzle effects and their influence on the initial state of

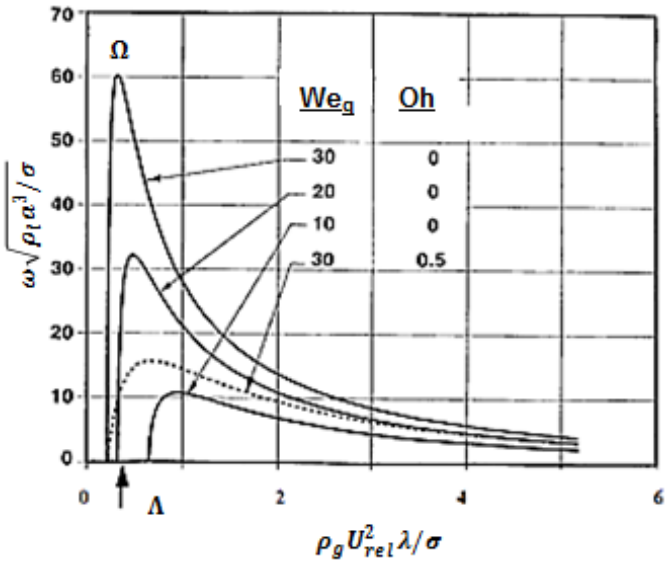

Figure 1.9: *Numerical solutions of the dispersion relation from linear stability analysis, showing the dependence of the growth rate and wavelength of the most unstable wave,* Ω *and* Λ*, respectively, on* We_g *and* Oh *[15].*

the jet as it exits the injector nozzle. In the linear stability analysis used to derive the dispersion relation in Equation 1.1, it is assumed that the jet exit conditions are single phase and laminar, and that the gas-jet interface is deformed by an infinitesimally small disturbance [15, 30]. Experimental work, such as the image of a turbulent jet shown in Figure 1.10 [46], provides evidence that mechanisms other than the growth of aerodynamic-induced instabilities are responsible for atomization. More specifically, for the conditions shown in Figure 1.10 where the water is injected into atmospheric conditions, no significant gas inertial forces are expected to act on the jet. In spite of reduced aerodynamic effects, disturbances on the surface of the jet are observed to grow that result in the formation of droplets. These results provide additional evidence that mechanisms other than aerodynamic-induced breakup can contribute to primary atomization. Out of the possible mechanisms considered by Reitz [29], turbulence generated in the nozzle is the most likely mechanism to augment the primary atomization process for non-cavitating diesel sprays. As a result, there is a need to consider how turbulence can drive the spray breakup process under the

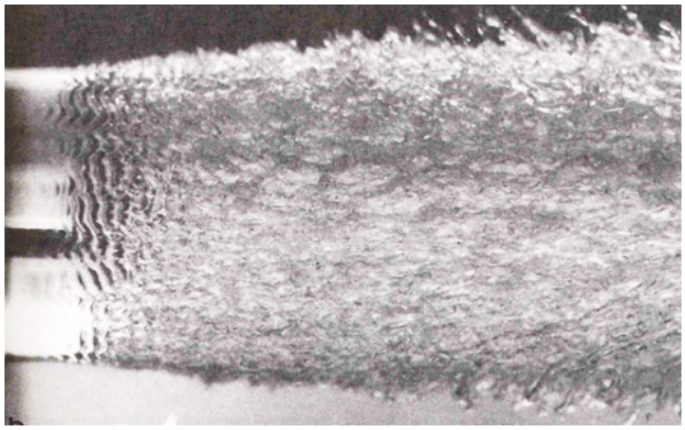

Figure 1.10: *Turbulent water jet injected into quiescent atmospheric environment [46].*

wide range of operating conditions characterizing advanced engine technologies. The predominant theories describing turbulence-induced breakup is detailed in the next section.

1.2.1.2 Turbulence-Induced Breakup

Several theories have been put forth to explain the role of nozzle-generated turbulence on the primary breakup process [18, 38–40, 47]. Schweitzer proposed that turbulence generated in the nozzle serves to augment the aerodynamic breakup process [39]. This theory was evaluated by examining images of fuel jet breakup conducted by Lee and Spencer [48], as shown in Figure 1.11, and Schweitzer [39]. Fuel was injected into evacuated and pressurized chambers across a range of Reynolds numbers ($Re_f \sim 1500 - 9000$). Schweitzer found that complete atomization of the jet could be suppressed if the spray was injected into rarefied gas or if the nozzle exit conditions of the jet were laminar. These results led to the hypothesis that the radial component in turbulent pipe flow could cause disturbances on the surface of the jet beyond the nozzle exit, which then grow according to aerodynamic wave growth. However, without sufficient spatial and temporal resolution of their imaging set-up to characterize the length and time scales of the primary atomization process, the proposed theory could not be directly validated. In spite of this, this conceptual framework forms the

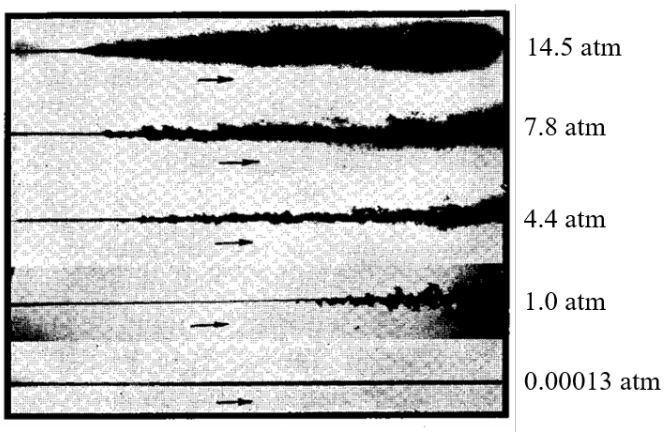

Figure 1.11: *Photographs detailing the effect of ambient pressure on fuel jet breakup, modified from Lee and Spencer [48].*

foundation for the majority of existing turbulence-induced breakup models used to study diesel spray formation, as will be discussed in further detail in Sections 1.2.3.2 and 1.2.3.3.

Due to advancements in imaging technology since the work of Schweitzer, Faeth and co-workers were able to propose and validate a phenomenological model for turbulence-driven spray atomization using pulsed shadowgraphy, as shown in Figure 1.12, and high-magnification holographic imaging [18, 47, 49, 50]. Wu and co-workers postulated that droplets formed from turbulent breakup were due to turbulent kinetic energy overcoming the surface tension energy at the liquid-gas interface. This hypothesis was tested by systematically isolating the influence of turbulence-induced breakup from other known breakup mechanisms, such as cavitation through careful design of the injection system, and aerodynamics by injecting into relatively low ambient density environments. By injecting into conditions where the liquid-to-gas density ratio (ρ_f/ρ_g) was large, the magnitude of the inertial force acting on the jet was expected to be minimized. For ρ_f/ρ_g greater than 500, aerodynamic effects were observed to be diminished and have little effect on the droplet formation process. It was hypothesized that because droplet-forming eddies only needed enough turbulent kinetic energy to surpass the surface energy present at the liquid-gas in-

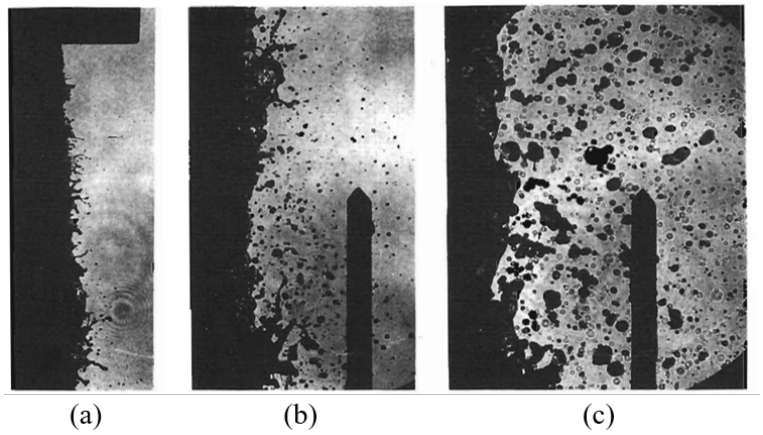

Figure 1.12: *Pulsed shadowgraphs near the liquid-gas interface of a low-velocity water jet [49] (a) at the nozzle exit and at distances of (b) 10 and (c) 50 nozzle diameters from the nozzle exit.*

terface, initially formed droplet sizes, SMD_i, should only scale with jet properties at the nozzle exit. Indeed, analysis of the experimetal images confirmed that SMD_i scaled with We_f alone [49],

$$\frac{SMD_i}{d_j} = 77We_{fd_j}^{-0.74} \tag{1.8}$$

where d_j is the injector nozzle diameter. In comparison to length scales characterizing the turbulence spectrum, SMD_i was found to be larger than estimated Kolmogorov length scales, but smaller than integral length scales. As a result, Faeth and co-workers hypothesized that because turbulent eddies formed in the injector convect downstream and dissipate energy while doing so, the reduced size of droplet-forming eddies, l_i, likely exist within the inertial sub-range of the turbulence spectrum. This hypothesis is supported by the scaling of SMD_i in Equation 1.8, which is dependent on both the dimension and velocity of the flow.

However, the size of ligaments and droplets were observed to be influenced by aerodynamic effects when the spray was injected into ρ_f/ρ_g conditions less than 500. Wu and co-workers proposed that aerodynamic effects can enhance the spray breakup process by reducing the enery required to form a droplet. As schematically represented

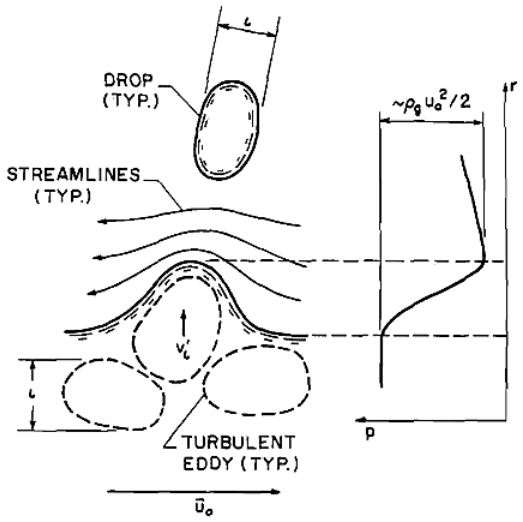

Figure 1.13: *Schematic of aerodynamically enhanced turbulence breakup, modified from [18]. The size of droplets formed are proportional to the size of the turbulent eddies, l_i.*

in Figure 1.13 [18], acceleration of gas over a ligament can reduce the local pressure, akin to flow over a sphere [51]. Faeth and co-workers modeled the enhanced aerodynamic effects as a mechanical energy, $C_{sa}\rho_g \bar{U}_0^2 l_i^3$, which together with the kinetic energy from the turbulent velocity fluctuations, $\rho_f v_{li}^2 l_i^3$, balances the surface energy, $C_{si}\sigma l_i^2$, at the instant of droplet formation, as mathematically defined below,

$$\left(\rho_f v_{li}^2 + C_{sa}\rho_g \bar{U}_0^2\right) l_i^3 = C_{si}\sigma l_i^2 \tag{1.9}$$

where v_{li} is the radial velocity of an eddy of size l_i, $\bar{U}_0$ is the average jet exit velocity, and C_{sa} and C_{si} are coefficients that incorporate the effects due to ellipticity, non-uniform pressure variation over the ligament surface and non-uniform velocities within the eddy. Even under conditions where aerodynamics augmented the spray breakup process, the size of droplet-forming eddies, l_i, were still found to scale with eddies within the inertial subrange of the turbulence spectrum.

Through evaluation of images characterizing the formation of ligaments and the resultant droplets for fully-developed turbulent jets across a wide range of liquid-to-gas density ratio ($\rho_f/\rho_g \sim 104 - 6230$), Reynolds number ($Re_f \sim 1.5 \cdot 10^5 - 5.3 \cdot 10^5$)

and Weber number ($We_f \sim 7 \cdot 10^4 - 4.1 \cdot 10^5$) conditions, three different primary breakup regimes were identified, as depicted in Figure 1.14. Non-aerodynamic primary breakup is found to occur for high ρ_f/ρ_g conditions where aerodynamic effects are suppressed, and turbulence is the only mechanism driving the formation of droplets. Transition between non-aerodynamic (turbulent) and aerodynamically enhanced primary breakup was determined to be a function of ρ_f/ρ_g alone. The critical ρ_f/ρ_g condition defining this transition was proposed to be 500, although Wu and Faeth acknowledged that more experimental work was needed to better define the breakup regime boundaries [18]. Within the aerodynamically enhanced breakup regime, turbulence is the primary mechanism governing the spray formation process, although aerodynamics serve to reduce the energy required to form droplets. As a result, smaller primary droplets are observed within this regime relative to ones formed in the non-aerodynamic regime.

For ρ_f/ρ_g conditions less than 500, Wu and Faeth hypothesized that for sufficiently large enough injection velocities, the secondary droplet breakup process would become fast enough such that the primary and secondary breakup processes would become effectively merged and indistinguishable from one another [18]. Under such conditions, the measured droplet sizes were thought to be highly influenced by aerodynamic secondary breakup processes. The transition between aerodynamically enhanced and merged aerodynamic primary and secondary breakup regimes was defined using the relative timescales of ligament formation to secondary breakup timescale ratios (τ_R/τ_b), where the critical timescale ratio was selected to be 4. In contrast to the non-aerodynamic primary breakup regime, measured droplet sizes in the aerodynamic primary and secondary breakup regime are smaller and have a strong dependence on the secondary breakup mechanism.

Although the phenomenological framework developed by Faeth and co-workers to explain the role of turbulence in the primary atomization process is strongly sup-

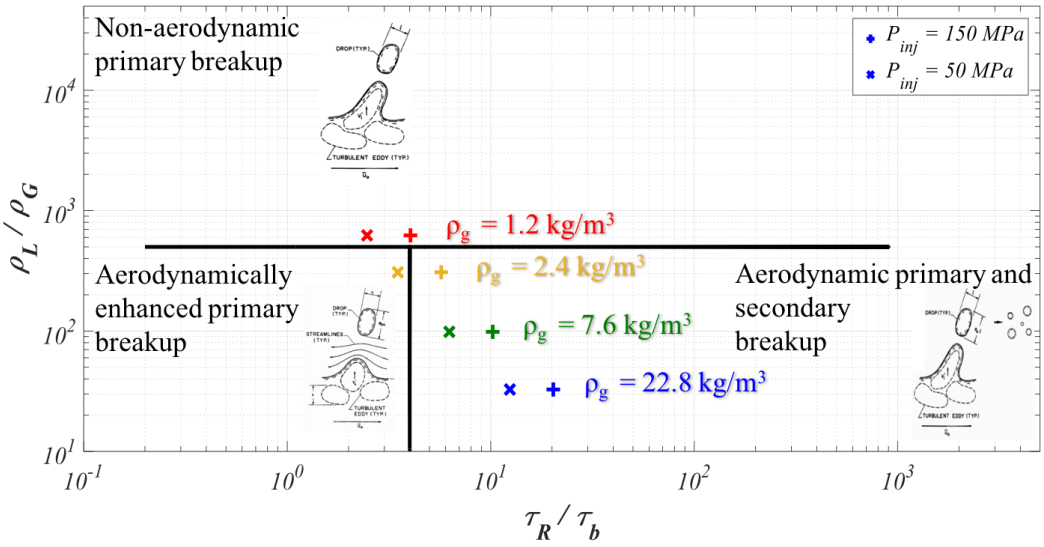

Figure 1.14: *Turbulent primary breakup regime map, adapted from the work of Faeth and co-workers [18].*

ported through comparison with direct observation and measurements, questions remain about the applicability of these findings to sprays formed from practical diesel injectors. The set of experimental data supporting their theory considers jets issued from large idealized nozzles, with nozzle diameters ranging from 3.6 - 9.5 mm and with long enough nozzle L/d_j to ensure fully developed turbulence conditions at the nozzle exit. In general, diesel injectors utilize nozzles with small diameters and short length-to-diameter ratios, typically with $d_j < 1$ mm and $L/d_j < 12$ [52]. However, results from Wu and co-workers suggest that for conditions where aerodynamic forces have a minimal influence on the spray ($\rho_f/\rho_g > 100$), the condition at the onset of turbulent breakup and the size of primary and secondary droplets were relatively independent of L/d_j [50]. Therefore, discrepancies between the L/d_j of diesel injectors and those considered by Faeth and co-workers in the development of their primary breakup regime diagram may not effect the applicability of their results to diesel sprays.

However, as noted by Dumouchel [53], divergent conclusions in the literature regarding the role of turbulence in the spray breakup process are possibly related to

the size of nozzles used in the various experimental campaigns [18, 54, 55]. Karasawa and co-workers [54] and Tamaki and co-workers [55] considered sprays formed from small nozzles ($d_j \sim 300$ μm) with high injection velocities (90 - 220 m/s). Their experimental results suggest that increasing turbulence in cavitation-free jets did not particularly promote atomization. These results directly conflict with the work of Faeth and co-workers [18, 47, 49, 50], which considered sprays formed from relatively larger nozzles ($d_j > 3.6$ mm) with slower injection velocities ($U_{inj} \sim 16 - 67$ m/s). As a result, it is still an open research question if the conclusions from Faeth and co-workers regarding the role of turbulence in the primary atomization process can be directly applied to diesel sprays.

Using the regime diagram from Wu and Faeth shown in Figure 1.14, a set of experimental conditions can be defined to explore the applicability of the theories underpinning the three primary breakup regimes to diesel sprays. Using well-characterized research-grade diesel injectors that are likely to suppress cavitation phenomena within the nozzle, a range of injection and ambient conditions can be selected to systematically explore the role of areodynamics and turbulence on the diesel spray formation process. As shown in Figure 1.14, the most influential parameters for determining the pertinent breakup regime are the ambient gas density and the fuel injection pressure. Evaluation of sprays injected into ambient densities characterizing conventional diesel conditions ($\rho_g > 7.6$ kg/m^3) could provide insight into the joint contribution of aerodynamics and turbulence on the atomization process, whereas injection into atmospheric conditions ($\rho_g \sim 1.2$ kg/m^3) would potentially enable turbulence-induced breakup to be studied in isolation. Modulation of the fuel injection pressure directly controls the injection velocity, and could enable the influence of aerodynamic secondary breakup in diesel sprays to evaluated.

In order to assess the applicability of aerodynamic- and turbulence-induced breakup theories to the broad range of conditions characterizing diesel sprays in current and

future engines, high-fidelity quantitative spray measurements, capable of characterizing spray formation, are needed. In the next section, available spray measurement and droplet sizing techniques will be discussed, along with the inherent limitations of these methods to quantify the spray breakup process under engine-relevant conditions.

1.2.2 Spray Diagnostics

The physical mechanisms governing atomization and spray formation are still largely unknown due to the difficulty in directly observing this multi-scale and multi-physics process. In order to assess the validity of applying aerodynamic and turbulent spray breakup theory to high pressure fuel sprays under engine-relevant conditions, high-fidelity quantitative spray measurements are needed. In this section, several imaging and spray measurement techniques are presented, along with the inherent limitations which prevent the direct quantification of the primary breakup process in diesel sprays.

A range of imaging techniques have been applied to sprays in order to directly image and observe global spray characteristics, as well as the initial jet breakup and droplet formation processes in sprays. For example, in the work by Reitz and Bracco [15,29], previously discussed in Section 1.2.1.1, the shadowgraph technique was used to characterize the spray and its response to changes in injection and ambient conditions, as shown in Figure 1.8. In its most rudimentary form, the shadowgraph optical configuration only requires a light source and a recording plane to detect the shadow of a given flowfield, as schematically shown in Figure 1.15 [56]. As represented in the schematic, a shadow is formed due to the refraction of incident light away from its initial undeflected path. Although this technique does not yield a quantitative description of the spray, it does provide qualitative characterization of the spray geometric features, such as the spreading angle. The images obtained from Reitz and

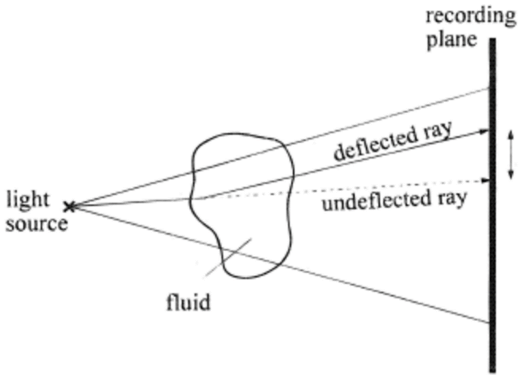

Figure 1.15: *Schematic of shadowgraph imaging technique without optical components [56].*

Bracco were limited in their spatial resolution ($\sim \mathcal{O}(100\ \mu\text{m})$) and as a result were not able to resolve features related to the primary atomization process, such as ligaments or droplets. As a result, their study was limited to indirectly relating measurable spray parameters, such as the spreading angle of the spray, to the proposed mechanisms driving the atomization process.

Since the work of Reitz and Bracco, digital camera resolution, as defined by the number of pixels in the image sensor, has increased by more than two orders of magnitude [57], resulting in significant improvements in spatial resolution capabilities. Additionally, the use of pulsed light sources, either using lasers [18] or LEDs [58, 59] has improved both the spatial and temporal resolution of imaging techniques. For example, Wu and co-workers used a pulsed ruby laser to obtain single-pulse shadowgraphs capable of resolving the primary spray breakup process in the near-nozzle region [18, 47]. A set of single-pulse shadowgraphs is shown in Figure 1.12. Feature extraction and analysis of these images enabled the quantification of the characteristic length and time scales governing the turbulent primary atomization process, as previously detailed in Section 1.2.1.2. However, the maximum injection velocity evaluated by Wu and co-workers was approximately 67 m/s [49], which is slower than typical diesel sprays traveling with convective speeds greater than 300 m/s. In general, imaging techniques are limited to slow to moderate jet speeds ($\bar{U}_0 \sim 50$–$100\,\text{m/s}$) due to

competing needs of spatio-temporal resolution and contrast required to image the ligament and droplet formation process. Utilizing a state-of-the-art high-speed camera, Zaheer found that the minimum spatial resolution of a feature traveling at a velocity of 100 m/s was roughly 3 μm or larger; for faster features on the order of 500 m/s, the resolution capabilities drop to approximately 18 μm [59]. Further development of current imaging technology is needed to improve the simultaneous temporal and spatial resolution required to resolve primary droplets produced from high pressure fuel sprays, which are on the order of 1 μm and travel with convective speeds of 300 m/s or greater.

In the absence of sufficiently resolved images to visualize spray development, droplet sizing spray measurements are needed to characterize the outcomes of the spray breakup process. However, such measurements have been generally unsuccessful in the near-nozzle region under engine-relevant conditions. For example, phase-Doppler particle analysis (PDPA) measurements [60–63], which utilize a pair of crossed laser beams to probe local droplet characteristics such as size and velocity at the crossed beam point, can provide detailed spray structure measurements that are quite valuable for spray model validation. However, sampling requirements of isolated single droplets within the probed volume make such measurements challenging in dense sprays, where droplet number densities are high, and render it incompatible for near-nozzle measurements needed to quantify primary breakup droplet sizes [60, 61]. Generally, PDPA measurements have been conducted far downstream of the nozzle exit ($x/d_j \sim 200 - 400$) and have been unable to directly characterize the near-nozzle spray formation process of interest. Additionally, measured droplet sizes from PDPA are typically much larger than those indicated from more recent near-field measurements [64, 65], suggesting that droplet coalescence may influence the measurement at these locations [62, 66], which complicates the use of such measurements for the validation of primary breakup theories.

In order to quantify details of the spray in the near-nozzle region where primary droplets are formed, alternative diagnostics to conventional imaging and droplet sizing techniques must be employed. X-ray radiography measurements [67, 68] are an absorption-based technique, which can quantify the path-integrated liquid fuel mass distribution in a spray, commonly referred to as projected density. X-rays do not scatter and therefore can "see into" denser portions of the spray than what has been possible from optical techniques. As a result, liquid mass distributions can be quantified throughout the spray, particularly in the near-nozzle region. Although x-ray radiography cannot directly quantify spray structure, as it is a joint function of droplet size and number density, it does provide unique and insightful information in regions of the spray where primary breakup is expected to occur.

While x-ray radiography measurements can provide valuable information of the liquid mass distribution in dense regions of the spray, measurements that can quantify spray structure details within the near-nozzle region are still needed to advance fundamental understanding of the primary breakup process. Recent advances of the x-ray beamline have leveraged existing projected density measurements to quantify droplet sizes using the ultra-small angle x-ray scattering (USAXS) measurement technique [64,65]. This measurement affords a unique opportunity to use the Sauter mean diameter (SMD) of droplet size distributions, particularly in the near-nozzle region, to evaluate primary breakup droplet sizes. However, it should be noted that the USAXS measurement technique is a highly specialized and resource intensive method. As a result, the amount of droplet sizing data that can be collected using this technique is limited.

A database of droplet sizing measurements, capable of guiding a comprehensive and critical assessment of existing spray model predictions, is currently missing. Therefore, two key objectives of this thesis are to 1) develop a new complementary measurement technique to USAXS and 2) use this newly available data to identify

modeling inaccuracies in existing spray models. In the next section, existing spray breakup models implemented in today's engine CFD packages are detailed. The corresponding capabilities and limitations of the various spray model predictions are noted.

1.2.3 Computational Spray Breakup Models

As previously mentioned in Section 1.1, the most commonly employed method for modeling sprays in engine simulations is the Lagrangian-Eulerian framework. Because it is not computationally feasible to directly resolve the liquid phase in the context of an engine simulation, the evolution of the spray due to primary and secondary break up, coalescence, and other processes is instead represented with physics-based sub-models. Details of the spray sub-models employed in today's engine CFD codes, as they relate to the spray atomization theory discussed previously, are presented in the next section.

1.2.3.1 Kelvin-Helmholtz (KH)

As previously mentioned in Section 1.1, The KH model is the most widely used physical model for spray atomization in engine CFD codes, and describes how the Lagrangian parcels initially change in size due to the primary breakup process [17]. The KH model was developed from the aerodynamic breakup theory from Reitz and Bracco [15], as previously detailed in Section 1.2.1.1, and is shown in Figure 1.16. The primary breakup of the injected fuel is represented in the spray model through the decrease in size of "parent" droplets, a, and formation of "child" droplets of size r_c via KH aerodynamic instabilities, as physically modeled with the following equations:

$$\frac{da}{dt} = -\frac{a - r_c}{\tau_{KH}} \tag{1.10}$$

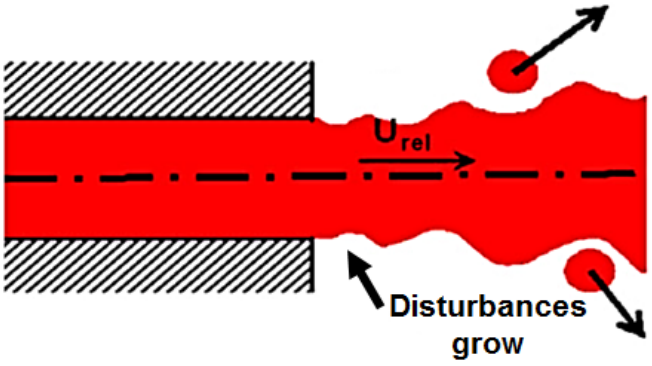

Figure 1.16: *Schematic of KH primary breakup model, modified from [42]. Disturbances grow and result in the formation of primary droplets*

$$\tau_{KH} = \frac{3.726 B_1 a}{\Lambda_{KH} \Omega} \tag{1.11}$$

$$r_c = B_0 \Lambda_{KH} \tag{1.12}$$

where τ_{KH} is the characteristic breakup time, and Ω and Λ_{KH} are the maximum growth rate and corresponding wavelength of the most unstable liquid surface wave, as numerically solved from linearized stability theory previously described in Equations (1.5) and (1.6). The primary empirical constants employed in the KH breakup model are the breakup time constant, B_1, and droplet size constant, B_0, which are typically calibrated to achieve agreement between modeled and measured liquid-phase penetration [17]. Although B_0 is typically set to a value of 0.61, a wide range of B_1 model constants have been employed with primary breakup models, from 1.76 to 40 [17, 45, 69–73] in order to improve agreement between model predictions and measured spray parameters of interest, such as spray penetration, spreading angle and far-field droplet size distributions. The need for arbitrary calibration of the KH spray breakup model to match experimental spray data highlights the failure of the model to fully capture and characterize the pertinent physics in the primary breakup process.

1.2.3.2 Huh-Gosman

In order to link the internal nozzle flow development with the primary atomization process and reduce the need for excessive tuning seen for the KH model, Huh and Gosman developed a hybrid primary breakup model that incorporated the effects of both aerodynamics and turbulence-induced instabilities [44]. This model is built on the assumption that turbulence-induced breakup is controlled by the production of large-scale turbulent fluctuations within the the injector, which create the initial disturbances on the liquid-gas interface. These disturbances then grow according to KH instabilities and ultimately control the time to form droplets, as depicted in Figure 1.17.

In contrast to the theory put forth by Faeth and co-workers [47], the turbulent fluctuations responsible for droplet formation are assumed to exist within the energy containing range of the turbulence spectrum. These fluctuations are represented using a turbulent integral scaling, which are characterized by a turbulent length scale, L_t, and time scale, τ_t,

$$L_t = C_\mu \left(\frac{K_0^{1.5}}{\epsilon_0} \right) \tag{1.13}$$

$$\tau_t = C_\mu \left(\frac{K_0}{\epsilon_0} \right) \tag{1.14}$$

where K_0 and ϵ_0 are the turbulent kinetic energy and dissipation rate at the nozzle exit, and C_μ is a model constant from the standard k-ϵ turbulence model [42,44,45,74]. Turbulence levels at the nozzle exit can be determined by predictions of turbulence levels at the nozzle exit from high-fidelity internal nozzle flow simulations [45, 75, 76]. Similar to the KH primary breakup model, the breakup of the jet is then represented in the spray model through the effective decrease in size of the "parent" drop, a, due

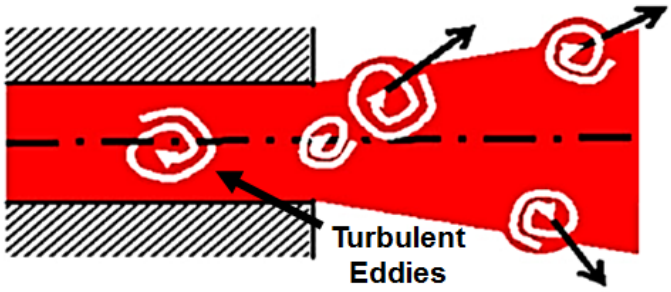

Figure 1.17: *Schematic of turbulence primary breakup model, modified from [42]. Turbulent fluctuations formed within the injector create disturbances at the liquid-gas interface, which grow and result in the formation of primary droplets*

to primary breakup as modeled below,

$$\frac{da}{dt} = k_1 \frac{L_A}{\tau_A} \tag{1.15}$$

where L_A and τ_A are the turbulent atomization length and time scales, and k_1 is the main model calibration constant. The breakup length scale, L_A, is then modeled as proportional to L_t, and occurs over a timescale, τ_A, that is a weighted sum of τ_{KH} and τ_t.

In absence of detailed internal nozzle simulations, K_0 and ϵ_0 can also be estimated using a force balance between the pressure force exerted on the fluid at the nozzle exit and turbulent stress within the nozzle, as detailed in the work of Huh and co-workers [43, 44]. An order of magnitude analysis was conducted to determine the relevant forces governing the spray atomization process. The possible candidates included surface tension, σ/d_j, gas inertia, $\rho_g U_{inj}^2$, turbulent stress in the jet, $\rho_f u_f^2$, viscous stress in the jet, $\mu_f U_{inj}/L$, viscous stress in the gas, $\mu_g U_{inj}/L$, and gravity, $\rho_f g d_j$, where L is a relevant length scale for each force and u_f and u_g are the turbulent fluctuating velocities in the jet and gas. The analysis led to the conclusion that the dominant forces acting on the jet during the atomization process are the forces due to the gas inertia ($\rho_g U_{inj}^2$) and the turbulent jet internal stress ($\rho_f u_f^2$).

The turbulent jet internal stress was estimated from a force balance,

$$\rho_f u_f^2 \pi d_j L = \Delta p_{noz} \frac{\pi d_j^2}{4} \tag{1.16}$$

that equated the resultant wall shear stress to the nozzle pressure drop, Δp_{noz}. Δp_{noz} is obtained by considering the contributions from the total pressure drop, Δp_{tot}, the form loss pressure drop, Δp_{form}, and acceleration pressure drop, Δp_{acc},

$$\Delta p_{tot} = \Delta p_{noz} + \Delta p_{form} + \Delta p_{acc} \tag{1.17}$$

The pressure loss terms are determined with the following relations,

$$\Delta p_{tot} = \frac{1}{c_d^2} \frac{\rho_f U_{inj}^2}{2} \tag{1.18}$$

$$\Delta p_{form} = K_c \frac{\rho_f U_{inj}^2}{2} \tag{1.19}$$

$$\Delta p_{acc} = (1 - s^2) \frac{\rho_f U_{inj}^2}{2} \tag{1.20}$$

where c_d is the discharge coefficient, K_c is the form factor due to the nozzle inlet radius of curvature for a fixed nozzle diameter, d_j, and s is the area ratio that accounts for the pressure loss due to flow acceleration in the contracting nozzle. Re-arrangement of Equation 1.17 results in the following expression for Δp_{noz}:

$$\Delta p_{noz} = \frac{1}{c_d^2} \frac{\rho_f U_{inj}^2}{2} - (1 - s)^2 \frac{\rho_f U_{inj}^2}{2} - K_c \frac{\rho_f U_{inj}^2}{2} \tag{1.21}$$

Substitution of Equation 1.21 and the definition of u_f into Equation 1.16 yields the

following expressions for K_0 and ϵ_0:

$$K_0 = \frac{U_{inj}}{8L/d_j}[\frac{1}{c_d^2} - K_c - (1 - s^2)] \tag{1.22}$$

$$\epsilon_0 = K_\epsilon \frac{U_{inj}^3}{2L}[\frac{1}{c_d^2} - K_c - (1 - s^2)] \tag{1.23}$$

where K_ϵ is a calibration model constant set to 0.27 [43]. These relations for K_0 and ϵ_0 can then be substituted into Equations 1.13 and 1.14 to characterize the turbulent integral length and time scales.

Although the Huh-Gosman model requires the calibration of three model constants, which control the relative contributions of turbulence and KH to the atomization time scale and the ultimate breakup rate of the spray, the implemented physics were deemed to be validated through replication of the experimentally observed trends for the spreading angle from four different nozzles [77–79]. Subsequent evaluation of the model was conducted through comparisons of predicted and measured spray tip penetration and far-field droplet size measurements along the spray centerline and periphery at distances of 40 nozzle diameters or larger from the nozzle exit [43]. Although the model was noted to predict the spray observables well, the assumed role of turbulence in the atomization process was never directly validated.

It should be noted that the assumed turbulent breakup scaling within the Huh-Gosman model is inconsistent with the body of experimental work from Faeth and co-workers [18, 47]. As noted in Section 1.2.1.2, analysis of the spray breakup images indicated that primary droplets scale with smaller turbulent length scales, more specifically those within the inertial sub-range. At the present time, it remains unclear what the appropriate turbulent scaling should be for the breakup of fuel sprays, issuing with higher injection velocities from injectors with smaller nozzles and shorter length-to-diameter ratios than considered in the experimental work from Faeth and

co-workers. This thesis will aim to shed light on the appropriate scaling of turbulent breakup by systematically controlling for aerodynamic effects on the spray breakup process and evaluating the measured spray structure as injector and ambient parameters are varied.

1.2.3.3 Kelvin-Helmholtz Aerodynamic-Cavitation-Turbulence (KH-ACT)

While the Huh-Gosman model utilizes a hybrid spray breakup approach that includes the influence of both aerodynamics and turbulence on the primary breakup process, the relative contributions of each of the mechanisms on the resultant spray was not evaluated. However, the role of the selected primary atomization model on the predicted spray metrics was extensively studied throughout the body of work conducted by Som and Aggarwal [42, 45, 74, 80]. In particular, the primary atomization process was characterized by the resultant distribution of liquid mass and droplet dispersion. Such comparisons were only possible through the use of x-ray radiography measurements, which enabled the quantification of liquid mass distributions, particularly in dense regions of the spray [67, 68], as detailed in Section 1.2.2. Through the comparison of measured and predicted liquid mass distributions at various locations in the spray, the KH model was found to underpredict droplet dispersion, as indicated by the relatively narrower mass distributions in comparison to the experimental data. The underprediction in droplet dispersion was attributed to the insufficient formation of child droplets from the primary atomization process [80]. As a result, the inclusion of additional primary atomization mechanisms, such as turbulence- and cavitation-induced breakup was motivated by the need to improve model predictions of droplet dispersion. The addition of these physics was further supported through the inability of the KH model to predict the expected trends of injector nozzle geometry on droplet dispersion [45, 80].

The KH-Aerodynamic Cavitation Turbulence (KH-ACT) model improved upon

the hybrid spray breakup formulation from the Huh-Gosman model. Because cavitation has been shown experimentally [81] and computationally [44, 74, 82] to influence the breakup process in diesel sprays, cavitation-induced breakup was included in the model. As previously mentioned, the influence of cavitation is suppressed in this thesis so that the relative contributions of the dominant mechanisms affecting diesel spray breakup, namely the growth of aerodynamic waves and nozzle-generated turbulence, can be isolated and fundamentally studied. Therefore, only the KH-ACT model improvements for aerodynamics and liquid turbulence breakup will be highlighted here.

Firstly, in the Huh-Gosman model, each parcel is assumed to have constant turbulence levels throughout the simulation. In the KH-ACT model, a standard k-ϵ turbulence model formulation is used to model the temporal evolution of turbulence levels in each parcel, $K(t)$ and $\epsilon(t)$, as it convects downstream from the nozzle exit prior to the occurrence of primary breakup. Additionally, the Huh-Gosman model assumes that the size of formed droplets is characterized by the turbulent length scale. The KH-ACT model compares and identifies the maximum breakup rate of aerodynamic and turbulence induced breakup in order to select the appropriate atomization length and time scales, L_A and τ_A, as defined below:

$$\frac{L_A}{\tau_A} = max\{\frac{a - r_c}{\tau_{KH}}, \frac{L_t(t)}{\tau_t(t)}\} \tag{1.24}$$

One final key difference is the philosophy underlying breakup. In the Huh-Gosman model, the breakup time scale is modeled as an averaged process between the two breakup mechanisms. In the KH-ACT model, it is assumed that the breakup process is ultimately determined by a single mechanism, either aerodynamics or turbulence, at each instant in time. If KH primary breakup is dominant, then the parent parcels evolve according to Equation 1.10. However, if turbulent primary breakup dominates the atomization process, then the parent parcel decreases in size according to the

following relation:

$$\frac{da}{dt} = -C_{T,CAV}\frac{L_A}{\tau_A} \tag{1.25}$$

where $C_{T,CAV}$ is the breakup rate calibration constant.

Using the hybrid spray model formulation described above, the KH-ACT model was shown to yield improved prediction of spray characteristics in comparison to the KH model across non-vaporizing, vaporizing, and combusting conditions [42, 45]. However, the KH-ACT model was only observed to produce marginal improvements over the KH model to predictions of liquid length and vapor penetration for injection into low ambient density environments (ρ_g less than 7 kg/m^3, ρ_f/ρ_g greater than 100), as shown in Figure 1.18 [42]. Although the influence of the employed primary atomization model was shown to have diminished influence on the spray formation process under vaporizing conditions [42, 45], this predicted discrepancy might suggest that the scalings employed in the turbulence model did not sufficiently enhance droplet formation and droplet dispersion. Indeed, the turbulent atomization process in the KH-ACT model is assumed to scale with the turbulence integral scaling [45]. It may be possible that the employment of a different turbulence scaling that results in the formation of smaller droplets could improve the predictive capability of the KH-ACT model under vaporizing conditions.

Droplet sizing measurements, capable of identifying inaccuracies in the selected modeling approach for turbulence-induced breakup in diesel sprays, are currently missing. Critical evaluation of the selected turbulence scaling in a given spray breakup model, and its influence on the resultant droplet size distribution, can help inform a pathway towards an improved hybrid spray breakup modeling formulation. A key aim of this thesis is to fill this existing gap in validation data and to use the insight gained from these measurements to inform the improved representation of turbulence-induced breakup in spray models.

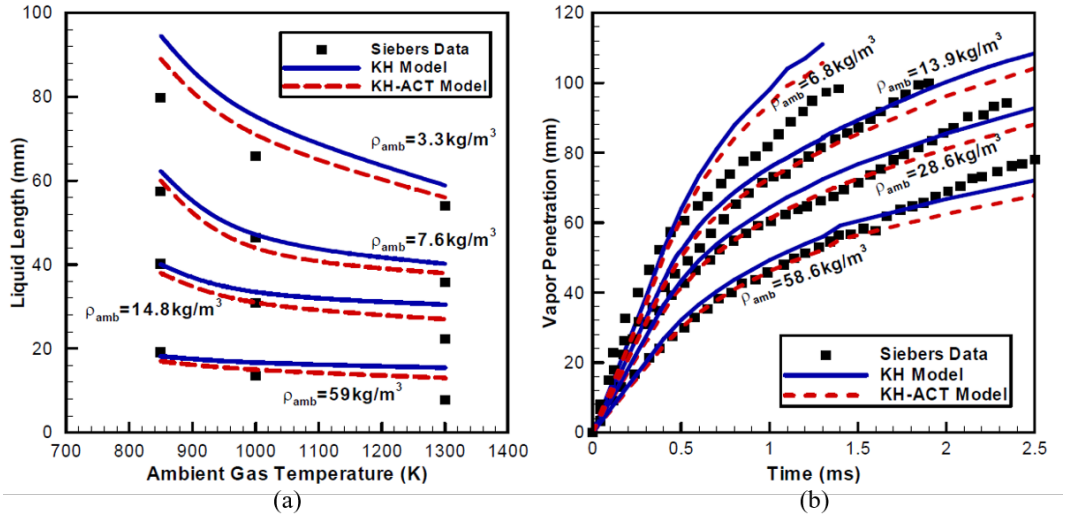

Figure 1.18: *Comparison of KH and KH-ACT model predictions against the Siebers data for (a) liquid length for a range of ambient gas temperature and density and (b) vapor penetration for a range of ambient gas densities [45].*

1.2.4 Open Research Questions

If computational design tools are to be used to guide the use of direct injection strategies for cleaner and more fuel efficient engines, the joint contributions of aerodynamics and nozzle-generated turbulence on primary atomization must be better understood to ensure accurate representation of these physics under current and future engine-relevant operating conditions. The KH model, based on aerodynamic wave growth theory, has been the most widely employed primary spray breakup model due to its success in adequately predicting trends in large-scale spray parameters, such as liquid and vapor phase penetration, under conventional diesel conditions [15, 17, 77]. However, there has been a recent push towards advancing or retarding the injection timing to help abate in-cylinder pollutant formation, to regenerate particulate aftertreatment system operation, and to enable stable operation for new direct-injection spark-ignition engines. Therefore, it is unclear how successful predictions from aerodynamic-induced breakup models will be under such conditions where the ambient density is greatly reduced and the effects due to aerodynamic

forcing on the jet are expected to be diminished. Due to the high Re_f characterizing internal nozzle flows for fuel injectors, it is expected that turbulence generated in the injector will have a relatively more pronounced effect on the spray breakup process than is expected at conventional diesel conditions.

Several questions have been unanswered by previous experimental and computational investigations regarding the manner in which turbulence augments aerodynamic breakup processes in diesel sprays.

- In the absence of sufficiently resolved images to visualize diesel spray atomization, droplet sizing measurements are needed to characterize the outcomes of the spray breakup process. However, there has been a lack of drop sizing data that can be used to study primary atomization in the near-nozzle region under diesel-relevant conditions. What measurement technique can be developed to help expand an experimental database of droplet sizing data and to assess breakup theories governing diesel sprays?

- Although application of aerodynamic breakup theory to diesel sprays in the atomization jet breakup regime has shown success in adequately predicting global spray characteristics, such as divergence angle and spray penetration, the physical processes controlling the droplet size distribution throughout the spray are still unknown. Under conventional diesel conditions, what spray and droplet phenomena control the resultant spray structure?

- As previously noted in Section 1.2.1.2, the phenomenological model developed by Wu and Faeth to describe turbulent spray breakup is based on experimental data from idealized nozzles, with long enough length-to-diameter ratios (L/d_j) to ensure fully-developed turbulence conditions at the nozzle exit. How do real-world geometry features of injector nozzles, such as relatively short L/d_j, affect the applicability of Wu and Faeth's turbulent breakup scalings to diesel sprays?

- Under what ambient and injection conditions is the diesel spray atomization process completely driven by turbulence? Within this regime, what is the appropriate scaling for the size of droplets formed from non-cavitating diesel sprays?

1.3 Research Objectives

Although it has been accepted that several mechanisms contribute to the diesel spray breakup process, namely nozzle-generated turbulence and cavitation and the aerodynamic growth of surface waves, the appropriate representation of these physics is currently unknown. To contribute to improved understanding of diesel spray breakup, this thesis focuses on aerodynamic and turbulence-driven primary atomization for non-cavitating diesel sprays so that a hybrid spray breakup model incorporating the influence of both mechanisms can be formulated. Towards this goal, a joint experimental and computational approach is employed to inform the improvement of existing spray breakup models for use in studying advanced engine concepts and future engine designs. Specific research objectives of this thesis are detailed below:

1. Derive theoretical basis for a new measurement technique capable of quantifying average droplet sizes under diesel-relevant conditions. Demonstrate ability of measurement to characterize droplet sizes through cross-validation with newly available USAXS data.

2. Utilize droplet sizing data from USAXS and newly developed measurement technique to quantitatively evaluate aerodynamic-induced breakup predictions from the KH spray model in the near-nozzle and downstream regions of the spray under conventional diesel operating conditions. Identify possible spray and droplet phenomena governing the measured spray structure.

3. Develop a new hybrid spray breakup model to investigate the influence of the assumed scaling in the turbulent primary atomization model on the predicted spray structure. This model will help provide insight into the relationship between aerodynamic and turbulent spray breakup processes, and the ability of a given spray model to match experimentally observed trends in droplet sizing measurements.

4. Identify fuel injection regimes where the influence of nozzle-generated turbulence on primary atomization can be isolated from aerodynamic effects, and length scales characterizing turbulent droplet formation can be assessed.

5. Synthesize experimental and computational findings across a broad range of injection and ambient conditions to provide recommendations for a hybrid spray breakup model for non-cavitating diesel sprays. With improved physical representation of primary atomization processes in diesel sprays, predictions of spray structure will allow for a more realistic assessment of advanced and retarded fuel injection timing strategies in future computational investigations.

CHAPTER 2

METHODS

In order to better understand the role of nozzle-generated turbulence in augmenting the aerodynamic-induced primary atomization process in diesel sprays, both computational and experimental methods are employed in this dissertation to characterize the resultant spray structure. Many of the computational and experimental methods presented in this section have been detailed in published works by the author, and are shown here for posterity [83–88].

2.1 Computational Spray Model Set-up

As previously depicted in Figure 1.5, engine simulations must be able to accurately represent a wide range of physical processes, including fuel injection and spray formation, ambient entrainment, vaporization, fuel-air mixing, ignition, and combustion chemistry. Although several modeling frameworks have been proposed, the majority of engine CFD simulations are formulated using a Lagrangian-Eulerian approach due to its computational efficiency, particularly in representing the spray processes. In this thesis, the spray modeling work is conducted using CONVERGE [13]; a sample spray computation is shown in Figure 2.1. The liquid-phase fuel is statistically represented using discrete Lagrangian computational parcels, where their evolution is tracked in space and time. The gas phase is modeled as a continuum and is resolved using an Eulerian framework on the computational grid. The governing equations and sub-models employed to describe the properties of the liquid and gas phases, and their exchange of mass, momentum and energy, are detailed in the following sections.

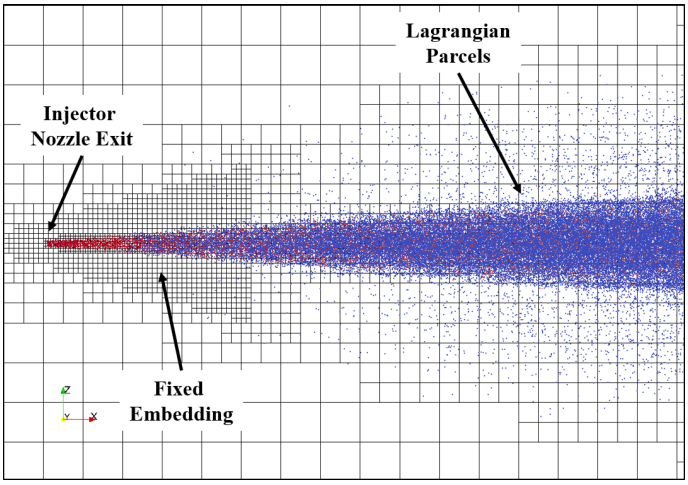

Figure 2.1: *A rendering of the Lagrangian-Eulerian spray simulation at 0.7 ms ASI using CONVERGE [13]. The Lagrangian computational parcels are colored according to the droplet diameter.*

2.1.1 Gas-Phase Governing Equations

The finite volume method is employed to solve the integral form of the governing conservation equations to calculate temporal and spatial distributions of the gas-phase properties. A non-reacting turbulent flow can be described using continuity, momentum, and energy conservation equations, along with an equation of state and a turbulence model, to characterize the gas-phase velocity, pressure, temperature, and species concentration. The conservation equations can be expressed for a multi-component compressible flow, as shown below for:

Conservation of mass:

$$\frac{\delta \rho}{\delta t} + \nabla \cdot (\rho \boldsymbol{U_g}) = \dot{\rho^s} \tag{2.1}$$

where ρ and $\boldsymbol{U_g}$ are the gas-phase density and velocity, respectively, and $\dot{\rho^s}$ is the spray source term due to evaporation of liquid-phase fuel.

Conversation of species mass fraction:

$$\frac{\delta(\rho Y_i)}{\delta t} + \nabla \cdot (\rho \boldsymbol{U_g} Y_i) = \nabla \cdot [\rho(D + D_t)\nabla Y_i] + \dot{\rho_i^s} \tag{2.2}$$

where Y_i is the mass fraction of species i, D and D_t are the molecular and turbulent diffusivities, and $\dot{\rho_i}^s$ is the spray source term due to evaporation of liquid-phase fuel.

Conservation of momentum:

$$\frac{\delta(\rho \boldsymbol{U_g})}{\delta t} + \nabla \cdot (\rho \boldsymbol{U_g} \boldsymbol{U_g}) = -\nabla p + \nabla(\tau + \tau_T) + \boldsymbol{F^s} \tag{2.3}$$

where p is the pressure, τ and τ_T are the viscous and Reynolds stress tensors, and $\boldsymbol{F^s}$ is the source term due to body forces, momentum exchange due to evaporation, and drag force exerted on the droplets.

Conservation of energy:

$$\frac{\delta \rho e}{\delta t} + \nabla \cdot (\rho \boldsymbol{U_g} e) = -p \nabla \cdot \boldsymbol{U_g} + \nabla \cdot [(\kappa + \kappa_t) \nabla T_g] + (\tau \cdot \nabla) \boldsymbol{U_g} + \nabla \cdot (\rho D h_i \nabla Y_i) + \dot{Q}^s \tag{2.4}$$

where e is the specific internal energy, κ and κ_t are the laminar and turbulent thermal conductivities, h_i is the specific enthalpy of species i, and $\dot{Q}^s$ is the spray source term due to evaporation of liquid-phase fuel. To completely characterize the gas-phase properties, an equation of state and a turbulence model are needed. In this work, the ideal gas law is employed to describe the equation of state for the gas-phase,

$$p = Z \, \rho \, R \, T_g \tag{2.5}$$

where Z is the compressibility factor, which equals unity for an ideal gas, and R is the specific gas constant.

Because direct numerical simulation (DNS) is not practical for resolving the wide range of length and time scales characterizing the gas-phase flow field in spray and engine simulations [89, 90], models are needed to account for the effect of turbulence on the momentum and energy transport. The smallest scale in the flowfield that would need to be resolved is the Kolmogorov length scale, η, which can be defined as

follows [91]

$$\eta = \left(\frac{\nu^3}{\epsilon}\right)^{1/4} \tag{2.6}$$

where ν is the kinematic viscosity of the gas and ϵ is the turbulent dissipation rate. For typical engine simulations, the smallest scales are on the order of $1 - 10$ μm [90], which are not possible to resolve using practical grid resolution for engine simulations (0.1-1.0 mm). As a result, large-eddy simulations (LES) or Reynolds-Averaged Navier Stokes (RANS) formulations are required to model these scales.

LES approaches calculate the instantaneous flow field by resolving flow structures on the grid and modeling scales smaller than the computational cell size [91, 92]. Due to smaller dissipation in the LES turbulence model, more flow structures and eddies can be resolved in comparison to the RANS approach. Depending on the formulation, some LES approaches are also able to resolve a larger range of scales by employing finer grid resolution [93]. Although LES spray simulations can offer insight into the temporal evolution and variability of the gas-phase flow field and relative velocity of the spray, direct comparison with experiments present a challenge. The experimental measurements utilized in this work are ensemble-averaged quantities that have been determined over the course of many spray injection events (30-64 total injections [86, 94]). In order to validate LES spray predictions, up to 28-30 realizations may be required to obtain statistically significant results [95, 96], which would result in prohibitively expensive computational costs for the large range of conditions that are of interest in this thesis.

The RANS approach therefore allows for a direct and computationally efficient manner to compare spray model predictions with ensemble-averaged experimental measurements. RANS approaches model all scales of the flow-field, and yield predictions for the ensemble-averaged mean quantities. The influence of turbulence on the transport of momentum can be represented as an additional viscous stress term, τ_T,

using the Boussinesq approximation,

$$\tau_T = \frac{1}{2}\mu_t(\nabla \boldsymbol{U_g} + \nabla \boldsymbol{U_g}^T) - \frac{2}{3}\rho K \boldsymbol{I} \tag{2.7}$$

where K is the turbulent kinetic energy, $\boldsymbol{I}$ is the identity matrix, and μ_t is the turbulent eddy viscosity,

$$\mu_t = C_\mu \rho \frac{K^2}{\epsilon} \tag{2.8}$$

where C_μ is a turbulence model constant. In order to characterize the evolution of turbulence properties, transport relations for K and ϵ are required. The standard k-ϵ turbulence model is a two-equation model that describes the transport of K and ϵ, and has been widely employed to model the turbulent flow induced by the spray in Reynolds-Averaged Navier-Stokes (RANS) simulations [75, 83, 97]. As a result, the gas-phase flow field is described using the RANS equations with the standard k-ϵ turbulence model using a turbulence round jet-correction [98], and solved with a Pressure Implicit with Split Operator (PISO) algorithm to treat the pressure-velocity coupling [13].

As previously noted, there are source terms in each of the conservation equations to account for the exchange of mass, momentum and energy between the gas and liquid phases. The next section details the governing equations describing the properties of the liquid-phase, and models to represent the various source terms.

2.1.2 Liquid-Phase Governing Equations

Resolving liquid-fuel injection and subsequent development of the spray under engine-relevant conditions is a challenging computational problem. Typical diesel sprays form droplets on the order of 10 μm or less [64]. A first order approximation for the number of fuel droplets formed from a spray can be obtained by assuming that the initial

droplet size is on the order of the diameter of the injector nozzle ($\sim \mathcal{O}(1\text{ mm})$), and breaks up into a monodisperse droplet distribution with a diameter of 10 μm. This simple calculation provides an estimate of approximately 10^6 droplets formed from the primary breakup process. As these droplets collide and breakup, the total number of droplets would increase further, and the tracking of each individual droplet would become prohibitively expensive with respect to required computational resources.

In order to address this issue, Amsden and co-workers [11] applied a statistical approach to the Lagrangian framework [10] to represent the evolution of droplets formed from the spray using a droplet distribution function, f [99]. f represents the probable number of droplets per unit volume at a given instant in time, t, position in space $\boldsymbol{x}$ in the volume interval $d\boldsymbol{x}$, with velocities in the range of $\boldsymbol{U_d} \pm d\boldsymbol{U_d}$, droplet radii in the range of $r \pm dr$, temperature in the range of $T_d \pm dT_d$, and non-dimensionalized droplet distortion displacements and oscillation velocities in the range of $y \pm dy$ and $\dot{y} \pm d\dot{y}$, respectively. The evolution of f can be described using the following differential equation, also known as the spray equation [99],

$$\begin{aligned}\frac{\partial f}{\partial t} + \frac{\partial}{\partial \boldsymbol{x}} \cdot (f\boldsymbol{U_d}) + \frac{\partial}{\partial \boldsymbol{U_d}} \cdot (f\frac{\partial \boldsymbol{U_d}}{\partial t}) + \frac{\partial}{\partial T_d}(f\frac{\partial T_d}{\partial t}) \\ + \frac{\partial}{\partial r}(f\frac{\partial r}{\partial t}) + \frac{\partial}{\partial y}(f\dot{y}) + \frac{\partial}{\partial \dot{y}}(f\ddot{y}) = \dot{f}_{collision} + \dot{f}_{breakup}\end{aligned} \tag{2.9}$$

where $\dot{f}_{collision}$ and $\dot{f}_{breakup}$ are source terms to account for droplet collisions and breakup.

The solution of Equation 2.9, coupled with the governing equations for the gas-phase, allows for the interaction between the spray and the gaseous environment to be modeled. Using the continuum droplet model (CDM) approach [100], Equation 2.9 can be directly solved by discretizing f into 11 dimensions (t, $\boldsymbol{x}$, $\boldsymbol{U_g}$, r, T_d, y, and $\dot{y}$). However, the resolution required in each dimension for most practical spray applications would result in excessive requirements for computational memory and resources, therefore rendering the CDM approach impractical for diesel spray simulations. A

more computationally efficient approach that has become the standard method in engine simulations is the discrete droplet model (DDM), where the the spray equation is solved using a Monte Carlo method [10]. With this approach, the spray is statistically described by a large number of stochastic computational parcels, which represent N droplets of identical r, T_d, $\boldsymbol{U_d}$, y, and $\dot{y}$. Due to the statistical nature of this approach, N need not equal an integer as there is not a direct physical analogy between computational parcels and actual droplets in the spray [101].

Although the Lagrangian-Eulerian formulation allows for a computationally efficient method to simulate diesel sprays, it should be noted that spray predictions have been known to suffer from grid dependencies. This dependency stems from the modeling of the liquid-gas coupling and interactions, which considers average gas flow properties over the scale of the local computational cell. Because the scale of the computational cell is often much larger than the size of the droplets represented in a given computational parcel, predicted relative velocities between the two phases can substantially differ from the actual local relative velocity at the droplet-gas interface. The largest deviations in predicted relative droplet velocities are expected in the near-nozzle region, where steep gradients in the gas-phase velocity occur.

For the computational work presented in this thesis, the influence of the grid on the spray predictions is minimized through several methods, based on best practices outlined by Senecal and co-workers [102]. First, careful design of the computational mesh can ensure adequate spatial resolution for resolving the gas-phase flow field, particularly through the use of fixed embedding and adaptive mesh refinement [13], as shown in Figure 2.1. Injection into a mesh with such fine grid resolution in the near-nozzle region requires sufficient injection of computational parcels to achieve statistical convergence [102–104]. In this work, injection of 750k computational parcels into a domain with a minimum grid size of 125 μm in the near-nozzle region yielded grid and statistically convergent spray predictions [83]. Additionally, improved liquid-

gas coupling can be achieved by calculating $\boldsymbol{U_g}$ at the parcel location through a Taylor series expansion, as opposed to estimation of $\boldsymbol{U_g}$ at the nearest node of the computational grid [102]. It has also been noted that some types of fuel injection source models can be more sensititive to details of the mesh than others [104]. For example, injection from a point-source effectively represents a delta function source term of mass and momentum at the location of the injector nozzle exit [11], which cannot lead to grid convergent results no matter how small the mesh is refined. As a result, parcels are injected within a circle instead [13, 102], where the diameter of the circle is set equal to the diameter of the injector nozzle.

2.1.2.1 Spray Source Terms

The solution for f in Equation 2.9 using the DDM approach allows for the spray source terms in the gas-phase conservation equations (Equations 2.1- 2.4) to be determined. The spray source term in Equation 2.1 accounting for evaporation of liquid-phase fuel is defined as

$$\dot{\rho}^s = -\int 4\pi\,\rho_f\,f\,r^2\,\frac{\delta r}{\delta t}\,d\boldsymbol{U_d}\,dr\,dT_d\,dy\,d\dot{y}. \tag{2.10}$$

The spray source term in Equation 2.2 follows a similar form as Equation 2.10, except ρ_f is replaced with the density of species i, ρ_i. The spray source term in Equation 2.3 accounting for the rate of momentum gain due to droplet drag, body forces and evaporation is defined as

$$\rho_g F^s = -\int f\rho_f[\frac{4}{3}\pi\,r^3\,(\frac{d\boldsymbol{U_d}}{dt}\,-\,\boldsymbol{g})\,+\,4\pi\,r^2\,\frac{dr}{dt}\,\boldsymbol{U_d}]\,d\boldsymbol{U_d}\,dr\,dT_d\,dy\,d\dot{y}. \tag{2.11}$$

The spray source term in Equation 2.4 accounting for energy transfer between the droplets and gas-phase due to evaporation, heat transfer into the droplet, and work

due to turbulent fluctuations is defined as

$$\begin{aligned}\dot{Q}^s = & -\int f\rho_f\{4\pi\, r^2\, \frac{dr}{dt}\,[e_d + \frac{1}{2}(\boldsymbol{U_d} - \boldsymbol{U_g})^2] \\ & + \frac{4}{3}\pi\, r^3\,[c_f\, \frac{dT_d}{dt} + (\frac{d\boldsymbol{U_d}}{dt} - \boldsymbol{g})(\boldsymbol{U_d} - \boldsymbol{U_g} - \boldsymbol{U_g'})\,]\,\}\, d\boldsymbol{U_d}\, dr\, dT_d\, dy\, d\dot{y},\end{aligned} \tag{2.12}$$

where c_f and e_d are the specific heat and internal energy for the liquid droplets, and $\boldsymbol{U_g'}$ is the turbulent fluctuating component of the gas velocity. $\boldsymbol{U_g'}$ is modeled using the O'Rourke turbulent dispersion model [105], which is discussed in further detail in Section 2.1.2.2.

2.1.2.2 Droplet Kinematics

The trajectory of a given droplet within an interval of time, dt, can be defined as follows

$$\frac{d}{dt}\boldsymbol{x} = \boldsymbol{U_d}, \tag{2.13}$$

where the change in droplet velocity over time is determined from

$$\frac{d}{dt}\boldsymbol{U_d} = \boldsymbol{F}, \tag{2.14}$$

where the specific force $\boldsymbol{F}$ acting on the droplet is the result of both gravitational and drag forces. In this work, the drag force is determined using the dynamic droplet drag model [105], which is dependent on r, U_d, y, and $\dot{y}$, as well as $\boldsymbol{U_g}$ and the turbulent fluctuating component of the gas-phase velocity, $\boldsymbol{U_g'}$.

The trajectory of droplets is also influenced by turbulent flow structures in the gas-phase. This influence is represented in the spray model through the application of a turbulent dispersion model, where $\boldsymbol{U_g'}$ is defined with a given probability distribution function. For the spray modeling results presented in this thesis, the turbulent

dispersion is described using the O'Rourke model [11], where each component of $\boldsymbol{U_g^{'}}$, $U_{g,i}^{'}$, is sampled from a Gaussian distribution given by

$$G(U_{g,i}^{'}) = \frac{1}{\sqrt{2\pi\sigma}} exp(\frac{-(U_{g,i})^2}{2\sigma^2}), \tag{2.15}$$

with a variance $\sigma^2 = 2/3K$. $\boldsymbol{U_g^{'}}$ is updated every turbulence correlation time, t_d,

$$t_d = min(\frac{K}{\epsilon}\,,\, \frac{l_e}{|\boldsymbol{U_g} + \boldsymbol{U_g^{'}} - \boldsymbol{U_d}|}), \tag{2.16}$$

which is the lesser of the eddy breakup time (K/ϵ) and time for a droplet to traverse an eddy of length, l_e,

$$l_e = c_\mu^{3/4} \frac{K^{3/2}}{\epsilon}. \tag{2.17}$$

2.1.2.3 Spray Sub-models

Because the liquid-phase and its interface are not directly resolved, there is a need to employ sub-models to represent the wide range of spray processes depicted in Figure 1.5. Prior to breaking up and forming the initial droplets via primary atomization, the liquid-phase fuel is injected as a continuous liquid jet. The continous liquid jet is modeled in this computational framework using the "blob" injection model developed by Reitz and Diwakar [29], whereby the liquid core is represented by a train of discrete injected parcels which start with d equal to d_j.

After the computational parcel is injected into the domain, the droplets begin to decrease in size due to primary atomization. For a non-cavitating injector, there are two dominant mechanisms that are believed to drive the primary atomization process: aerodynamic-induced instabilities at the liquid-gas interface and turbulence-induced disturbances within the injector nozzle, as previously described in Section 1.2.1. Two existing primary atomization models from the literature that represent the formation

of "child" parcels are the KH and KH-ACT models, where the KH model accounts for aerodynamic-induced breakup, and the KH-ACT model accounts for the competition between aerodynamic- and turbulence-induced breakup on the formation of child droplets. The physics and governing equations underpinning the KH and KH-ACT models were previously detailed in Sections 1.2.3.1 and 1.2.3.3, respectively. Both of these models are employed in this work to identify the capabilities and deficiencies in current spray modeling approaches through their ability to capture experimentally observed responses to spray parameters, such as spray penetration, dispersion, and liquid-mass and droplet size distribution.

Child droplets formed from the primary atomization process may continue to decrease in size due to secondary droplet breakup. Secondary droplet breakup is modeled using the hybrid model which considers the competition between the growth of KH and Rayleigh-Taylor (RT) instabilities on the surface of child droplets [17]. In this work, a breakup length is not employed in order to reduce the number of spray model tuning parameters [74]. As a result, the competition between the KH and RT breakup models act on child droplets at all locations in the spray. The formation of secondary droplets in the RT model is governed by the following equations:

$$\tau_{RT} = \frac{1}{\Omega_{RT}} \tag{2.18}$$

$$r_{RT} = \pi \frac{C_{RT}}{k_{RT}} \tag{2.19}$$

where r_{RT} is the stable droplet size created via RT breakup after a characteristic secondary breakup time scale τ_{RT}, Ω_{RT} is the growth rate of the unstable liquid surface wave with wavenumber k_{RT}, and C_{RT} is the primary empirical constant employed in the RT model. Increasing C_{RT} serves to create larger secondary droplets. The RT secondary breakup model, and its applicability to representing diesel sprays, is

investigated in further detail in Chapter 4.

Droplets within the spray may also change in size due to interactions with other droplets via collisions. In dense regions of the spray, particularly in the near nozzle region, collisions are thought to be more likely to occur due to the relatively short distances between the droplets [106–108]. Further downstream as the spray entrains ambient gases and becomes more dilute, the occurrence of collisions becomes less probable. It is currently not known if droplet collisions govern the ultimate size of droplets in a diesel spray, and if these physics should be included in a spray simulation [86]. To investigate the appropriateness of including the influence of droplet collisions on the resultant spray strucuture, the widely-used O'Rourke droplet collision model [107], with Post outcomes [109], is employed. The probability of two droplets of size r_1 and r_2 colliding n times in the same computational cell of volume $\mathcal{V}$ is assumed to follow a Poisson distribution,

$$P_n = e^{-\bar{n}} \frac{\bar{n}^n}{n!}, \tag{2.20}$$

with a mean value $\bar{n}$ defined as

$$\bar{n} = \frac{N_2 \, \pi \, (r_1 \, + \, r_2)^2 \, |U_{d,1} - U_{d,2}| \, dt}{\mathcal{V}}, \tag{2.21}$$

where N_2 is the number of drops in the droplet parcel, and $|U_{d,1} - U_{d,2}|$ is the relative velocity between the two droplets. It then follows that the probability of no collisions occurring ($n \, = \, 0$) between the two droplets is given by

$$P_0 = e^{-\bar{n}}. \tag{2.22}$$

In the O'Rourke collision model, a random number is selected between zero and one to determine if a collision occurs. If the random number is less than P_0, then no collisions occur. However, if the random number is larger than P_0, then a collision

event occurs. If a collision occurs, then the collision outcome must be determined. Using the collision outcome model by Post and Abraham [109], the outcome is evaluated by first comparing the collision Weber number We_{coll} based on droplet diameter ($2We_{coll}$) given by

$$We_{coll} = \frac{\rho_f \left| U_{d,1} - U_{d,2} \right| r_2}{\sigma} \tag{2.23}$$

to the bouncing parameter, We_{bounce} [109]. If $2We_{coll}$ is smaller than We_{bounce}, then the two droplets are assumed to bounce after colliding. However, if $2We_{coll}$ is larger than We_{bounce}, then either permanent coalescence, stretching or reflexive separation occurs. To determine if separation occurs following the collision event, the impact parameter, b, is evaluated

$$b = (r_1 + r_2)\sqrt{\mathcal{Y}} \tag{2.24}$$

where $\mathcal{Y}$ is a random number between zero and one and compared to the critical impact parameter, b_{crit}, given by

$$b_{crit} = (r_1 + r_2)\, min(1.0\,,\, \frac{2.4\, f_{coll}}{We_{coll}}) \tag{2.25}$$

where f_{coll} is a dimensionless function defined as

$$f_{coll} = \left(\frac{r_1}{r_2}\right)^3 - 2.4\left(\frac{r_1}{r_2}\right)^2 + 2.7\left(\frac{r_1}{r_2}\right). \tag{2.26}$$

If b is greater than b_{crit}, then separation may take place. If separation does not occur and $2We_{coll}$ is greater than We_{bounce}, then permanent coalescence is assumed to occur. Of all of the outcomes of droplet collisions, coalescence is the only one that results in the formation of larger droplets.

2.1.3 Validation of Spray Modeling Framework

Using the previously described modeling framework, the ability of the spray model to accurately represent the diesel fuel injection and spray formation process is assessed. As previously noted in Section 2.1.2, spray predictions have been known to suffer from both statistical noise and grid dependencies that stem from the DDM modeling approach and the treatment of the liquid-gas coupling and interactions. These potential shortcomings of the Lagrangian-Eulerian approach are addressed with statistical and grid convergence studies. Using a consistent computational mesh, statistical convergence of the spray model predictions is determined by evaluating the change in key predicted spray features as additional computational parcels are injected into the domain. Grid convergence is evaluated through the relative change in predicted spray parameters as the grid is refined. In order to ensure that the momentum exchange between the liquid and gas phases is adequately captured in the non-vaporizing spray simulations, the predicted mass and droplet size distribution are identified as key spray features. The mass distribution is quantified using the transverse integrated mass, TIM. At each axial location, TIM is defined as the path-integrated projected density and has units of μg/mm. TIM quantifies the amount of liquid mass contained within each axial slice of the spray. The droplet size distribution is characterized by evaluating the centerline SMD profile. The statistical and grid convergence studies are conducted under the baseline ECN non-vaporizing Spray A condition (see *Case 1* experimental condition detailed in Table 2.3).

2.1.3.1 Statistical Convergence Study

In order to ensure a sufficient number of computational parcels are injected into the simulation to statistically represent the spray, a statistical convergence study is performed. Using a consistent computational mesh, the statistical convergence of the spray features of interest are evaluated using four different levels of total injected

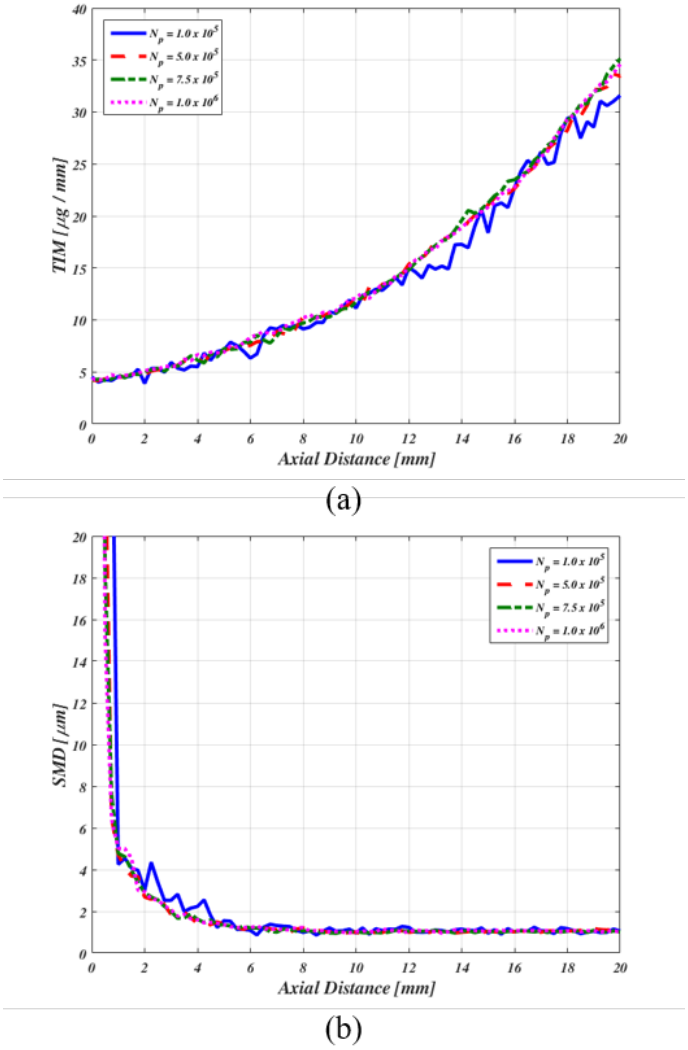

Figure 2.2: *Comparison of predicted axial distributions of (a) transverse integrated mass (TIM) and (c) Sauter mean diameter (SMD) for four different total number of injected computational parcels.*

parcels: 10^5, $5{\cdot}10^5$, $7.5{\cdot}10^5$, and 10^6. By evaluating the time-averaged axial TIM and SMD distributions, the statistical convergence of the temporal and spatial characteristics of the spray can be evaluated. The results of the study are shown in Figure 2.2 for the predicted axial (a) TIM and (b) SMD distributions. These results indicate that the spray is sufficiently represented using the DDM modeling approach when at least 500k computational parcels are injected into the simulation.

Table 2.1: *Minimum cell size and number of injected parcels utilized in the grid convergence study for the baseline non-evaporating Engine Combustion Network Spray A condition.*

Model Set-Up	**Minimum Grid Size** (dx_{min}) [μm]	**Number of Injected Parcels** (N_p)
1	500	11,720
2	250	93,750
3	125	750,000
4	62.5	3,000,000

2.1.3.2 Grid Convergence Study

In order to reduce the discretization error in the spray model predictions, a grid refinement study is performed to determine the minimum cell size where convergence is achieved for predicted spray parameters of interest. It is important to note that as the grid is refined, the number of injected computational parcels must be sufficiently increased [102–104]. As derived by Schmidt and Bedford for transient spray simulations [103], grid convergence is not achievable if the number of injected parcels is held constant as the mesh is refined. However, Schmidt and Bedford note that a rate of convergence on the order of one-half can be achieved for a transient three-dimensional spray simulation if the refinement of the grid by a factor of 2 is conducted with a simultaneous increase in the number of injected computational parcels by a factor of 8 (2^3).

Bearing these recommendations in mind, a grid convergence study is conducted using the cell size and corresponding number of injected parcels listed in Table 2.1. The results of the study are shown in Figure 2.3 for the predicted axial (a) TIM and (b) SMD distributions. These results indicate that grid convergence is achieved for the spray parameters of interest when a minimum cell size of 125 μm is employed.

The results of the statistical and grid convergence studies suggest that a spray simulation injecting 750k computational parcels into a domain with a minimum grid size of 125 μm in the near-nozzle region yield grid and statistically convergent spray predictions. Therefore, the spray simulation results presented in this thesis in Chap-

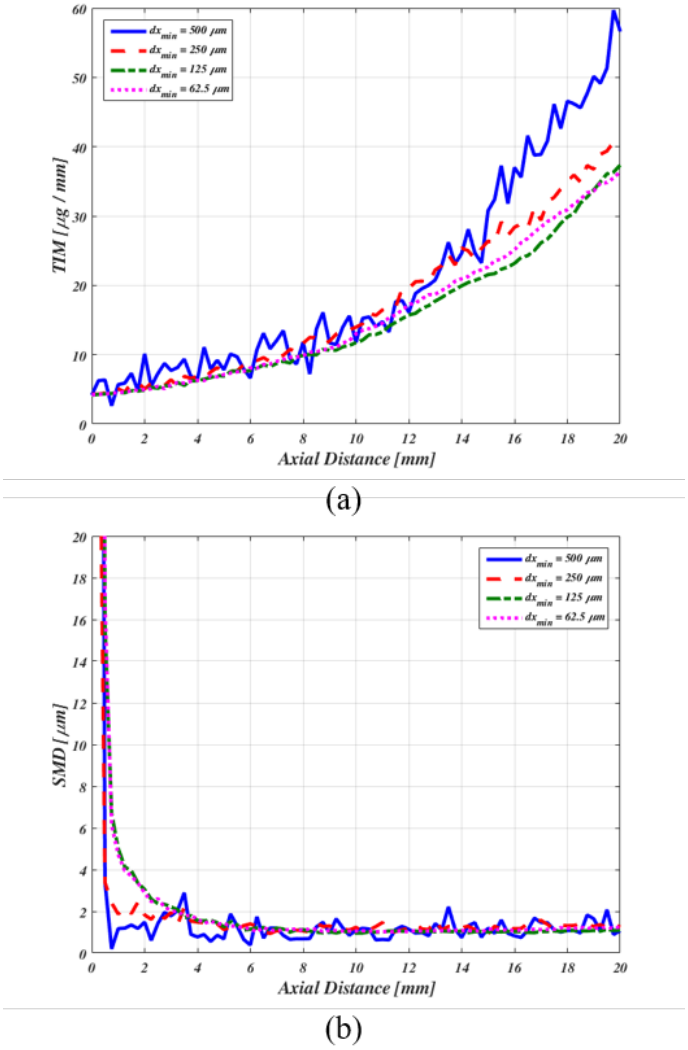

Figure 2.3: *Comparison of predicted axial distributions of (a) transverse integrated mass (TIM) and (b) Sauter mean diameter (SMD) for the four spray model set-ups detailed in Table 2.1.*

ters 4 and 5 employ these specifications to achieve statistically and spatially convergent spray predictions.

2.2 Spray Diagnostics

In order to assess spray predictions from existing primary atomization models, and determine how the influence of nozzle-generated turbulence should be represented in a spray model, experimental measurements are needed to characterize the spray struc-

ture under engine-relevant conditions. Evaluation of experimental spray observables over a wide conditions can provide insight into the governing physical mechanisms of fuel atomization under different engine operating conditions. This section details different spray diagnostics that are employed and utilized in this dissertation to guide model assessment and inform recommendations for an improved spray breakup model. The injection and ambient conditions evaluated in the computational and experimental investigations presented in this thesis are now presented.

2.2.1 Experimental Test Matrix

In order to better understand the interaction between aerodynamics and turbulence on the primary atomization process in diesel sprays, the dynamic and geometric factors contributing to cavitation inception must be systematically suppressed. As the fuel flows through the injector, the liquid fuel pressure continuously decreases from initially high values in the pressurized fuel supply to the ambient back pressure. Through informed selection of a fuel, such as n-dodecane [110], the likelihood of cavitation occuring due to the local reduction in pressure below the fuel vapor pressure can be minimized [81,82]. Cavitation can also be suppressed through careful selection of injectors with converging nozzles having a rounded inlet corner and minimal surface imperfections [81, 82, 111, 112]. Single-hole research-grade diesel injectors, with well-characterized internal nozzle geometries, are available through the Engine Combustion Network (ECN) [113]. Two classes of injectors provided by ECN that have ideal internal nozzle geometries for suppressing cavitation are the Spray A and Spray D injectors [94, 112]; key geometric features of the injectors are detailed in Table 2.2. As a result, for the experimental and computational investigations presented in this thesis, n-dodecane injected from the ECN Spray A and Spray D injectors will be studied so that the influence of cavitation on the resultant spray will be minimized.

Once the influence of cavitation on the spray has been minimized, changes in

Table 2.2: *Comparison of Engine Combustion Network Spray A and D injector nozzle geometries [113]. The total injected mass, injection duration and nozzle discharge coefficient are given for an injection pressure of 50 MPa and an ambient density of 22.8 kg/m^3 [88, 114].*

Injector Parameters	**Spray A #210675**	**Spray D #209133**
Nozzle diameter (d_j) [μm]	89.4	186
Nozzle Discharge Coefficient (C_d)	0.86	0.90
Injection Duration [ms]	6.00	4.69
Total Injected mass [mg]	15.2	51.6
Nozzle K-factor	1.5	3.7

injection and ambient conditions can be related to the changing turbulent and aerodynamic breakup phenomena. As previously discussed in Section 1.2.1.2, a set of experimental conditions can be defined to explore the aerodynamic and turbulent primary breakup regimes proposed by Wu and Faeth [18]. As shown in Figure 1.14, evaluation of ambient densities, ρ_g, between $1.2 - 22.8$ kg/m^3 allows for the proposed non-aerodynamic and merged aerodynamic secondary and primary breakup regimes to be investigated. Modulation of the fuel injection pressure, P_{inj}, from $50 - 150$ MPa and selection of injectors with different nozzle diameters, d_j, as defined in Table 2.2, allows for the influence of Reynolds on the resultant spray to be assessed. Using these selected ranges for ρ_g, P_{inj}, and d_j, 16 different cases were defined, as detailed in Table 2.3, the role of aerodynamics and turbulence on the breakup process in diesel sprays can be evaluated using both experimental and computational approaches.

2.2.2 X-Ray Measurements

When x-rays interact with steel in fuel injectors or liquid fuel droplets in a spray, the incident light is strongly absorbed and enables the characterization of the medium in the path of the beam. This is in direct contrast to optical diagnostics where visible light is scattered and reduces the detection of transmitted light, thereby limiting the

Table 2.3: *Non-vaporizing ambient and injection conditions for the Engine Combustion Network [113] Spray A and Spray D nozzles evaluated in this thesis. In all cases, n-dodecane at a fuel temperature of 303 K was injected in a pure nitrogen environment at an ambient temperature of 303 K.*

Case	**ECN Injector**	**Ambient Density** (ρ_g) $[kg/m^3]$	**Density Ratio** (ρ_f/ρ_g)	**Injection Pressure** (P_{inj}) **[MPa]**
1	A	22.8	32.7	150
2	A	22.8	32.7	50
3	A	7.6	98	150
4	A	7.6	98	50
5	A	2.4	310.4	150
6	A	2.4	310.4	50
7	A	1.2	620.8	150
8	A	1.2	620.8	50
9	D	22.8	32.7	150
10	D	22.8	32.7	50
11	D	7.6	98	150
12	D	7.6	98	50
13	D	2.4	310.4	150
14	D	2.4	310.4	50
15	D	1.2	620.8	150
16	D	1.2	620.8	50

applicability of optical techniques. As a result, x-ray diagnostics provide a unique capability in yielding quantitative information about the injector geometry and liquid mass and surface area distributions, particularly in highly scattering, optically thick regions of the spray. X-ray measurements, conducted by researchers at Argonne National Laboratory at the Advanced Photon Source (APS), enable improved definition for spray model inputs through high precision quantification of the fuel injector geometry, and yield validation data to assess spray breakup model predictions, particularly in regions of the spray inaccessible to optical techniques. In the subsequent sections, the x-ray experimental techniques and corresponding spray observables are detailed.

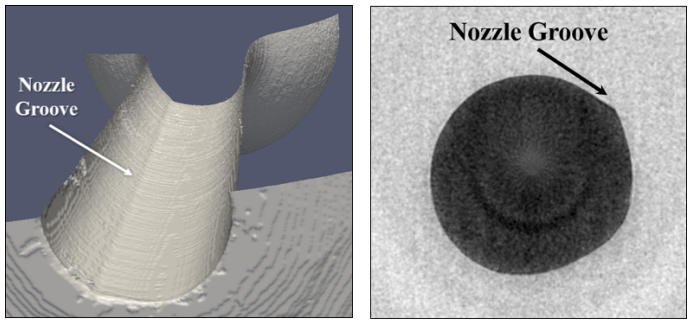

Figure 2.4: *Detailed internal nozzle geometry measurements from x-ray tomography conducted at the APS [94]. Renderings for the constructed (a) iso-surface of Spray D* #209133 *and (b) nozzle hole are shown.*

2.2.2.1 X-ray Tomography

Injector nozzle tomography measurements were conducted by Argonne researchers at the 7-BM beamline at the APS [115]. These measurements utilized x-ray images of the injector nozzle from 1800 lines of sight and computed tomography algorithms to reconstruct the geometry of the internal flow passages. A detailed description of the procedure can be found in [94]. The final reconstructed geometry, as shown for the ECN Spray D injector in Figure 2.4 has a spatial resolution of 1.8 μm, allowing nozzle features to be determined with great precision. Key features from the computed tomography can then be compared to the nominal manufacturer's specifications to assess machining tolerances for the injectors.

2.2.2.2 X-ray Radiography Technique

X-ray radiography (XRR) measurements were performed by Argonne researchers at the 7-BM beamline at the APS. XRR measurements are an absorption-based technique used to quantify the path-integrated liquid fuel mass distribution in a spray, commonly referred to as projected density, $\overline{M}$. A set of sample transverse distributions of $\overline{M}$ are shown in Figure 2.5 as scattered markers, and Gaussian fits to the data are overlaid and depicted using the solid lines. To obtain two-dimensional maps of

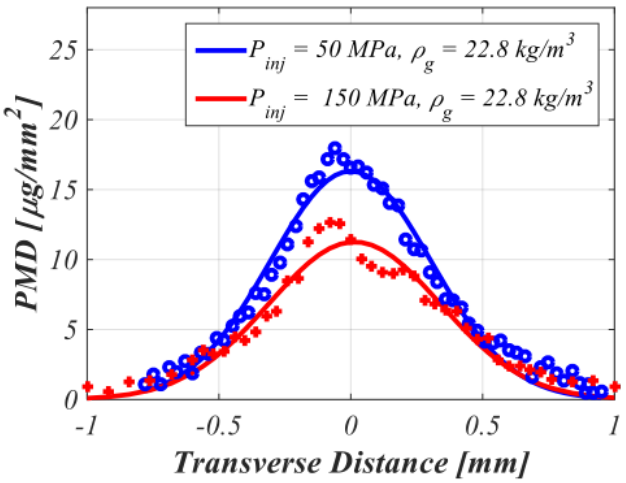

Figure 2.5: *Comparison of radial distribution of x-ray radiography measurements, at an axial distance of 8 mm from the nozzle exit [64].*

$\overline{M}$, the injector was horizontally mounted in a pressure chamber fitted with a pair of 12 x 30 mm x-ray transparent windows. The chamber was pressurized to the desired back pressure with N_2, which was also used to maintain a continuous purge flow of approximately 4 standard L/min through the chamber to minimize droplet formation on the windows during data acquisition. A diesel common-rail injection system was used to pressurize n-dodecane fuel to the desired rail pressure. The injector was fired at 3 Hz for a commanded injection duration of 2.0 ms.

Detailed descriptions of the time-resolved radiography measurements may be found in previous work conducted by Kastengren and co-workers [115–118], but are discussed here for completeness. A monochromatic beam at 8 keV energy passed through a set of curved mirrors, which focused the beam to a 5 x 6 μm point. The incoming beam intensity, I_0, was measured using a diamond x-ray beam monitor placed upstream of the pressure chamber. The outgoing beam intensity, I, downstream of the pressure chamber was measured with a PIN diode. As the x-ray beam passed through the fuel spray, photons were absorbed through the process of photoelectric absorption, attenuating the beam by an amount related to the quantity of fuel in the beam path of length z. When the XRR measurement is normalized by ρ_f, the quantity is shown

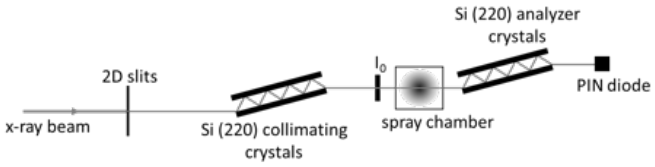

Figure 2.6: *A schematic of the Ultra-Small Angle X-ray Scattering experiment [94].*

to be proportional to the liquid volume fraction, LVF:

$$\overline{M} = \rho_f \frac{V_{liq}}{V} z = \rho_f (LVF) z. \tag{2.27}$$

2.2.2.3 Ultra-small Angle X-Ray Scattering Technique

Researchers at Argonne performed USAXS measurements at the 9-ID beamline of the APS in order to characterize the total surface area per sample volume of the spray. By combining the surface area measured with USAXS and volume of the droplets measured with radiography, the SMD of the droplet size distribution can be determined, where the SMD is defined as

$$SMD = 6\frac{V}{A} \tag{2.28}$$

where V and A are the volume and surface area of the droplets within the measurment volume, respectively.

A schematic of the experiment set-up is shown in Figure 2.6. A beam of x-rays at 21 keV was first shaped into a 50 x 500 μm H x V spot by a set of high precision 2D slits. The beam was then collimated using a pair of Si (220) crystals before interacting with the spray. As the beam passed through the spray, x-rays were scattered at small angles. The scattered x-rays were filtered downstream with a pair of Si (220) analyzer crystals, and the resulting intensity measured with a detector. The 9-ID beamline is equipped with a Bonse-Hart instrument to measure the scattering intensity, $I_{scat}(q)$, as a function of scattering vector, q [119]. The pair of analyzer crystals were rotated

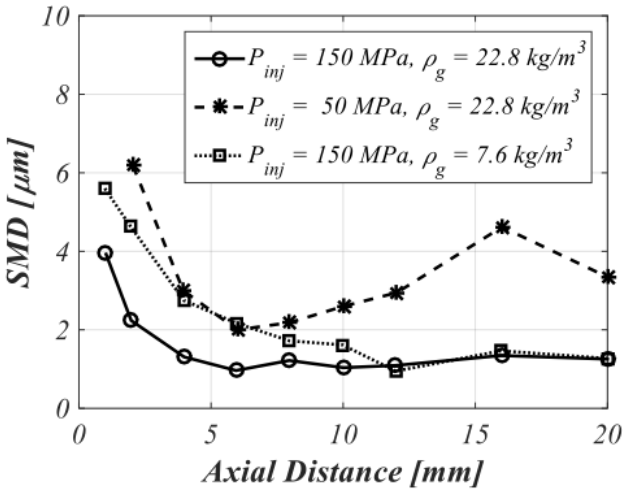

Figure 2.7: *Comparison of axial distributions of USAXS SMD measurements along the spray centerline [64]. Data is shown for a range of ambient density and injection pressure conditions for the ECN Spray A injector.*

to vary q between 1 x 10^{-4}Å^{-1} < q <1 x 10^{-2}Å^{-1} with a step size of 1 x 10^{-5}Å^{-1} at low q, with increasing step size for larger q. The scattered beam intensity as a function of q was measured at axial distances ranging from 1 to 20 mm downstream of the injection nozzle tip, at the centerline of the spray. Data were recorded in a 1 ms interval during the steady-state portion of the spray event. Background measurements were also recorded over 80 ms before each scan to account for any changes within the measurement domain caused by previous spray events. Once $I_{scat}(q)$ is measured, post-processing is performed using the Irena data analysis package [120] in order to obtain the surface area per volume of fuel droplets.

In order to find the spray centerline during USAXS measurements, a transverse scan at fixed q was also recorded at each axial location of interest. The spray centerline was taken to be the transverse location at which the beam intensity was a maximum, i.e. the location with the highest droplet density. Radiography measurements were temporally averaged during the steady portion of the spray event for the SMD calculation. The transverse profiles from the USAXS and radiography measurements were each centered about their full width at half maximum in order to

index the profiles onto the same coordinate system. Because the transverse location of the USAXS measurement is known at each axial distance, the corresponding radiography data at that location may be found. The USAXS measurement point is assumed to be in the center of the 50 x 500 μm measurement volume. All measured radiography points that fall within this window are averaged to arrive at one value of the pathlength, with interpolation and appropriate weighted averaging performed to accurately incorporate the edges of the measurement volume. The pathlength of fuel obtained from the radiography measurements provides the line-of-sight integrated volume of droplets in a sample of unit thickness. The USAXS measurements provide the line-of-sight surface area per volume of droplets, likewise in a sample of unit thickness. Thus, the two measurements can be combined per Equation 2.28 to arrive at a line-of-sight integrated SMD value at each measured axial location. A sample set of USAXS measurements conducted along the spray centerline for the ECN Spray A is shown in Figure 2.7.

2.2.3 High-Pressure Spray Facility

To complement the experimental work conducted by Argonne researchers at APS using x-rays, laser extinction measurements, diffused-back illumination (DBI) imaging and hydraulic characterization measurements were performed in a continuous flow optically-accessible high-pressure and temperature spray chamber at the Spray Physics and Engine Research Lab at Georgia Institute of Technology, as shown in Figure 2.8. The details of the spray facility have been previously detailed in previous works by Knox and Genzale [121,122], but are reproduced here for completeness. The spray chamber is capable of creating a quasi-quiescent environment with air, 99.5% N_2, or any mixture of the two at a maximum temperature and pressure of 950 K and 10 MPa. In order to control for the influence of vaporization on the resultant spray structure, all of the experiments for this study were conducted with air at room

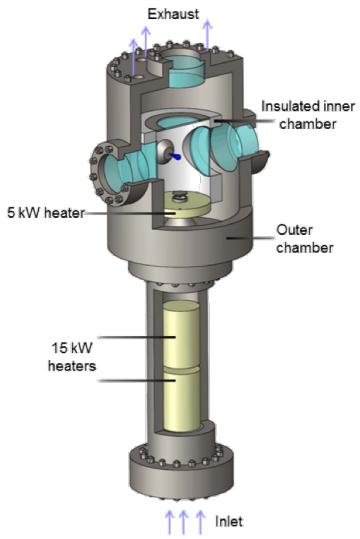

Figure 2.8: *An illustration of the continuous flow optically-accessible spray chamber [121].*

temperature. High-pressure air is supplied to the inlet to achieve the desired ambient density conditions listed in Table 2.3. The injector is mounted perpendicularly to the quartz windows, which provide approximately 100 mm of optical access at the front, sides, and the top of the chamber. The spray chamber was designed by Advanced Combustion Gmbh and is similar to other continuous flow-through spray chambers in the literature [123].

To investigate a range of fuel injection pressures listed in Table 2.3, a pneumatically-operated pump from MaxPro Technologies was used to provide fuel pressures up to 410 MPa. In order to monitor the fuel pressure and identify the start of injection, a time-resolved fuel pressure measurement near the inlet to the injector was acquired using a Kistler piezoresistive pressure sensor. The data was sampled using a National Instruments 9215 16-bit input module at 100 kHz.

2.2.4 Visible Extinction Measurements

While x-ray measurements can provide valuable information of the liquid mass distribution in a spray, full validation of predicted local spray characteristics requires a complementary measurement technique. An attractive option is the visible laser ex-

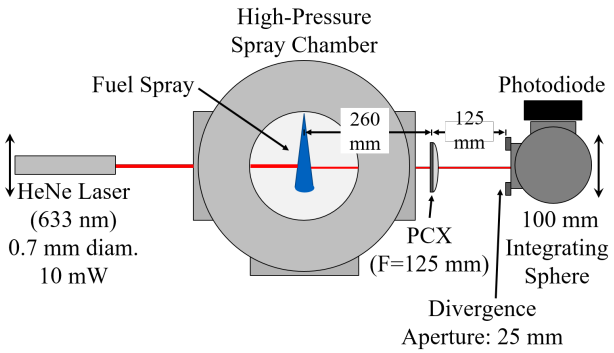

Figure 2.9: *A schematic of the high pressure spray chamber and laser extinction measurement set-up.*

tinction measurement technique [86,124–126]. Measurements of light attenuation can be used to quantify the path-integrated distribution of droplet size and number density in optically thin regions [127]. The laser extinction measurements were conducted in the high-pressure spray facility, detailed in Section 2.2.3, using the experimental set-up detailed in the next section. The use of this measurement to develop a new droplet sizing technique will be detailed in Chapter 3.

2.2.4.1 Laser Extinction Technique

The laser extinction experimental measurement set-up is depicted in Figure 2.9. A similar set-up has been utilized by researchers at Sandia National Laboratories to quantify soot optical thickness [128] and extinction from liquid-phase droplets under vaporizing conditions [126]. A 10 mW 0.7 mm diameter HeNe laser, centered at 633 nm, passes through the spray and is focused with a plano-convex lens (f = 125 mm) into the Newport 819C-SF-4 spectraflect-coated integrating sphere. This signal detection arrangement provides a 5.6° viewing angle of the forward-scattered laser illumination. The plano-convex lens was sized to 50.8 mm to ensure that the transmitted laser beam is fully captured at the 25 mm diameter integrating sphere aperture in the event of beam steering, while the integrating sphere creates an equal distribution of light across the active area of the photodiode to reduce bias error of the

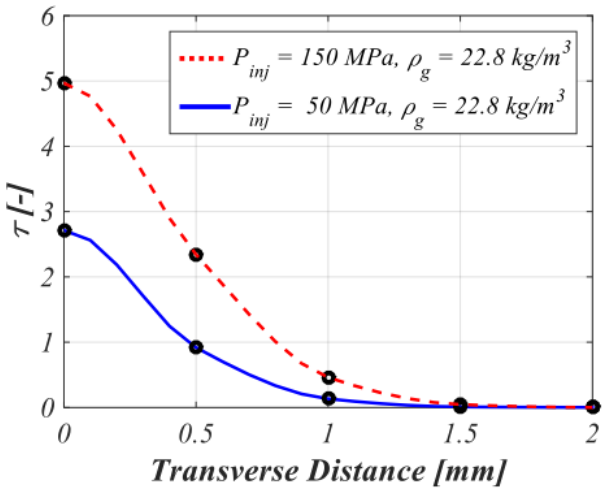

Figure 2.10: *Comparison of radial distribution of laser extinction measurements, τ, at two different injection pressures (50 and 150 MPa) [86]. The distributions are shown for a location 8 mm from the injector nozzle exit. Each experimental data point shows the mean optical thickness, ensemble-averaged over 30 injections.*

measurement [128]. The incident light intensity before the injection event, I_0, and the transmitted light intensity during the injection event, I, were recorded as a function of time using a Thorlabs PDA36A silicon transimpedance amplified photodetector. The signal was sampled using an National Instruments 9215 16-bit input module at 100 kHz.

The HeNe laser and light collection optics were each mounted on separate stepper motor-controlled traverses, which were synchronized to maintain alignment and allow for measurements at many axial and radial locations throughout the spray. The laser was rastered across the spray with a spatial resolution of 0.5 mm and allowed for the collection of I_0 and I to be related to the optical depth, τ, using the Beer-Lambert law:

$$\frac{I}{I_0} = e^{-\tau}. \tag{2.29}$$

Sample measurements of τ are shown in Figure 2.10.

Because measurements in this work were taken at room-temperature conditions,

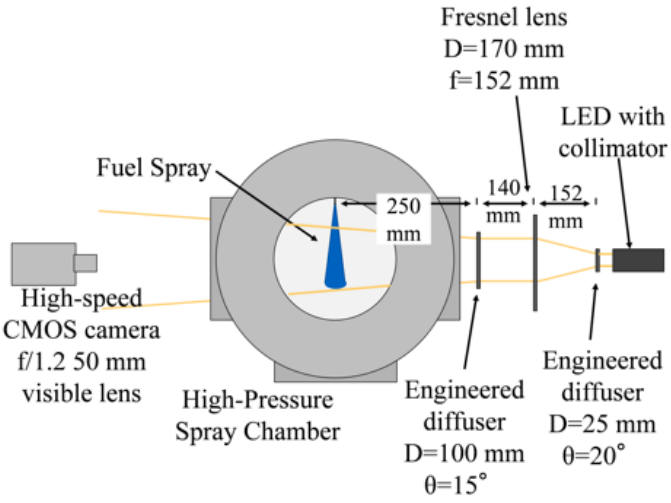

Figure 2.11: *Experimental arrangement for diffused back-illuminated imaging, based on the recommendations outlined by Westlye and co-workers [129].*

where the chamber was at thermal equilibrium with the environment, beam steering effects are not expected. However, this set-up was employed to provide the flexibility of pursuing high-temperature vaporizing conditions in the future. This experimental configuration has been shown to yield consistent quantification of light transmission over a range of ambient temperatures, pressures, and levels of beam steering [126,128].

2.2.4.2 Diffused-Back Illumination Imaging

Two-dimensional line-of-sight extinction maps of the spray were obtained by a colleague using a diffused back-illumination arrangement, following the recommendations of Westlye and co-workers [129], as shown in Figure 2.11. The resulting image resolution for the optical arrangement was approximately 78 μm/pixel. To freeze the motion of the spray, a Light-Speed Technologies white LED was used with a pulse width of 90 ns. A Photron SA-X2 camera, fitted with a 50-mm f/1.2 les, captured the spray at 72 kfps while the LED pulsed every other frame. The camera captured a dark frame every other frame, which allowed the sensor to reset prior to the next frame. Westlye and co-workers recommended this procedure as a way to reduce error in the measured extinction due to ghosting, which is residual charge left on the

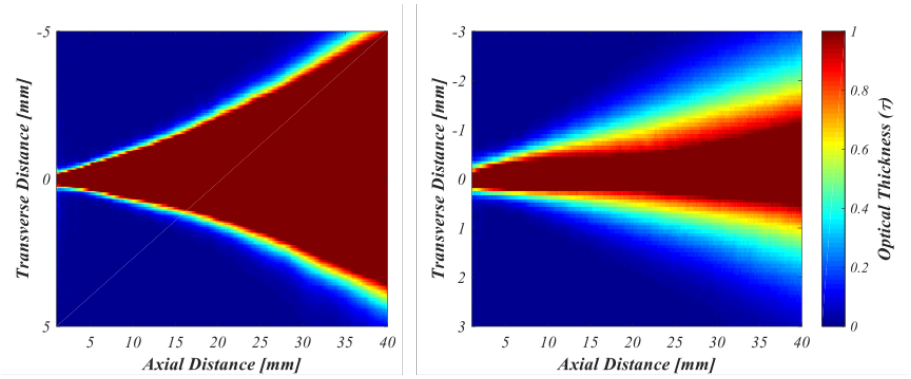

Figure 2.12: *Example 2D extinction maps obtained from DBI measurements are shown for P_{inj} of 50 MPa and P_{amb} of (a) 2 MPa and (b) 0.1 MPa.*

sensor for the next frame [129]. Figure 2.12(a)-(b) shows examples of time-averaged two-dimensional extinction maps produced for the Case 10 and 16 conditions, respectively, as defined in Table 2.3 for the ECN Spray D injector, with the injector nozzle centered at 0-mm in the axial and transverse coordinates.

2.2.5 Rate of Injection and Injector Nozzle Flow Characterization

The rate-of-injection (ROI) profile for each injector was obtained from rate-of-momentum measurements conducted by colleagues in the Georgia Institute of Technology's spray vessel (Section 2.2.3) using the impingement technique, as schematically shown in Figure 2.13. A summary of the experimental measurement technique is provided here, but further details and uncertainty quantification can be found in previous work performed by Knox and co-workers [122, 130]. Using the impingement technique, the transducer measures the reaction force of the control volume surrounding a single spray plume. Using control volume analysis, the reaction force can be related to the rate of momentum of the spray at the nozzle exit. Under atmospheric back pressure conditions, the measured reaction force is typically equated to the rate of momentum of the spray due to the neglibigle influence of the ambient air on the spray momentum transport. However, under elevated back pressure conditions, Knox and co-workers

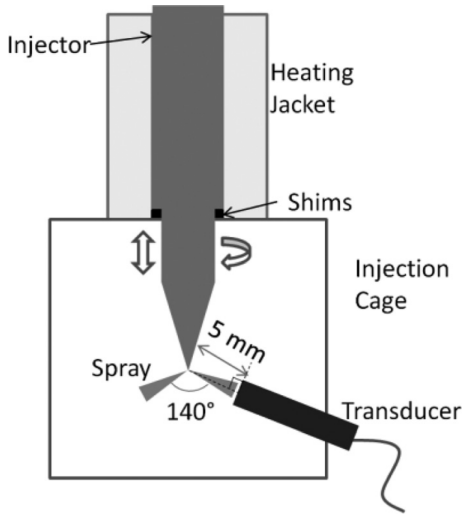

Figure 2.13: *Schematic of apparatus for rate-of-momentum measurement [122]. The schematic is shown for a multi-hole injector.*

have demonstrated that careful consideration of the ambient gas is required to reduce uncertainties in the rate of momentum measurements [122, 130].

The rate-of-momentum measurements, along with measurements of total collected mass over 50 injections, can then be used to determine the rate-of-injection (ROI) profiles. The ROI profile is an important parameter for spray simulations because it is used to define the define the injection velocity boundary condition at the nozzle exit. ROI profiles for the ECN Spray A (#211020) and Spray D (#209133) nozzles, are shown in Figure 2.14 for an ambient pressure (P_{amb}) condition of 2 MPa and injection pressure of 50 MPa.

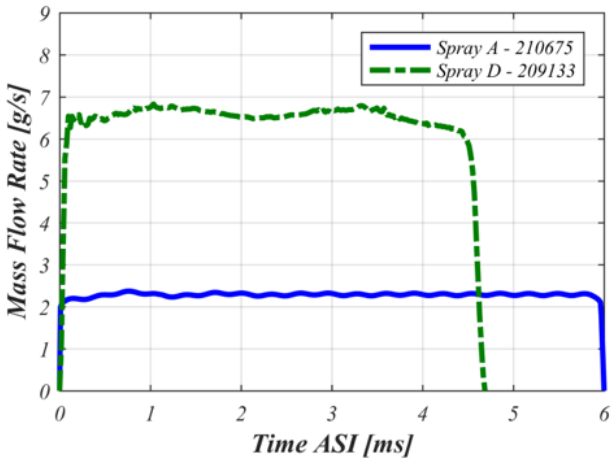

Figure 2.14: *Comparison of the modeled ECN Spray A ROI [114, 131] and measured Spray D ROI [88] profiles at* $\rho_g = 22.8\ kg/m^3$ *and* $P_{inj} = 50\ MPa$.

CHAPTER 3
SCATTERING AND ABSORPTION MEASUREMENT RATIO TECHNIQUE

As previously discussed, a database of droplet sizing measurements, capable of guiding a critical assessment of existing spray model predictions, is currently missing. To complement available data from the resource intensive USAXS measurement technique, a new droplet sizing method was developed. In particular, path-integrated XRR and laser extinction measurements were employed because both measurements are joint functions of spray parameters, namely droplet size and liquid volume fraction. By conducting a ratio of the two measurements, it is possible to deconvolve the scattering absorption measurement ratio (SAMR) and relate it to an average droplet size within the probed volume. In this chapter, the theoretical basis of the SAMR technique is demonstrated. The steps for jointly processing the laser extinction and XRR measurements to determine the measurement ratio are also detailed. The available axial and transverse SMD distributions from the USAXS technique, conducted by researchers at Argonne National Laboratory [64], are then presented, discussed, and used for cross-validation and assessment of the SAMR measurements. This work has been detailed in published works by the author, and are shown here for posterity [85, 86, 132].

3.1 Theoretical Development of Scattering Absorption Measurement Ratio Technique

The measured attentuation of light as it passes through the droplet field, quantified using the optical thickness, τ, can be related to other measurable spray quantities,

such as d and LVF via the Mie solution to Maxwell's equation. The Mie solution describes the 3-D scattering and absorption behavior for a plane wave of light interacting with a spherical object [127]. Following Mie-theory:

$$\tau = \alpha_{ext}\, z \tag{3.1}$$

where α_{ext} is the attenuation coefficient and, z, is the illumination path-length through the droplet field. For a distribution of droplet sizes within the probed cloud, α_{ext} can be expressed as:

$$\alpha_{ext} = \sum_j C_{ext,j}\,(N/V)_j = \frac{1}{V}\sum_j C_{ext,j}\,N_j \tag{3.2}$$

where $(N/V)_j$ is the number of droplets of size j within the probed volume, V, and $C_{ext,j}$ is the corresponding extinction cross section for drops of size j. The expression for τ can be simplified when there is a distribution of droplet sizes by introducing the number-weighted mean extinction cross section, $\overline{C_{ext}}$:

$$\overline{C_{ext}} = \sum_j \frac{C_{ext,j}\,N_j}{N} = \frac{1}{N}\sum_j C_{ext,j}\,N_j \tag{3.3}$$

Thus, α_{ext} can be expressed as the product of $\overline{C_{ext}}$ and (N/V) in the probed volume:

$$\alpha_{ext} = \overline{C_{ext}}\,(N/V). \tag{3.4}$$

(N/V) can also be expressed as a function of the liquid volume fraction, LVF, within the probed volume, and α_{ext} can be reformulated in terms of LVF:

$$LVF = \frac{V_{liq}}{V} = \frac{\sum_j N_j\,(\pi\, d_j^3/6)}{V} \tag{3.5}$$

$$\alpha_{ext} = \overline{C_{ext}}\frac{LVF \cdot N}{\sum_j N_j\,(\pi\, d_j^3/6)} \tag{3.6}$$

The expression for α_{ext} can be further simplified by introducing the number-weighted mean droplet volume, $\overline{\pi\, d^3/6}$, and substituting the relation into Equation 3.6:

$$\overline{\pi\, d^3/6} = \sum_j \frac{(\pi\, d^3/6)\, N_j}{N} \tag{3.7}$$

$$\alpha_{ext} = \frac{\overline{C_{ext}}}{\overline{\pi\, d^3/6}} LVF \tag{3.8}$$

Thus, a simplified expression for the attenuation coefficient, valid for a distribution of droplet sizes in the probed droplet cloud is obtained. Substituting Equation 3.8 into Equation 3.1 shows τ as a function of LVF and d:

$$\tau = \frac{\overline{C_{ext}}}{\overline{\pi\, d^3/6}} \cdot LVF \cdot z \tag{3.9}$$

It should be noted that within the Mie scattering regime, it has been shown that C_{ext} is proportional to the geometric cross-sectional area of the droplet (d^2) [127].

Laser extinction measurements can be related to the underlying droplet sizes and number density within the probed volume at locations in the spray where the attenuation of light, as defined by the Beer-Lambert Law in Eqn. 2.29, is dominated by single and independent scattering events; under such conditions, theoretical Mie-scattering equations hold. Typically, the single scattering assumption is considered valid for $\tau < 1$. However, Monte-Carlo light scattering simulations of laser extinction from Berrocal and co-workers [133] have shown that the optical depth at which errors due to multiple scattering become significant depends jointly on the characteristic droplet sizes present in the probed region and the collection angle of the laser detection optics. Berrocal and co-workers showed that for a monodisperse collection of small droplets (1 μm) and narrow collection angles (1.5°), the measurement error due to multiple scattering was only 2% for τ less than 2. However, their simulations showed that errors increased to $25 - 317\%$ for larger droplets (5 μm) and collection

angles (8.5°). As previously noted in Section 2.2.4.1, the maximum half-collection angle in the employed laser extinction measurement set-up is 5.6°, and based on USAXS measurements, shown in Figure 2.7, the underlying SMD of the probed region can lie between $1-5$ μm. Thus, it is possible that the laser extinction measurements can be accurately related to droplet size and number density in probed regions where $\tau < 2$. In Section 3.2.1, regions of the spray where $\tau < 2$ are interpreted, keeping in mind that errors in these regions can grow substantially if droplets larger than 5 μm are present. Further work is required to quantify multiple scattering errors for polydisperse droplet distributions, such as those present in the sprays studied in this work. Although multiple scattering effects will limit regions where laser extinction measurements can be reliably related to the underlying droplet field characteristics, laser extinction measurements still offer an improvement over traditional droplet sizing measurements for high-pressure sprays because of their ability to quantify spray structure details in regions closer to the nozzle exit ($x/d_j \sim 90$) than has previously been achieved ($x/d_j > 200$) [60, 61, 134].

As previously discussed, path-integrated XRR and laser extinction measurements yield useful information about the structure of the spray because they are both joint functions of spray parameters, namely droplet size and number density. By conducting a ratio of the two measurements, it is possible to deconvolve the scattering absorption measurement ratio (SAMR) and relate it to an average droplet size within the probed volume. As shown in Equation 3.9, application of the Mie-scatter solution to Maxwell's equations yields an expression for the measured τ as a function of the LVF, $\overline{C_{ext}}$, and $\overline{\pi\, d^3/6}$ within the laser probed measurement volume. For non-vaporizing isothermal conditions with constant ρ_f throughout the spray, $\overline{M}$ can be recast as a measurement of LVF, as defined in Equation 2.27. Thus, for overlapping XRR and laser extinction measurement volumes, the measurement ratio is shown to

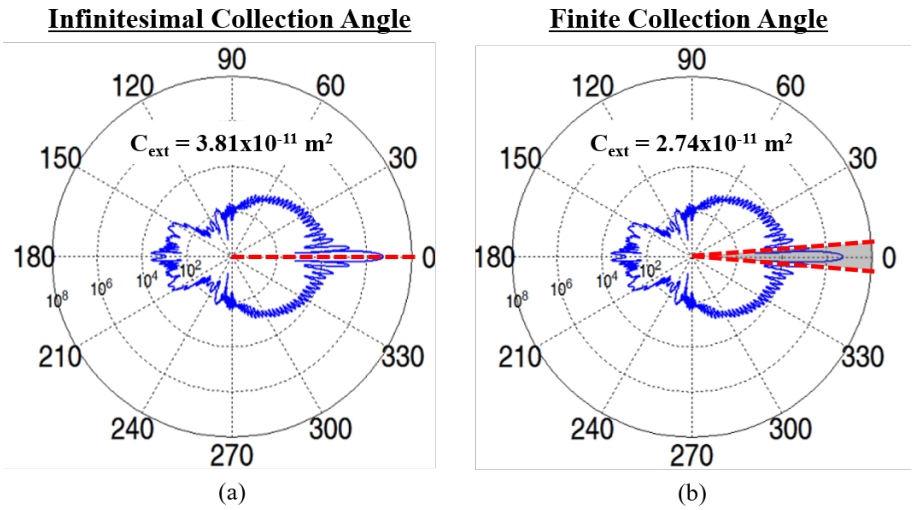

Figure 3.1: *Influence of collection angle on collection of forward scattered light and* C_{ext} *from a* $5\mu m$ *droplet.* $\theta_{1/2} \approx 0°$ *is shown in (a) while* $\theta_{1/2} = 5.6°$ *is shown in (b).*

be proportional to SMD:

$$\frac{\overline{M}/\rho_f}{\tau} = \frac{\overline{\pi\, d^3/6}}{\overline{C_{ext}}} \propto \frac{\overline{d^3}}{\overline{d^2}} \propto SMD \tag{3.10}$$

To relate the measurement ratio to the SMD of the droplet size distribution, C_{ext} must be determined. Using the publicly available program MiePlot [135], $\overline{C_{ext}}$ is determined for a given SMD using an assumed log-normal droplet size distribution, along with the incident laser wavelength (633 nm) and index of refraction for n-dodecane in air (1.422). As graphically depicted in Figure 3.1, the calculation of C_{ext} also depends on the collection angle of the laser detection optics ($\theta_{1/2}$). As $\theta_{1/2}$ is increased, additional forward scattered light is detected, which serves to decrease C_{ext}; for an increase in $\theta_{1/2}$ from approximately 0° to 5.6°, C_{ext} decreases by approximately 28%.

The measurement ratio is then related to SMD by normalizing the calculated $\overline{C_{ext}}$ by $\overline{\pi\, d^3/6}$ for the assumed drop size distribution. This relationship is depicted in Figure 3.2, where a range of expected SMD from 0.1 – 10 μm and geometric standard deviation, σ_g, from 1.0 - 1.75 of the assumed droplet size distribution is

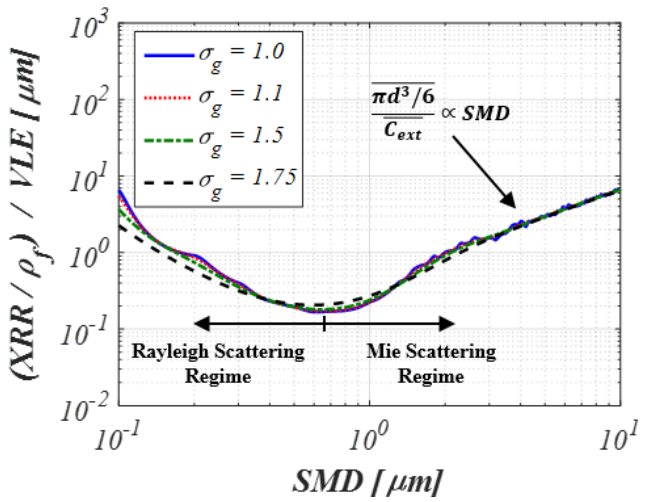

Figure 3.2: *SAMR measurement ratio as a function of SMD. Solutions for diesel-like sprays are evaluated within the Mie scattering regime.*

shown. This chart serves as a lookup table of SMD for a given measurement ratio. As shown in Figure 3.2, the droplet size distribution assumed in the determination of $\overline{C_{ext}}$ and $\overline{\pi\, d^3/6}$ has little effect on the relationship between the measurement ratio and SMD for droplets in the Mie-scattering regime. Thus, for simplicity, a monodisperse assumption ($\sigma_g = 1.0$) is employed in subsequent calculations.

As shown in Figure 3.2, two possible SMD solutions exist, one from the Mie-scattering regime and one from Rayleigh-scattering regime, for a given measurement ratio. In general, measurements in the literature indicate SMD values for diesel sprays that are greater than 1 μm [64, 65, 136], as indicated by the USAXS measurements in Figure 2.7. These findings indicate that the Mie solution should provide a consistent estimation with results from the literature, and this assumption is employed in this work to quantify SMD from the SAMR technique. However, such an assumption should be employed with caution for We_g and Re_f conditions outside of those characterizing diesel spray conditions. Note that in circumstances where the existence of larger SMD values within the Mie-scattering regime could be ruled out, the SAMR technique also enables drop sizing down to sub-micron levels.

3.2 Scattering and Absorption Measurement Ratio Analysis

The ability of the SAMR technique to quantify the SMD within the measurement volume has been theoretically demonstrated, as defined in Equation 3.10. In practice, there are several factors that must be considered when jointly processing the visible and x-ray measurements to extract a measurement ratio. This section details best practices for jointly processing the scattering and absorption measurements, conducted under the Case $1-3$ conditions defined in Table 2.3 using the ECN Spray A injector detailed in Table 2.2. The section ends with an estimation of uncertainty in SMD from the SAMR technique.

3.2.1 Joint Processing of Visible and X-Ray Extinction Measurements

Careful consideration is required when jointly processing data conducted in separate spray vessels using different experimental techniques. For asymmetric sprays with high variability in the spray structure in the azimuthal direction, it is important to ensure that consistent injector orientations are used for both measurements. The x-ray radiography data shown in Figure 2.5 under the Case 1 and Case 2 conditions exhibit relatively symmetric distributions, as indicated by their close agreement with the fitted Gaussian distribution. Although these measurements are the result of a projection from a single viewing angle of the spray, these results suggest that the spray is relatively symmetric under these conditions. Therefore, in this analysis, half of the transverse distribution is used to represent the measurement. Overall, the influence of relative injector orientation between the XRR and laser extinction measurements on the resultant measurement ratio is expected to be small. The influence of injector orientation on the uncertainty in SMD from the SAMR technique is explored in Section 3.2.2 by evaluating the measurement ratio with 0° and 180° orientations of the x-ray radiography measurements.

When conducting the measurement ratio, it is important to consistently define and align the central spray axis between the two measurements. When jointly processing the XRR and USAXS measurements under the Case 1 - 3 conditions, Kastengren and co-workers co-aligned the peaks of the two measurement distributions to center their measurements [64]; for these conditions, they noted that uncertainty in SMD due to relative positioning errors was small, on the order of $\pm 5\%$. It should be noted however that this definiton may not be appropriate under all conditions, particularly if the spray centerline is not co-located with the peak in the distribution. For example, under low back pressure conditions, Martinez and co-workers [132] noted that defining the spray centerline by centering the full-width at half max of the distribution more accurately characterized the measurement distributions. For the Case 1 and 2 conditions considered, the spray centerline was defined using the peak value of the XRR and laser extinction measurements, bearing in mind that this method may not be robustly applicable under all conditions. The uncertainty in SMD due to positioning errors from the SAMR technique is discussed in further detail in Section 3.2.2.

Once the two measurements are spatially aligned, the XRR and laser extinction data must be resampled. Each transverse distribution is fitted with a unique function in order to faithfully represent the measurement. As shown in Figure 3.3, the XRR data is fitted with a single term exponential function in regions where the measurement ratio can be interpreted. These regions were defined using an upper bound for the measured τ and a lower bound for the measured $\overline{M}$. As previously discussed, τ can be interpreted in terms of spray parameters, such as droplet size and LVF when independent and single scattering events dominate the measured signal; because interpretation is expected to be valid for $\tau < 2$, analysis of the measurement ratio is limited to regions where $\tau < 2$. The lower bound for $\overline{M}$ was determined using the measured noise floor, which is defined as twice the standard deviation of the measured signal along the periphery of the spray. The noise floor was determined

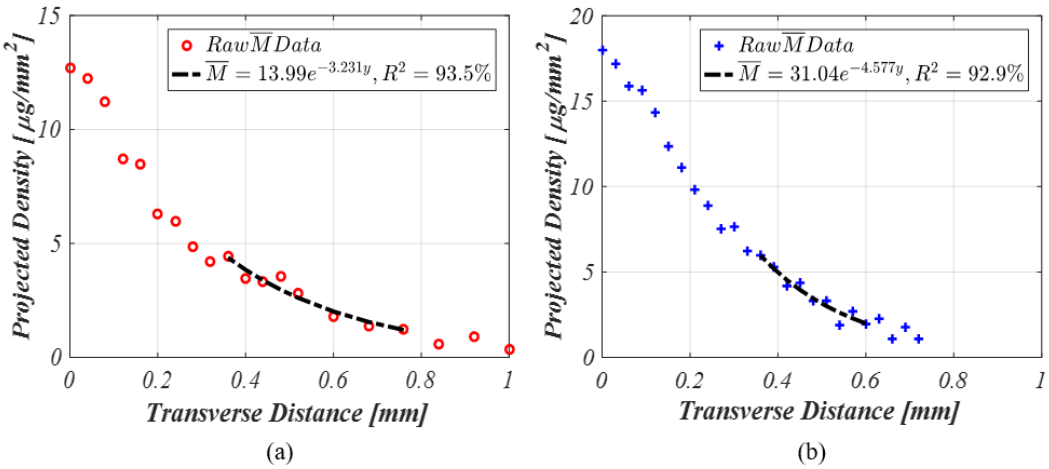

Figure 3.3: *A single term exponential function is used to represent the XRR measurements under an injection pressure of (a)150 MPa and (b) 50 MPa.*

to be 1.434 μg/mm^2 for the Case 1 condition and 1.214 μg/mm^2 for the Case 2 condition. The laser extinction data is fitted with a piecewise cubic Hermite interpolating polynomial (*pchip*) function, as previously shown in Figure 2.10.

Using the curve fits for the XRR and laser extinction data, equivalent measurement volumes are constructed for the joint measurement analysis. The size of the measurement volume dictates the region over which the experimental data is averaged, and therefore should be equivalent to the dimensions of the light source. This would ensure a representative and consistent volume over which the two line-of-sight measurements can be simultaneously analyzed. However, although the dimensions of the x-ray and laser extinction laser beam are well known at the light source, the exact dimensions of each of the beams at the spray axis are unknown due to interactions of the light with the windows and droplets. The exact dimensions characterizing the measurement volume are therefore uncertain.

In order to assess the influence of the assumed measurement volume size on the measurement ratio, a range of bin sizes, Δ, from $10 - 250$ μm were evaluated, as shown in Figure 3.4. For both Case 1 and Case 2 conditions, although the selected Δ controls the volume over which the averaging is considered, Δ is seen to have a

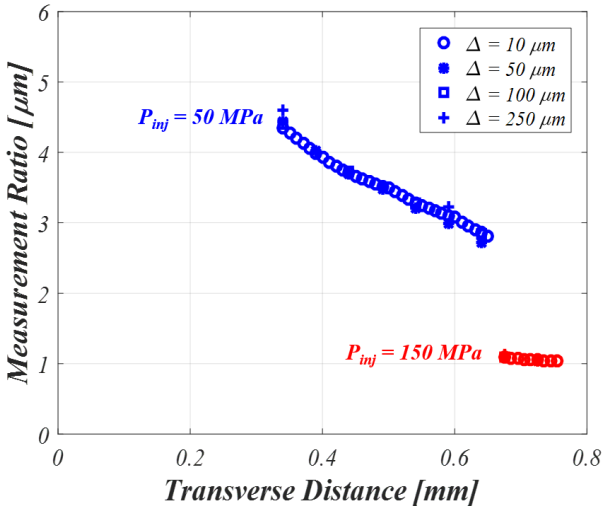

Figure 3.4: *Influence of measurement volume dimension, Δ, on calculated measurement ratio.*

minimal influence on the measurement ratio (less than $\pm 3\%$). However, employing finer resolution allows for more information to be obtained regarding the shape of the measurement ratio, and ultimately SMD, distribution. As a result, in this analysis a resolution of 10 μm is selected. Using the average value of $\overline{M}$ and τ within each bin, and ρ_f evaluated at the nozzle exit thermodynamic condition, the measurement ratio is calculated using Eqn. 3.10 to determine SMD via the look-up table shown in Figure 3.2.

3.2.2 Uncertainty Analysis of SMD from SAMR Technique

The major sources of the uncertainty in SMD from the SAMR technique are due to uncertainties in relative positions within the spray and injector orientations between the x-ray and visible extinction measurements, and errors introduced from multiple scattering events. In particular, uncertainty in the measurement location in the transverse direction of the laser extinction measurements by ± 0.05 mm could result in up to 12% uncertainty in the measured SMD. Uncertainty in relative injector orientations between the two measurements was assessed by evaluating the measurement

ratio with 0° and 180° orientations of the x-ray radiography measurements, which yields an uncertainty of approximately 17% in the measured SMD. A conservative estimate for the uncertainty in SMD due to multiple scattering events is between $10-60\%$. Adding in quadrature, the resulting uncertainty of the SMD measurement is between $23-64\%$. Further details on the estimation of the uncertainty due to multiple scattering on the SMD measurement can be found in the next section. Future work should focus on reducing uncertainty in both the relative measurement position and injector orientations, and better quantifying expected multiple scattering errors for the evaluated spray conditions and employed measurement system.

3.2.2.1 Estimation of Uncertainty in SMD Due to Multiple Scattering Events

For the scattering absorption measurement ratio (SAMR) technique, the estimated uncertainty in SMD due to multiple scattering events was determined through its influence on τ, and ultimately on the measurement ratio. The Beer-Lambert law, defined in Eqn. 2.29, describes the transmission of light along the optical axis of the incident light that is detected within an infinitesimal collection angle ($\theta_{1/2} \approx 0°$). With a finite collection angle, additional forward scattered light is collected due to single and multiple scattering events. In general, multiple scattering will serve to increase the forward-scattered illumination and reduce the measured optical thickness, $\tau_{Measured}$, which will artificially increase the measurement ratio and derived SMD. As detailed in the works of Berrocal and co-workers [133], the contribution of multiply scattered light to the detected forward-scattered light is a function of droplet size, optical depth and collection angle of the laser detection optics. To characterize the contribution of multiple scattered light on the reduction in $\tau_{Measured}$, Berrocal and co-workers determined a modification to the Beer-Lambert law based on Monte-Carlo light scattering simulations for two different droplet sizes (1 and 5 μm) and half-angles for the detection optics ($\theta_{1/2} = 1.5°$ and 8.5°) [133]. The modified Beer-Lambert law

allowed for $\tau_{Measured}$ to be related to a corrected optical thickness, $\tau_{Corrected}$, which quantifies the detected attenuation of light along the optical axis if an infinitesimally small collection angle were employed.

In order to obtain a conservative estimate for the contribution of multiple scattering events on $\tau_{Measured}$, and ultimately on SMD, the correction factor developed by Berrocal and co-workers [133] for a 5 μm mono-disperse droplet size distribution is employed,

$$\tau_{Measured} = \tau_{Corrected} - \alpha \cdot \tau_{Corrected}^{\beta} \tag{3.11}$$

where α and β are constants used to account for the average size of droplets detected within the half-angle of the collection optics. $\tau_{Corrected}$ is determined for a given $\tau_{Measured}$ using the MATLAB *vpasolve* numerical solver. Because $\theta_{1/2}$ for the laser extinction measurement set-up (5.6°) lies within the range of detection angles considered by Berrocal (1.5° and 8.5°), $\tau_{Corrected}$ is evaluated considering both $\theta_{1/2}$ configurations in order to bound the contribution of multiply scattered light on $\tau_{Measured}$. Based on the findings from Berrocal and co-workers [133], for $\theta_{1/2} = 1.5°$, α and β are equal to 0.05 and 1.78, respectively, whereas for $\theta_{1/2} = 8.5°$, α and β are equal to 0.54 and 1.05, respectively.

The potential contribution of multiply scattered light on $\tau_{Measured}$ is illustrated in Figure 3.5 for the (a) Case 1 and (b) Case 2 conditions. For a narrow collection angle of 1.5°, multiply scattered light has a minimal contribution on $\tau_{Measured}$, as evidenced by the close agreement between $\tau_{Measured}$ and $\tau_{Corrected}$ at all levels of optical depth across the width of the spray. However, as $\theta_{1/2}$ is increased to 8.5°, differences up to 160% between $\tau_{Measured}$ and $\tau_{Corrected}$ can be seen at transverse positions close to the spray centerline, indicating a large contribution of multiple scattering to the detected forward-scattered light at high levels of optical depth. To limit the errors introduced from multiple scattering, evaluation of the measurement ratio is therefore confined to

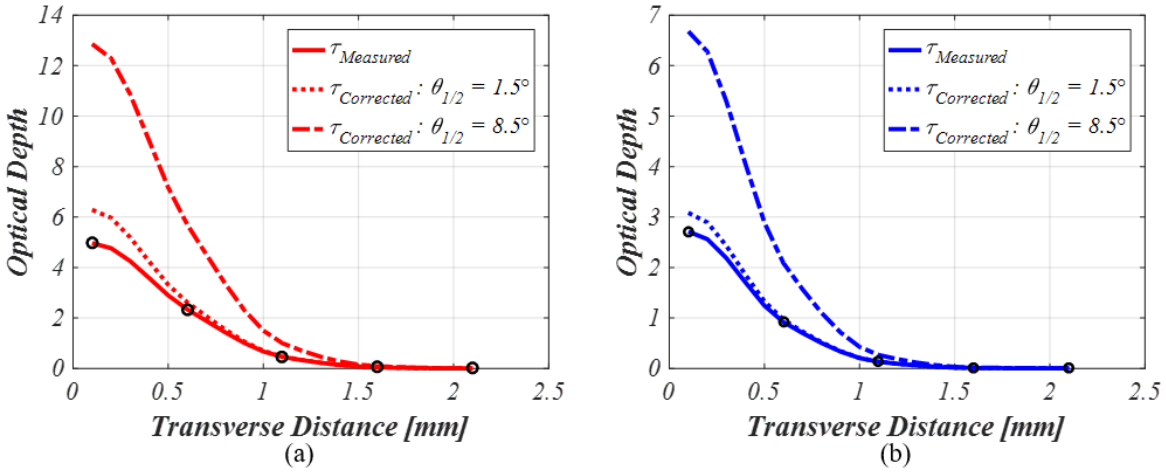

Figure 3.5: *Comparison of measured and corrected radial distribution of laser extinction measurements, τ, at two different injection pressures ((a) 150 MPa and (b) 50 MPa). The distributions are shown for a location 8 mm from the injector nozzle exit. The measurements locations are indicated with black markers on the distribution.*

transverse positions where $\tau_{Measured} < 2$.

Within the peripheral region of the spray where $\tau_{Measured} < 2$, the contribution of multiply scattered light on $\tau_{Measured}$, and ultimately the measurement ratio, is limited. However, even if the influence of multiple scattering on $\tau_{Measured}$ is minimal, and the measured and corrected measurement ratio are similar, different SMD values may be derived. This difference is due to the unique $\theta_{1/2}$ employed for the detection of forward scattered light for $\tau_{Measured}$ ($\theta_{1/2} = 5.6°$) and $\tau_{Corrected}$ ($\theta_{1/2} \approx 0°$). As previously shown in Figure 3.1, $\overline{C_{ext}}$ is a function of $\theta_{1/2}$; as $\theta_{1/2}$ is increased, additional forward-scattered light is detected, and serves to decrease the apparent $\overline{C_{ext}}$. From Eqn. 3.10, it is clear that decreasing $\overline{C_{ext}}$ results in smaller measurement ratio for a given SMD. As illustrated in Figure 3.6, increasing $\theta_{1/2}$ from approximately 0° to 5.6° results in a larger measurement ratio for a given SMD; this difference increases with increasing SMD, particularly for SMD greater than 2 μm. For a fixed measurement ratio, smaller SMD values would be indicated when relatively larger $\theta_{1/2}$ are employed. Therefore, considering the influence of $\tau_{Corrected}$ on the measurement ratio and resultant SMD, a conservative estimate for the uncertainty in SMD due

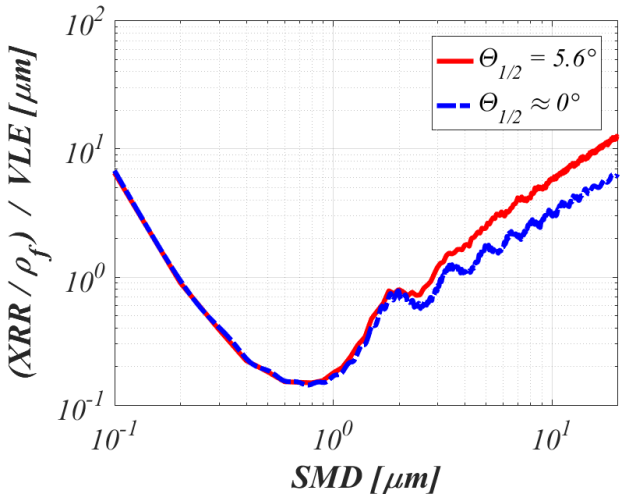

Figure 3.6: *SAMR measurement ratio as a function of SMD and half-collection angle of the laser detection optics,* $\theta_{1/2}$.

to multiple scattering is determined to be between $10 - 60\%$. Uncertainty due to multiple scattering is observed to decrease with decreasing injection pressure, and at transverse locations further away from the spray centerline.

3.3 Comparison of Measured SMD Profiles from SAMR and USAXS Techniques

In order to evaluate the ability of the SAMR technique to quantify average droplet sizes in diesel sprays, the measured SMD profiles are compared with available measurements from the newly available USAXS measurements. The salient features of the USAXS measurements are first noted. Then, the SAMR technique is cross-validated with the USAXS measurements.

3.3.1 Evaluation of USAXS SMD Measurements

The USAXS measurements quantifying the SMD distribution along the spray centerline, as shown in Figure 2.7, were conducted under the Case $1 - 3$ conditions defined in Table 2.3. The measurements begin 1 mm from the nozzle and extend downstream

along the centerline.

In general, the SMD measurements indicate large droplets in the near nozzle region that rapidly decrease in size due to simultaneous spray and droplet breakup processes. As can be seen in Figure 2.7 for the Case 1 condition (150 MPa, 22.8 kg/m^3), the measurement indicates a rapid decrease in SMD within 4 mm of the injector nozzle exit. This suggests that the initial breakup process does not occur immediately at the injector exit, but occurs over a fine amount of time and distance. The length of the breakup region is a salient feature of the spray that has not been well characterized by previous experimental measurements and can significantly improve model validation accuracy, as will be explored in Chapter 4. For example, faithful representation of the size and shape of the spray breakup region over a range of ambient and injection conditions would suggest that the timescale and rate of spray disintegration characterizing the primary spray breakup process are well captured by the model. These USAXS measurements provide detailed quantification of the atomization process in this region for the first time.

Downstream of the breakup region, the measured SMD reaches a minimum value that remains relatively constant with increasing axial distance. The stable SMD region could be caused by two possibilities. The first possibility is that following the primary spray breakup process, the formed droplets do not undergo any further change in size, via secondary breakup, collisions or coalescence. The second possibility is that processes such as secondary breakup and/or collisions of the droplets, which serve to decrease the droplet size, are equally balanced by increase of droplet size due to coalescence of colliding droplets. In Chapter 4, these newly-available measurements of the minimum SMD are used as an effective calibration target to assess the predictive capability of spray atomization models, and to evaluate the likelihood of each of these scenarios.

For the Case 2 condition (50 MPa, 22.8 kg/m^3), a similar trend is observed within

the breakup region, where the SMD is seen to rapidly decrease with increasing distance from the nozzle exit. Following this region, larger SMD values are observed relative to the distribution measured under the Case 1 condition (150 MPa). This relative increase in SMD with decreasing injection pressure may be due to the combined effect of droplet coalescence, aerodynamic drag forces, and the momentum of larger droplets surpassing slower moving neighboring droplets [70]. As will be discussed in Chapter 4, comparison with modeling results that include or exclude the effect of droplet collisions and coalescence over a range of conditions can provide insight into the physical explanation of this observed trend.

For the Case 3 condition (150 MPa, 7.6 kg/m^3), the decrease in SMD in the near-nozzle region is not as rapid as is seen for the other two conditions. It is interesting to note that although there are clear differences within the spray breakup region when the ambient density is parametrically varied from the baseline condition of 22.8 kg/m^3 to 7.6 kg/m^3, the stable droplet size formed in the downstream portion of the spray is nearly identical to that of the baseline condition. This trend suggests that the minimum SMD is independent of changes in ambient density for the range of densities explored in this work. The indicated insensitivity of the spray structure to changes in ambient density in the downstream portion of the spray serves as another target metric to assess the predictive capability of a given spray model within the evaluated range of ambient density ($7.6 - 22.8$ kg/m^3) and injection pressure ($50 - 150$ MPa) conditions.

3.3.2 Cross-Validation Between SAMR and USAXS Techniques

SMD measurements from the SAMR technique are now compared with USAXS measurements, as shown in Figure 3.7 for the Case 1 and Case 2 conditions defined in Table 2.3. The comparison is conducted at an axial location of 8 mm from the injector nozzle exit, where the transverse location at 0 mm indicates the spray centerline. In

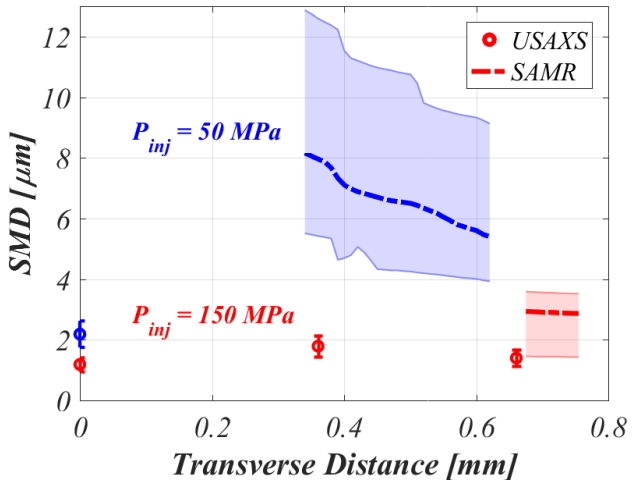

Figure 3.7: *Comparison of measured radial distributions of SMD for the USAXS and SAMR measurement techniques at two different injection pressures (50 and 150 MPa). The distributions are shown for a location of 8 mm from the injector nozzle exit.*

general, the measured SMD shows a decrease in droplet size with increasing radial distance, with a stronger radial gradient observed for the lower injection pressure condition (50 MPa). Enhanced spray breakup is seen for the higher injection pressure condition, as indicated by the decrease in SMD along the periphery of the spray. Although the USAXS measurements were sparsely sampled across the width of the spray at the higher injection pressure condition, some limited comparison is available between the USAXS and SAMR measurements at the Case 1 condition. Along the periphery of the spray, the SAMR measurements indicate a larger magnitude but similar gradient in the SMD distribution. The sources of the differences are likely due to measurement uncertainties due to relative positioning within the spray and injector orientations, as well as errors introduced from multiple scattering events. Future work should focus on reducing uncertainty in both the relative measurement position and injector orientations, and better quantifying expected multiple scattering errors for the investigated spray conditions and measurement system.

Although there are regions of the interior of the spray that are not suitable for the SAMR technique, the strength of the measurement is based on its inherent ability

to complement the somewhat limited data sampling of the USAXS measurements. Leveraging USAXS and SAMR measurements jointly shows the potential for a comprehensive evaluation of SMD throughout the spray. Figure 3.7 also shows that SAMR measurements can provide useful measurements of SMD independent of available USAXS measurements (Case 2). Furthermore, because both the XRR and laser extinction measurements represent path-integrated quantities, it is also possible to employ computed tomography to obtain information about the internal structure of the spray. Such information is particularly useful when studying asymmetric or multi-hole sprays. Future work should investigate the use of tomography to evaluate 3D distributions of SMD within the spray from the SAMR technique.

In summary, USAXS measurements conducted by researchers at Argonne National Laboratory [64] were presented and provided new information about the spatial evolution of SMD in the near nozzle region, along the spray centerline, and within the core of the spray. To provide complementary information about droplet sizes along the periphery of the spray, and at conditions where USAXS measurements were not available, a new measurement technique was proposed and demonstrated that quantifies SMD from the ratio of path-integrated x-ray and visible laser extinction measurements. The scattering absorption measurement ratio (SAMR) technique yields a quantity that is proportional to the SMD of the droplet size distribution within the probed volume. The SMD can be determined by employing theoretical Mie-scatter calculations to determine the number-weighted mean extinction cross section, $\overline{C_{ext}}$, and number-weighted mean droplet volume, $\overline{\pi\, d^3/6}$, that yields the measured SAMR. SAMR measurements indicated larger SMD values but similar radial gradients in SMD along the spray periphery than available USAXS measurements. These discrepancies are likely related to: 1) uncertainties in measurement position within the spray and relative injector orientation between the XRR and laser extinction measurements, due to the execution of these measurements at two different experimental

facilities; and 2) multiple scattering errors in regions where $\tau > 1$, which serve to artificially increase the SMD calculated from the SAMR technique. Future work will focus on reducing these uncertainties and better quantifying multiple scattering errors in the measurement system.

Additionally, evaluation of the USAXS measurements revealed two key features of the spray. Firstly, in the near nozzle region, a rapid decrease in droplet size was measured, and is likely related to the initial breakup of the spray into droplets. Second, at the highest injection studied in this work (150 MPa), a stable droplet size was formed in the downstream portion of the spray. Available measurements suggest that the minimum SMD is insensitive to changes in ambient density. The rate of SMD decrease in the spray breakup region and the minimum SMD formed are two recommended features that should be matched when calibrating and validating model to ensure faithful representation of the measured spray. The newly available USAXS and SAMR measurements will be employed in Chapter 4 to assess the predictive capability of existing aerodynamic-induced spray breakup models to capture the experimentally observed trends.

CHAPTER 4

ASSESSMENT OF EXISTING SPRAY MODELS UNDER CONVENTIONAL DIESEL OPERATING CONDITIONS

One of the largest sources of uncertainty for modeling high-pressure fuel sprays under engine-relevant conditions is the spray breakup process. The physical mechanisms governing the spray and droplet formation processes are still largely unknown due to the difficulty in experimentally observing this multi-scale and multi-physics process. The measured SMD distributions from the USAXS and SAMR measurement techniques, previously discussed in Chapter 3, offer a new opportunity to evaluate the appropriateness of the commonly employed KH aerodynamic-induced spray breakup model, and the ability of selected spray sub-models, such as secondary droplet breakup and droplet collisions, to predict experimentally observed trends in the spray structure. A computational study was conducted to investigate the possible spray and droplet phenomena governing the measured spray structure under conventional diesel operating conditions. This work has been detailed in published works by the author, and are shown here for posterity [85, 86].

4.1 Evaluation of Aerodynamic-Induced Spray Breakup Model Predictions

Throughout the fuel sprays literature, there are conflicting theories used to explain the experimentally observed trends in SMD distributions. It is a challenge to identify the correct physics influencing droplet size distributions using experiments alone. To help shed light on experimental SMD trends seen in the USAXS and SAMR measurements, previously shown in Figures 2.7 and 3.7, a computational study was conducted

to evaluate the effect of model calibration and different droplet phenomenon on the predicted structure for a range of ambient and injection conditions, as defined in the Case 1 - 3 conditions in Table 2.3. Several KH spray modeling set-ups, as detailed in Section 2.1, were employed with and without the inclusion of spray sub-models such as secondary droplet breakup via the KH-RT model [17], and droplet collisions and coalescence using the O'Rourke collisions model [107] with Post outcomes [109]. The capabilities of the models to replicate trends in SMD along the spray centerline and across the width of the spray, as detailed in Chapter 3, were evaluated. In particular, the first trend of interest was the extent by which the centerline distribution of SMD was seen to increase as the injection pressure is decreased (from 150 to 50 MPa), as indicated in the USAXS measurements in Figure 2.7. The second trend of interest was the bi-modal transverse SMD distribution for the Case 1 condition at a location 8 mm downstream from the nozzle exit, as suggested by the USAXS and SAMR measurements in Figure 3.7. These measurements offer excellent test cases for model validation because a single calibrated spray model set-up, which incorporates all of the relevant physics, should exhibit the correct spatial evolution and response of droplet size to changes in injection pressure and ambient density.

4.1.1 Influence of Spray Model Calibration on Predicted Spray Structure

A study on the calibration of the KH primary spray breakup model and its impact on the predicted spray structure was conducted at the baseline non-vaporizing Spray A (Case 1) condition. This condition was selected in particular because the largest amount of experimental data was available to characterize the global and local characteristics of the spray, namely the spray penetration and detailed SMD distribution. Conventional spray model validation practices employ the measured liquid penetration as the target spray feature to be matched, as shown in Figure 4.1 for the baseline non-vaporizing Spray A condition. Although the differently calibrated spray models

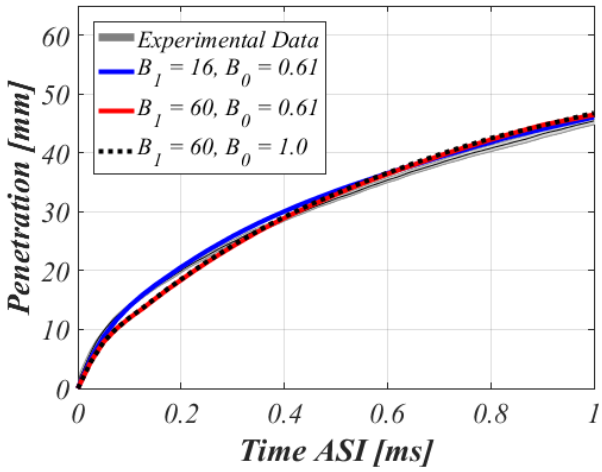

Figure 4.1: *Comparison of liquid penetration data, including measured standard error, from Sandia National Laboratories [113] with model predictions of liquid penetration.*

are expected to produce unique spray structures, all models produce similar spray penetration curves. This trend is expected since spray penetration is largely determined by the momentum exchange between the spray and ambient environment, which can be ensured through accurate boundary conditions for the rate of injection and initial conditions for turbulence modeling [9]. Some discrepancies are seen between spray penetration predictions from models employing larger B_1 constants ($B_1 = 60$) during the initial injection transients. This difference is due to initially larger predicted dispersion, which results in smaller axial velocities and therefore smaller penetration during the start of injection period. However, all spray models predict similar spray penetration within the steady portion of injection (0.5 to 1.0 ms) where the injection velocity is nominally constant. Within this injection period where all models exhibit similar global spray behavior, the predicted spray structure is evaluated in closer detail in comparison to available SMD measurements to identify potential modeling deficiencies.

Comparison of the calibrated spray models to the USAXS measurements highlights the influence of spray model "tuning" constants on the predicted spray structure, as shown in Figure 4.2. All spray model predictions shown here are for models employing

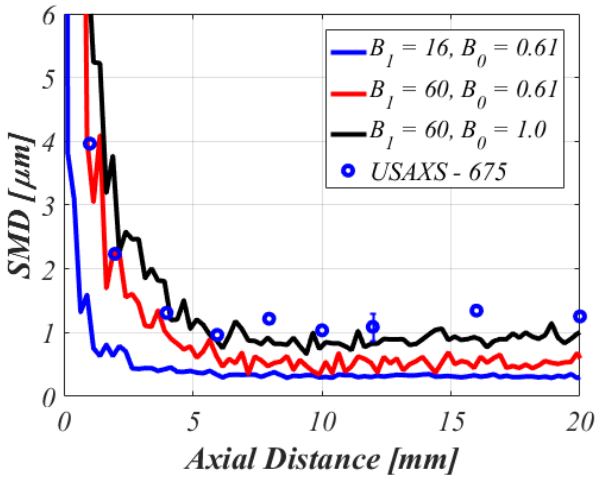

Figure 4.2: *Comparison of calibrated KH-RT spray models with measured axial distributions of SMD at the Case 1 condition ($P_{inj} = 150\,MPa$ and $\rho_{amb} = 22.8\,kg/m^3$) along the spray centerline. The spray model predictions do not include the effects of collisions.*

the KH-RT spray breakup model without the influence of droplet-droplet collisions. In general, all models exhibit a rapid decrease in the centerline SMD in the near nozzle region and then achieve a stable droplet size in downstream portions of the spray. Two spray breakup models constants were shown to have a significant influence on the SMD distribution: B_0, the KH primary breakup droplet size constant, and B_1, the KH breakup time constant, as defined in Equations 1.12 and 1.11, respectively. Recommended spray model constants for diesel sprays are typically $B_0 \sim 0.61$ and $B_1 \sim 7$ [13]. As is evident in Figure 4.2, increasing B_1 serves to elongate the breakup process and spatially delay the location where the minimum SMD is achieved. The smallest employed B_1 constant in this study ($B_1 = 16$), more than double the conventionally recommended value, results in a much shorter breakup region than what is indicated in the USAXS measurements. By increasing the employed B_1 constant to 60, thereby slowing down the modeled breakup process, better agreement is achieved between the model and measured drop size decrease within the spray formation region. Employing a standard B_0 value of 0.61 results in an underprediction of the stable droplet size, while increasing B_0 to 1.0 results in improved agreement between

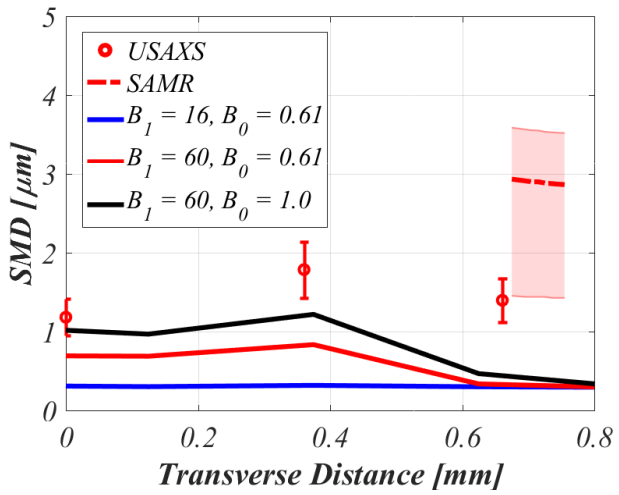

Figure 4.3: *Comparison of calibrated KH-RT spray models with measured radial distributions of SMD at the Case 1 condition ($P_{inj} = 150\,MPa$ and $\rho_{amb} = 22.8\,kg/m^3$). The comparison is conducted at an axial location of 8 mm downstream of the injector. The spray model predictions do not include the effects of collisions.*

predicted and measured minimum SMD along the spray centerline. This result suggests that stable droplet size distributions are best represented when droplet sizes produced by KH breakup are assumed to be directly proportional to Λ_{KH}.

To comprehensively evaluate the success of a given calibrated spray model to predict spray structure details, it is important to evaluate not only the SMD distributions along the spray centerline, but also across the width of the spray. In Figure 4.3, predicted radial SMD distributions are compared to the USAXS and SAMR measurements at an axial location of 8 mm from the nozzle exit. The USAXS measurements suggest a bi-modal distribution, with a local minimum in SMD ($\sim$ 1.2 μm) along the spray centerline and a maximum SMD ($\sim$ 1.8 μm) some radial distance away from the spray centerline. The SAMR and USAXS measurements along the periphery of the spray indicate larger droplet sizes than predicted by any of the models.

Figure 4.3 shows that the calibration of the spray breakup model constants also influences the characteristic shape of the droplet size distribution. The model with the fastest breakup timescale ($B_1 = 16$) predicts a relatively flat SMD distribution across the width of the spray, whereas the spray models employing slower breakup timescales

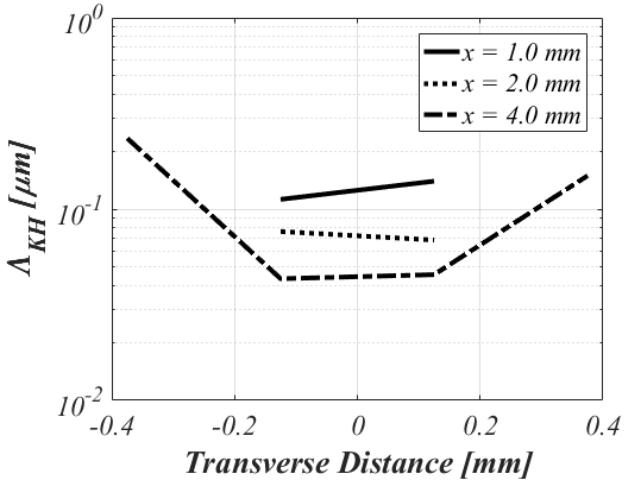

Figure 4.4: *Comparison of radial distributions of Λ_{KH} at various axial locations in the near nozzle region. Predictions are based on the local conditions from the $B_1 = 60, B_0 = 1.0$ spray model.*

($B_1 = 60$) predict a bi-modal SMD distribution that closely resembles the shape indicated by the USAXS measurements. The influence of the spray model calibration on the radial SMD distribution can be explained by evaluating the spatial history of Λ_{KH}, as shown in Figure 4.4. The distributions of Λ_{KH} are calculated using the time-averaged local We_g, and number-weighted mean T and Oh of the spray parcels. Λ_{KH} controls the primary breakup rate through modulation of the formed droplet size, r_c, as defined in Equation 1.12. At each instance in time, a fuel parcel travels through a range of We_g which will affect Λ_{KH} and therefore r_c of the parcel. As is shown in Figure 4.4, the distribution of Λ_{KH} at 1 mm from the injector is relatively constant across the width of the spray. This trend remains consistent for the distribution at 2 mm away from the nozzle exit as well. If the primary breakup process is completed within this near nozzle region, then all parcels across the width of the spray would experience similar primary breakup processes and form similar primary droplet sizes. For the spray model with a B_1 constant of 16, which represents relatively fast breakup, the breakup process is complete within the first 2 mm of the spray, as is indicated in Figure 4.2. As a result, the flat radial distribution of Λ_{KH} within 2 mm of the

injector nozzle suggests that a constant SMD distribution across the width of the spray is expected in the downstream portions of the spray, which is confirmed for this model in Figure 4.3. Figure 4.2 also shows that as the B_1 calibration constant is increased, the primary breakup region is elongated and the minimum SMD is formed further downstream. At a distance of 4 mm from the nozzle exit, larger differences in Λ_{KH} can be seen across the width of the spray in Figure 4.4. In general, larger Λ_{KH} are predicted along the periphery of the spray due to smaller relative droplet velocities and We_g. As a result, for conditions where the primary breakup process is slower, fuel parcels across the width of the spray can undergo different spray breakup processes and ultimately form different stable droplet sizes, which would result in a non-uniform droplet distribution, as is seen in Figure 4.3.

It is interesting to note the potential implications of these modeling results when interpreting radial distributions of droplet size measurements. For high injection pressures, where spray model predictions suggest the droplet collisions may not dictate the measured droplet size distribution in downstream portions of the spray (Figure 2.7), the shape of the predicted radial SMD distribution was shown to be influenced by the primary breakup process rate (Figure 4.3). Model predictions from this calibration study indicate that flat distributions of droplet size across the width of the spray can be indicative of fast primary breakup processes (blue line), whereas slower primary breakup led to non-uniform SMD distributions (black line). For carefully selected measurement locations downstream of the primary breakup region where other processes such as coalescence or large scale mixing have not influenced the droplet size distribution, SMD measurements across the width of the spray may serve as indirect validation metrics for the primary breakup process.

4.1.2 Influence of Spray Sub-Model Selection on Predicted Spray Structure

To assess the predictive capability of a spray model, the predicted spray structure must be tested and compared to spray measurements over a range of conditions. Under the Case 1 condition, comparison between measured and predicted SMD distributions suggests that the optimal spray model set-up is a KH-RT spray breakup model with a relatively slow breakup timescale ($B_1 = 60$) that forms droplets that are directly proportional to Λ_{KH} ($B_0 = 1.0$) and do not undergo collisions. Extending the comparison to a range of injection and ambient density conditions allows the response of the model to be evaluated. If a single calibrated spray model set-up is able to match the experimental measurements at a single condition, as well as the trends over a range of conditions, one could have confidence that the model employs all of the key physics that govern the spray structure. In this section, predictions from the KH-RT spray model set-up ($B_1 = 60$ and $B_0 = 1.0$) without collisions are compared with USAXS and SAMR measurements over a range of injection and ambient conditions. In addition, the influence of selected droplet sub-models on the predicted SMD distribution is assessed. In particular, the trends in predicted SMD along the spray centerline and across the spray width are evaluated when secondary droplet breakup via the RT breakup mechanism, and droplet collisions and coalescence, modeled using the O'Rourke formulation, are included or excluded in the spray model.

Comparison of the measured and predicted SMD distributions along the spray centerline for the calibrated model with $B_1 = 60$ and $B_0 = 1.0$ is shown in Figure 4.5 for the (a) Case 1, (b) Case 2 and (c) Case 3 conditions. As previously discussed, the KH-RT spray model without the influence of collisions (solid line) is able to represent the measured centerline SMD distribution for the Case 1 condition as shown in Figure 4.5(a). When the injection pressure is decreased to 50 MPa, the predicted droplet size distribution shown in Figure 4.5(b) exhibits a slight increase in SMD that is consistent with the measurements. Because no droplet-droplet collisions are mod-

eled, increasing SMD with axial distance is due to the momentum of larger droplets overtaking slower neighboring droplets. When the effects due to droplet collisions are included (dotted line), a substantial increase in droplet size with increasing distance from the nozzle is predicted for the Case 2 condition (Figure 4.5(b)) due to coalescence governing the resultant SMD in downstream regions of the spray. Although a collision model might be able to replicate experimentally measured SMD at a single condition, in general, the inclusion of droplet collisions results in overprediction of coalescence events and droplet sizes in downstream portions of the spray that is inconsistent with the USAXS measurements. These results suggest that collisions cannot explain the experimentally observed trend in centerline SMD distribution with respect to changes in injection pressure.

The ability of a coalescence model to explain the experimentally observed sensitivities of droplet size distributions with respect to changes in injection pressure is further investigated through comparison of predicted and measured radial SMD distribution at 8 mm from the injector nozzle exit at the Case 2 condition, as shown in Figure 4.6. The model predictions are shown for the spray model employing the KH model constants of $B_1 = 60$ and $B_0 = 1.0$. Although the predicted SMD agrees with the USAXS measurement at the spray centerline, the local maximum in the radial SMD distribution is slightly underpredicted in comparison to the SAMR measurements. Overall, the KH-RT spray model without the influence of droplet collision outcomes (solid line) predicts a bi-modal radial SMD distribution that is the consistent with the shape suggested by the available USAXS and SAMR measurements. However, when the influence of droplet collisions is included (dotted line), the spray model predicts relatively larger droplets near the spray centerline due to the occurrence of coalescence. Additionally, the predicted radial SMD distribution exhibits a steeper gradient in SMD along the periphery of the spray than is indicated by the SAMR measurements. Although no exact agreement is obtained between the

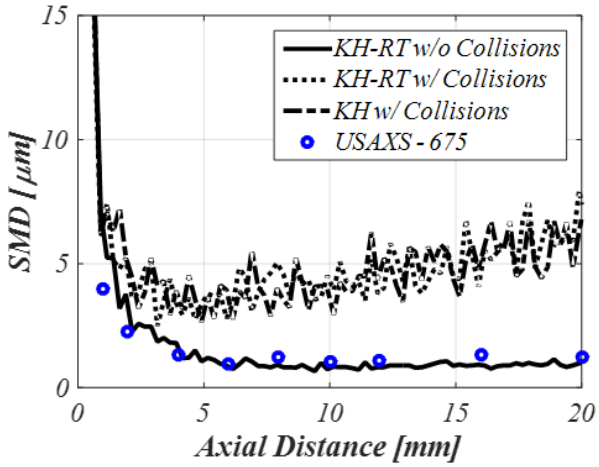

(a)

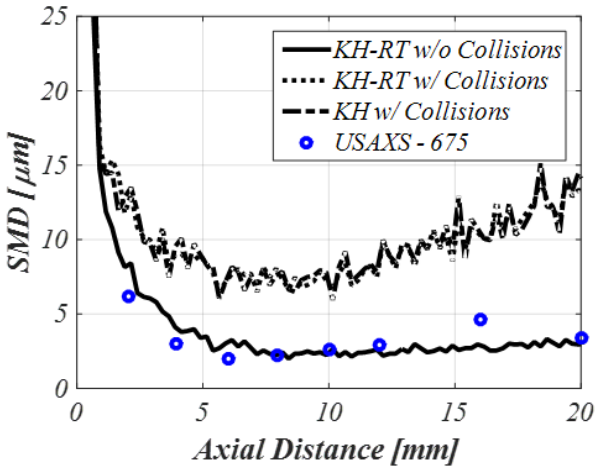

(b)

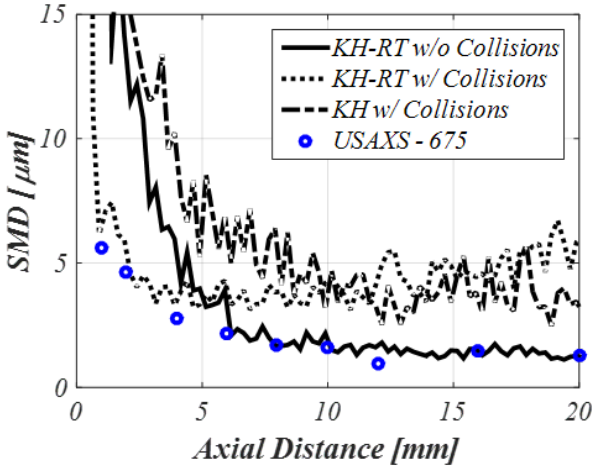

(c)

Figure 4.5: *Comparison of different selected spray models with measured axial distributions of SMD at the (a) Case 1, (b) Case 2 and (c) Case 3 conditions. The comparison is conducted along the spray centerline for the spray model employing the KH spray model constants* $B_1 = 60$ *and* $B_0 = 1.0$.

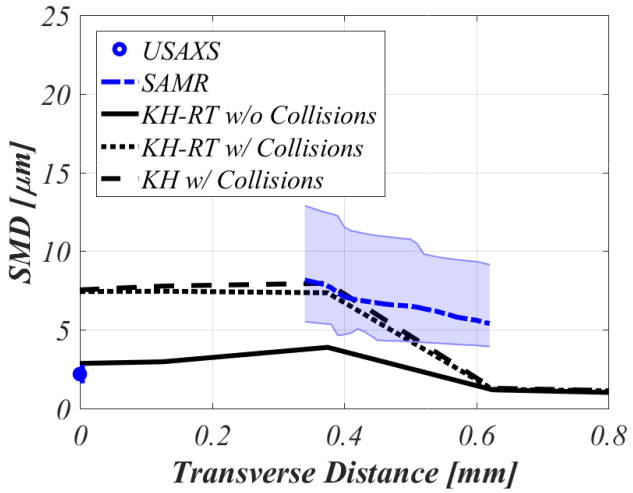

Figure 4.6: *Comparison of calibrated KH-RT spray models with measured radial distributions of SMD at the Case 2 condition ($P_{inj} = 50\,MPa$ and $\rho_{amb} = 22.8\,kg/m^3$). The comparison is conducted at an axial location of 8 mm downstream of the injector for the spray model employing the KH spray model constants $B_1 = 60$ and $B_0 = 1.0$.*

model predictions and the SAMR measurements, the KH-RT spray model without the effects of droplet collisions yields the best agreement with the available SMD data across the width of the spray. However, additional USAXS measurements are required within the central region of the spray in order to draw a more conclusive assessment on the accurate modeling approach for this condition.

The influence of the secondary droplet breakup via the RT instability mechanism (dashed line) on the centerline (Figure 4.5) and radial SMD distributions (Figure 4.6) was also tested for the KH-RT model including droplet collisions. The spray model set-up with collisions was selected in particular because droplet sizes are expected to be large enough to be unstable to the RT instability mechanism. As shown in Figure 4.5(a) and (b), the RT secondary droplet model has minimal impact on the centerline SMD distribution, regardless of the injection pressure. Evaluation of the radial SMD profile in Figure 4.6 reveals that the effectiveness of RT secondary breakup is dependent on transverse position. For distances close to the centerline of the spray, the RT secondary breakup mechanism is observed to minimally affect the SMD profile. However, further away from the spray centerline, RT secondary breakup results

in decreased SMD, although the reduction in droplet size is less than 8%. As a result, it can be deduced that the ability of the KH-RT model to capture the sensitivity of the SMD distribution to changes in injection pressure is predominantly due to the KH primary and secondary breakup model, as opposed to the RT secondary breakup model. Therefore, the KH spray breakup model, in isolation of RT secondary breakup and droplet collisions, well represents the experimentally observed trends of SMD throughout the spray.

A well-calibrated KH-RT model without the influence of collisions can also capture many of the experimentally observed features in the centerline SMD distributions when the ambient density is parametrically varied, as shown in Figure 4.5(a) and (c). When the ambient density is decreased from 22.8 to 7.6 kg/m^3, predictions from the KH-RT model without droplet collisions agree well with the USAXS measurement. In particular, spray predictions at the Case 1 and Case 2 conditions, shown in Figure 4.5(a) and (c) respectively, capture the measured minimum SMD in the downstream portion of the spray, and the insensitivity of the minimum SMD to changes in ambient density. Additionally, the lengths of the predicted and measured breakup region are observed to similarly increase with decreasing ambient density.

It is worth noting that other computationalists have adopted a similar modeling approach in previous publications, where collision modeling is neglected in the simulation of diesel sprays. For example, Lucchini and co-workers [137] exclude collision modeling in their simulations of vaporizing diesel sprays under similar ambient density condition (14.8 kg/m^3). They justify this approach by pointing to experimental measurements of Sauter Mean Radius (SMR) within evaporating diesel sprays that indicate minimal influence of collisions on the resultant spray structure [138]. Though the measurement and simulation conditions considered in this study are for non-vaporizing sprays, the simulation results indicate the inability of collision models to capture the experimentally observed trends in spray structure, and therefore

suggest a similar modeling approach.

Although the KH-RT spray model can capture many of the experimentally observed trends, the presented results do not confirm that the Kelvin Helmholtz mechanism completely describes the initial spray breakup process under all conditions. In fact, several of the details of the model predictions suggest that KH is not likely the only mechanism influencing the primary breakup process. Although the initial spray formation region is well captured by the carefully calibrated model ($B_1 = 60$ and $B_0 = 1.0$) for the Case 1 and Case 2 conditions, as shown in Figure 4.5(a) and (b), discrepancies between the predicted and measured spray structure in the near nozzle region can be seen for the Case 3 condition with a lower ambient density, as shown in Figure 4.5(c). While the minimum SMD and length of the spray breakup region are well captured by the model, the rate at which droplet sizes decrease within the spray breakup region is underpredicted and results in the prediction of larger SMD in the near-nozzle region and smaller droplet sizes along the spray periphery than indicated in the measurements. These results might suggest that the KH mechanism cannot predict the correct trend in isolation, and that other primary breakup mechanisms likely augment the breakup process in diesel sprays.

4.2 Implications for Modeling Spray Breakup in the Merged Aerodynamic Primary and Secondary Breakup Regime

The results from this computational study informed recommendations for modeling primary breakup in diesel sprays within the merged aerodynamic primary and secondary breakup regime, as defined by Wu and Faeth [18]. In summary, when considering the comparison of both centerline and radial SMD predictions against the USAXS and SAMR measurements, the spray structure details were best represented by the spray model that excluded the effects of droplet collisions and was calibrated

with KH breakup constants $B_1 = 60$ and $B_0 = 1.0$. This spray model represents slower spray breakup and larger formed droplets than is conventionally recommended for modeling diesel sprays. These results suggest that the influence of aerodynamics on the primary breakup process can be represented via an aerodynamic wave growth model, namely the KH spray breakup model [17].

For injection into lower ambient density conditions, turbulence generated within the injector nozzle may augment aerodynamic spray breakup. Under such conditions, nozzle-generated turbulence may more strongly affect the resultant spray structure since aerodynamic inertial forces are expected to be reduced. To evaluate the role of nozzle-generated turbulence on the spray breakup process, the influence of the assumed turbulent scaling within a primary atomization model on the predicted spray structure is evaluated in Chapter 5, and compared with available experimental measurements in Chapter 6.

CHAPTER 5

EXPLORATION OF TURBULENT ATOMIZATION MECHANISMS FOR DIESEL SPRAY SIMULATIONS

In order to formulate a hybrid spray breakup model that can accurately represent the role of turbulence in the primary atomization process, the length and time scales characterizing the turbulence-induced breakup process must be known. However, under diesel-relevant conditions, these scales are unknown due to the experimental challenges of directly observing and quantifying this process. Therefore, spray modeling studies that explore the influence of the employed primary atomization model and assumed scalings on the predicted spray structure, in concert with comparison against available spray measurements, could help inform the correct modeling approach. In order to identify the strengths and deficiencies of existing spray breakup models, the response of the predicted spray structure to changes in injection and ambient conditions from purely aerodynamic (KH) and hybrid turbulent and aerodynamic (KH-ACT) breakup models are evaluated. Additionally, using the KH-ACT modeling framework described in Section 1.2.3.3, the influence of the assumed turbulent scaling of the primary breakup model is assessed by replacing the existing breakup length and time scales with empirical correlations developed by Wu and Faeth [18]. This newly developed model, called the KH-Faeth model, is described in this chapter. Using local sensitivity analysis, the response of the predicted spray structure are compared among the three primary atomization models, and the relationship of the selected response metrics to the employed primary atomization model is evaluated. This work has been detailed in a published work by the author, and is shown here for posterity [88].

5.1 Experimental Spray Model Validation Data

The wide range of injection and ambient conditions used in this work to study the spray structure of non-vaporizing diesel sprays are detailed in Table 2.3. Two single-hole injectors from the Engine Combustion Network (ECN), namely the Spray A and Spray D injector nozzles as detailed in Table 2.2, are simulated [113, 115, 139]. All experiments were based on the use of nominally-matched single-orifice axial spray injectors, available to participants of the ECN. Rate-of-injection (ROI) measurements [114, 131], as shown in Figure 2.14, are used to define the boundary conditions for the Spray A and Spray D injectors. Liquid penetration data [113], discussed below, and USAXS measurements [64], as shown in Figure 2.7 and described in Section 3.3.1, are used for primary atomization model assessment.

5.1.1 Liquid Penetration

Measurement of the liquid penetration, as shown in Figure 5.1, was conducted for the ECN Spray A nozzle #210677, under the reference Case 1 condition of $\rho_f/\rho_g = 32$ and $P_{inj} = 150$ MPa. The liquid penetration data was obtained by researchers at Sandial National Laboratories using the Schlieren technique in their constant volume spray vessel [113]. Further details regarding the experimental set-up and spray vessel are detailed in the previous works from Sandia National Labs [140]. Although the spray was injected into a slightly higher ambient temperature (440 K) environment than the modeled ambient condition (303 K), the ambient temperature is still lower than the boiling temperature for n-dodecane (489 K at 1 bar), and therefore the effects of vaporization on the spray penetration are expected to be minimal. Therefore, the measured liquid penetration can be used for comparison against model predictions at the reference condition, as will be shown and discussed later, to ensure that the momentum exchange between the liquid phase fuel and ambient gases is well captured

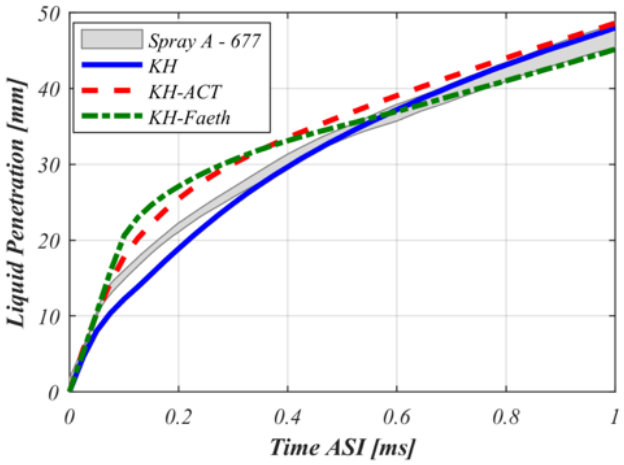

Figure 5.1: *Comparison of measured liquid penetration [113] against predicted liquid penetration for all three spray models based on* 99% *accumulated mass metric at* $\rho_f/\rho_g = 32$*,* $P_{inj} = 150$ *MPa for the ECN Spray A nozzle.*

by each of the spray models.

5.2 Computational Spray Modeling

Three different primary atomization models are evaluated, namely KH, KH-ACT and the newly developed KH-Faeth model, in order to evaluate the influence of atomization on predicted spray structure throughout the spray. The description of the CFD spray model set-up can be found in Section 2.1, but a summary is provided here. The commercial CFD code, CONVERGE [13], was utilized to simulate the injection of an n-dodecane spray into a constant volume chamber at non-vaporizing conditions, as listed in Table 2.3. The spray combustion chamber was modeled using a three-dimensional hexahedral structured mesh, as previously shown in Figure 2.1. The ROI profiles for the Spray A injector [114,131] and for the Spray D injector, shown in Figure 2.14, and nozzle discharge coefficients, C_d, listed in Table 2.2, were used to calculate the injection velocities at the nozzle exit. Three different models to represent the spray primary atomization process are evaluated in this work, namely the Kelvin-Helmholtz (KH) aerodynamic-induced breakup model [16], the KH-Aerodynamics-

Cavitation-Turbulence (KH-ACT) hybrid primary atomization model [45], and the newly developed KH-Faeth hybrid primary atomization model. The formulations for the KH and KH-ACT models can be found in Section 1.2.3, while the formulation for the KH-Faeth will be described below. For all spray models, secondary droplet breakup is modeled using the KH model and droplet collisions are neglected. As a result, these three spray models are therefore identical in set-up, except for the employed primary atomization sub-model.

5.2.1 KH-Faeth Primary Atomization Modeling Formulation

In order to understand the sensitivity of the predicted spray structure to the representation of the turbulence-induced breakup process, a new hybrid primary atomization model, called the KH-Faeth model, was developed. The KH-Faeth model was developed from the KH-ACT modeling framework [45], where the competition between aerodynamic and turbulent breakup mechanisms on the primary atomization process is treated identically. However, in the KH-Faeth model, the turbulent breakup length and time scales are modeled using empirical correlations from the work of Faeth and co-workers [18]. The salient conclusions of their work that support their correlation are highlighted here.

Based on an extensive database of near-nozzle holography imaging measurements across a wide range of Re_f ($9 \cdot 10^4 - 5.3 \cdot 10^5$) and ρ_f/ρ_g (104 - 6230) conditions, Faeth and co-workers developed a phenomenological framework to describe the onset of turbulent breakup and subsequent droplet formation process for round turbulent liquid jets injected into quiescent gases. For liquid jets injected into atmospheric conditions, they found that breakup scaled purely with the nozzle exit turbulence properties. However, for ρ_f/ρ_g less than 500, they found that aerodynamic effects can enhance spray breakup. They hypothesized that this enhanced breakup occurs due to a local reduction in pressure due to acceleration of the ambient gas

over surface protuberances that originate from liquid turbulence, akin to flow over a sphere [18]. Note that this mechanism of aerodynamically-enhanced breakup is distinct from the aerodynamically-induced breakup mechanism of surface wave development and growth that is represented in the KH breakup model. Using an energy balance between the mechanical energy at the liquid surface due to aerodynamic effects, the kinetic energy from the turbulent velocity fluctuations, and the surface energy at the instant of droplet formation, it was found that the measured size of ligaments and droplets formed, L_{Faeth}, were of the same order as estimated eddy scales within the inertial sub-range of the turbulence spectrum. It should be noted that this correlation will therefore result in the formation of droplets that are smaller than those predicted by the KH-ACT model, since in the KH-ACT model, the turbulent length scale is assumed to be proportional to the integral length scale.

Based on their analysis of the measured liquid surface ligament and droplet properties at the onset of turbulent breakup, the time required to form a droplet, τ_{Faeth}, was found to be proportional to the time required for a droplet to form from a ligament of size L_{Faeth}, according to the Rayleigh instability mechanism. For low Ohnesorge liquids, where viscosity effects can be neglected, Wu and Faeth [49] determined that $\tau_{Faeth} \propto \sqrt{\rho_f (L_{Faeth})^3)/\sigma}$. In the KH-Faeth model, a similar definition is implemented for τ_{Faeth}:

$$\tau_{Faeth} = C_\tau \sqrt{\rho_f \frac{L_{Faeth}^3}{\sigma}} \tag{5.1}$$

where C_τ is the turbulent breakup time constant, and σ is the surface tension of the liquid in the ambient gas. In the present study, C_τ is assumed to equal unity.

Wu and Faeth also developed a correlation to relate L_{Faeth} to nozzle exit turbulence properties and the axial location, x, where droplets are formed from the turbulent breakup process [18]. By assuming that the stream-wise velocity of the droplet-forming eddy remains relatively constant and can be equated to the injection

velocity, U_{inj}, x is simply equal to the product of U_{inj} and τ_{Faeth}. By using Equation 5.1 and re-arranging the terms, L_{Faeth} can be determined with the following relation:

$$\frac{L_{Faeth}}{\Lambda} = C_{sx}\left(\frac{x}{\Lambda We_{f\Lambda}^{1/2}}\right)^{2/3} \tag{5.2}$$

where Λ is the radial integral length scale, C_{sx} is an empirical constant, and $We_{f\Lambda}$ is the Λ-based liquid Weber number ($\rho_f U_{inj}^2 \Lambda/\sigma$). Based on experimental data across a wide range of Re_f ($9 \cdot 10^4$ –$5.3 \cdot 10^5$) and ρ_f/ρ_g (104-6230) conditions, Wu and Faeth determined that the empirical correlation in Equation 5.2 best fit the entire experimental data set when C_{sx} was set to 0.65. As a result, this relation is capable of representing the size of droplets formed across the non-aerodynamic and aerodynamic breakup regimes proposed by Wu and Faeth [18], as schematically shown in Figure 1.14.

In the KH-Faeth model, τ_{Faeth} and L_{Faeth} are used to represent the characteristic time and length scale governing the turbulence-induced primary breakup process. The turbulence-induced breakup model is implemented in a construct similar to the KH-ACT model. At each time step, only one primary atomization mechanism, either KH or turbulence-induced breakup, is assumed to act upon the computational parent parcel. KH and turbulent primary breakup rates are calculated and compared, and the maximum breakup rate is selected as the dominant primary atomization mechanism, as mathematically defined below,

$$\frac{L_A}{\tau_A} = max\{\frac{a - r_c}{\tau_{KH}}, \frac{L_{Faeth}}{\tau_{Faeth}}\}. \tag{5.3}$$

Similar to the KH-ACT atomization model, if KH primary breakup is dominant, then the parent parcels evolve according to Equation 1.10. However, if turbulent primary breakup dominates the atomization process, then the parent parcel decreases in size

according to Equation 1.25, where $C_{T,CAV}$ is equal to unity.

For each of the three spray model set-ups, after a child droplet has been formed from the selected primary atomization process, the droplet may undergo subsequent secondary droplet breakup due to the KH instability if the droplet size is larger than Λ_{KH}.

5.2.2 Spray Model Calibration Set-Up

Spray model constants, listed in Table 5.1, were tuned to match the predicted SMD distribution by the KH and KH-ACT models with the USAXS measurements along the spray centerline. Time-averaged two-dimensional SMD distributions were calculated by evaluating the droplet size distribution across the width of the spray within 0.25 mm wide bins from 0.7 to 1.0 ms ASI. Comparison between predicted and measured SMD at the reference Case 1 condition for the Spray A nozzle, where $\rho_f/\rho_g = 32$ and $P_{inj} = 150$ MPa, is shown in Figure 5.2(a). For the hybrid KH-Faeth atomization model, the model constants for the KH aerodynamic breakup model equations were set equal to those used in the KH and KH-ACT models. However, because the Faeth turbulent primary breakup model is based on an empirical correlation, where the empirical constant has been selected based on the best fit of experimental data spanning non-aerodynamic and aerodynamic primary breakup regimes [18], no additional model calibration constants were employed for the Faeth turbulent primary breakup model equations. At this single reference condition for the Spray A nozzle, the selected empirical constant results in an overprediction of the turbulent breakup rate relative to the predicted aerodynamic breakup rate, and ultimately underpredicts SMD. Because this reference condition occurs at a denser ambient condition than the conditions evaluated in the work of Faeth and co-workers ($\rho_f/\rho_g > 100$) [18], it could be expected that extrapolation of their empirical correlation would not yield good agreement with measurements at these conditions. Future work should investigate

Table 5.1: *Key spray model constants describing the three different spray model set-ups.*

Model Parameters	Model Calibration Constants
B_1	60
B_0	1
C_μ	0.09
$C_{T,CAV}$	0.33
C_τ	1
C_{sx}	0.65

calibration of the KH-Faeth model constants to better capture the relative influence of turbulence and aerodynamics on the primary breakup process under high back pressure conditions ($\rho_f/\rho_g < 100$).

It is important to ensure that the model set-ups well represent not only local spray details, such as SMD along the spray centerline, but also global spray features, such as liquid penetration. Comparison between the measured and predicted liquid penetration for the Spray A nozzle is shown in Figure 5.1. Ideally, as proposed in [83] for the vaporizing Spray "A" condition, a physically-based metric, such as the local liquid volume fraction, should be employed to define the computational liquid boundary for comparison against liquid penetration measurements. However, in absence of well-defined modeling practices for non-vaporizing sprays, the predicted liquid penetration was defined as the downstream axial location where 99% of the total injected mass has been encompassed. The model predictions of liquid penetration are within the experimental uncertainty of the measured liquid penetration within the steady portion of injection, from 0.7 to 1.0 ms after start-of-injection (ASI). This agreement indicates that the momentum exchange between the liquid phase fuel and ambient gases is well predicted within this time frame. It should be noted that during the early injection transient period, differences are seen among the predicted liquid penetration among the three models; this difference highlights the dependence of start of injection spray development on the details of the initial breakup process, consistent

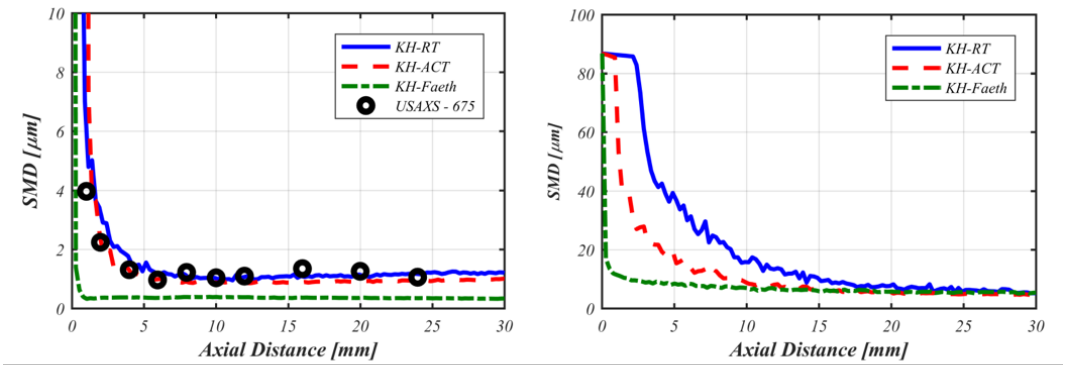

Figure 5.2: *Axial distributions of SMD along the spray centerline are compared among the three spray models for the Spray A nozzle at* $P_{inj} = 150$ *MPa and (a)* $\rho_f/\rho_g = 32$ *and at (b)* $\rho_f/\rho_g = 620$.

with the findings from Som [45]. However, since the computational study focuses on the study of predicted spray structure within the steady portion of injection (0.7 to 1.0 ms ASI), it is determined that each of the spray model set-ups represent similar global features of the spray.

5.3 Predictived Sensitivity of Selected Spray Models

The dependence of the predicted spray structure on the employed primary atomization model is evaluated. First, response metrics are identified that can efficiently characterize the predicted droplet size distribution throughout the spray to simplify the model analysis and comparisons of complex three-dimensional droplet field predictions. Then, using local sensitivity analysis, the prediction of these response metrics are compared among the three primary atomization models considered in this work to changes in injection and ambient conditions.

5.3.1 Identification of Response Metrics

In order to understand how the assumed primary atomization mechanism affects the predicted spray structure, it is desirable to identify simplified metrics that can

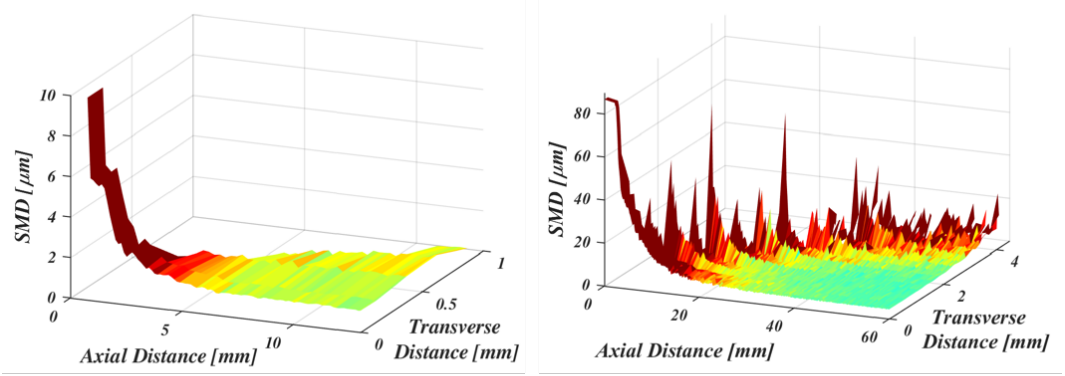

(a) (b)

Figure 5.3: *Sample 2-D time-averaged SMD map as predicted by the KH model for the Spray A nozzle at ambient and injection conditions of (a)* $\rho_f/\rho_g = 32$, $P_{inj} = 150$ *MPa and (b)* $\rho_f/\rho_g = 620$, $P_{inj} = 150$ *MPa. Only half of the spray is shown in order to clearly illustrate the difference in predicted SMD between the central and peripheral regions of the spray.*

enable insight into the behavior of the selected primary atomization model over a wide range of operating conditions. Additionally, the selected response metrics must also be directly comparable to available experimental measurements of droplet size. Example time-averaged SMD distributions, as predicted by the KH model for the ECN Spray A nozzle, are displayed in Figure 5.3. In Figure 5.3(a), the SMD distribution is shown for the Case 1 condition ($\rho_f/\rho_g = 32$, $P_{inj} = 150$ MPa). The droplets begin with diameter approximately equal to the nozzle diameter (89.4 μm) and quickly decrease in size due to primary atomization and secondary droplet breakup.

Along the centerline, the droplets eventually reach a stable droplet size near 6 mm from the nozzle exit. This behavior is also seen for the predicted SMD distribution even at the lower ambient density condition ($\rho_f/\rho_g = 620$, $P_{inj} = 150$ MPa), as shown in Figure 5.3(b), although the stable droplet size is not reached until approximately 40 mm from the nozzle exit. Similar to the experimental trends seen in the USAXS measurements in Figure 2.7 for ρ_f/ρ_g less than 100, and noted in Section 3.3.1, the minimum droplet size formed along the spray centerline, SMD_{min} is approximately equal to the stable droplet size. Therefore, to characterize the droplet size evolution in the central region of the spray, the minimum SMD (SMD_{min}) along the spray

centerline is selected as the target parameter for the basis of comparison among all three models, and with available USAXS measurements, as defined in Equation 5.4 below,

$$SMD_{min} = min\{SMD(x, y = 0)\} \tag{5.4}$$

where x is the axial distance from the nozzle, and y is the transverse distance, where $y = 0$ represents the spray centerline.

Along the periphery of the spray, the predicted droplet size distribution exhibits a sensitivity to changes in ρ_f/ρ_g that differs from the predicted SMD along the spray centerline. At the Case 1 condition as shown in Figure 5.3(a), the droplet sizes along the periphery of the spray are very similar to those along the centerline. As a result, the SMD distribution appears relatively "flat" throughout the spray. However, at higher conditions, this "flat" SMD distribution is not exhibited, as can be seen by the larger droplets along the periphery of the spray, relative to the centerline, in Figure 5.3(b).

There are several reasons why this change in droplet size behavior is seen at the higher ρ_f/ρ_g condition. As ρ_f/ρ_g is increased from 32 to 620, the primary atomization timescale increases, as illustrated by the relatively slower rate of SMD decrease along the spray centerline in Figure 5.3(b). At the $\rho_f/\rho_g = 32$ condition in Figure 5.3(a), the SMD along the centerline decreases by more than 95% of its initial size within the first 2 mm from the nozzle exit, whereas the SMD along the centerline decreases by less than 5% within the same distance at the $\rho_f/\rho_g = 620$ condition (Figure 5.3(b)). At 2 mm from the nozzle exit at the $\rho_f/\rho_g = 32$ condition, the primary atomization process has completed. Within this same distance, the velocity of the liquid jet has not developed substantially and is approximately uniform across the width of the spray. Therefore, as similarly noted in Section 4.1.1, all computational parcels across the width of the spray encounter similar local conditions and undergo similar subsequent

changes in droplet size due to secondary droplet breakup. As a result, the droplet size distribution across the width of the spray at downstream locations is relatively constant. In contrast, at the $\rho_f/\rho_g = 620$ condition, the primary atomization process is substantially elongated. Therefore, computational parcels across the width of the spray encounter different local conditions as they continue to decrease in size due to the development of the velocity profile of the spray. For example, parcels along the centerline of the spray have larger relative velocities and continue to undergo secondary droplet breakup. However, along the periphery of the spray, the relative velocities of the parcels approach zero, which results in nearly infinite droplet breakup times, and serve to "freeze" the droplet sizes. Therefore, relatively larger droplet sizes can be seen along the periphery of the spray in comparison to those along the spray centerline.

These results suggest that in absence of droplet interactions, droplet size distributions across the width of the spray may provide indirect indication of the primary atomization process, as previously noted in Section 4.1.1. Similar droplet sizes in the central and peripheral regions of the spray were formed from a fast primary atomization process. In contrast, a non-uniform droplet size distribution, with larger droplets along the periphery, were formed from an elongated primary atomization process that was more strongly affected by the fully-developed spray velocity profile. As will be discussed later, there are currently no available measurements that can assess this predicted relationship between the atomization timescale and the resultant downstream droplet size distribution. However, complementary measurements of the characteristic timescale or axial length of the primary atomization region and two-dimensional droplet size distributions could yield valuable insight into the currently missing link between the atomization processes in the near nozzle region and the produced spray structure.

Because the predicted droplet size distributions are seen to strongly differ in be-

havior along the centerline and periphery of the spray, it is desirable to quantify the peripheral droplet size distribution with its own response metric that will enable insight into the behaviors of different primary atomization models over a wide range of operating conditions. It is also desirable to target a quantity that may be feasibly measured to enable model validation of these behaviors. For example, the conventional PDPA measurement technique can provide point-wise droplet sizing data in these regions [61]. The SAMR measurement technique, detailed in Chapter 3, is also applicable within the optically thin regions along the spray periphery. A representative response metric to characterize the periphery of the spray can be identified through evaluation of the peripheral droplet size distribution, as shown in Figure 5.3(b). The peripheral SMD distribution varies greatly in the first 40 mm from the injector nozzle exit. Downstream of 40 mm, the peripheral SMD distribution does not appreciably change with axial distance. This steadiness in the peripheral SMD distribution is seen to coincide with the axial locations, $\tilde{x}$, where the central SMD distribution also reaches a steady value within 10% of SMD_{min}. As a result, characterization of the peripheral droplet distribution is limited to axial locations, $\tilde{x}$. Additionally, across the range of conditions and evaluated spray models, it was determined that the key features of the peripheral droplet size distribution were contained in transverse regions of the spray, $\tilde{y}$, where the local SMD distribution deviates by more than 20% from the centerline SMD. As a result, for the best comparison of spray model predictions with available and emerging measurements along the periphery of the spray, the arithmetic mean of the peripheral SMD distribution, SMD_{periph}, is identified as the characteristic response metric. $\tilde{x}$, $\tilde{y}$, and SMD_{periph} can be mathematically defined with the following equations:

$$\tilde{x} = \{x \,|\, 0.9\, SMD_{min} \leq SMD(x, y = 0) \leq 1.1\, SMD_{min}\} \tag{5.5}$$

$$\tilde{y} = \{y \,|\, SMD(\tilde{x}, \tilde{y}) \geq 1.2\, SMD(\tilde{x}, y = 0)\} \tag{5.6}$$

$$SMD_{periph} = mean\{SMD(\tilde{x}, \tilde{y})\} \tag{5.7}$$

5.3.2 Local Sensitivity Analysis of Central SMD Distributions to Changes in Injection and Ambient Conditions

Using the selected response metrics to characterize the spray structure in the central (SMD_{min}) and peripheral (SMD_{periph}) regions of the spray, it is possible to efficiently evaluate how the predicted spray structure responds to changes in injection and ambient conditions for each spray model. Comparison of SMD_{min} across the entire condition space is shown in Figure 5.4 for the (a) KH, (b) KH-ACT, and (c) KH-Faeth primary atomization models. For each spray model, SMD_{min} at each condition is normalized by the SMD_{min} predicted by the KH model at the Case 16 condition to yield $\overline{SMD}_{min}$. This normalization enables the response of the models to be evaluated relative to each other. Decreases in $\overline{SMD}_{min}$ indicate the formation of relatively smaller droplets along the centerline of the spray, and an enhanced spray breakup process. Comparison of Figures 5.4(a), (b) and (c) reveals that all models exhibit the same general trend that $\overline{SMD}_{min}$ (and therefore SMD_{min}) decreases with decreasing ρ_f/ρ_g, increasing P_{inj}, and decreasing nozzle diameter.

A non-intuitive result is found when comparing the KH and KH-ACT spray models; in particular, the two models predict similar responses of SMD_{min} to changes in ambient and injection conditions, even though the KH-ACT model includes additional physics that represent the effect of nozzle-generated turbulence on the primary atomization process. In fact, for the set of spray model constants employed in this study, as listed in Table 5.1, and over the range of evaluated conditions, the turbulent primary breakup governs the size of droplets predicted by the KH-ACT model

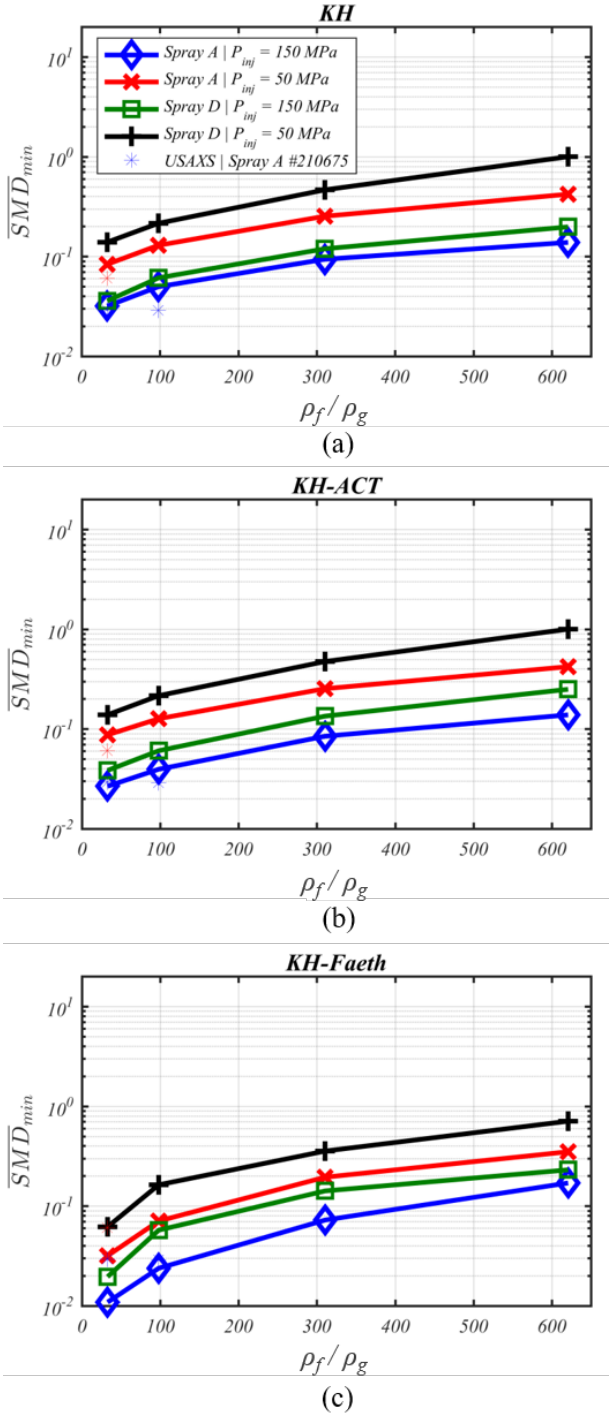

Figure 5.4: *Comparison of $\overline{SMD}_{min}$ as predicted by (a) KH, (b) KH-ACT, and (c) KH-Faeth models over a range of ρ_f/ρ_g, P_{inj}, and nozzle diameters. Decreases in $\overline{SMD}_{min}$ indicate the formation of relatively smaller droplets along the centerline of the spray, and an enhanced droplet breakup process.*

in the near nozzle region. Indeed, as shown in Figure 5.2, the KH-ACT model is seen to produce smaller SMD in the near nozzle region relative to the KH model predictions. These findings are also in agreement with the work from Tatschl and co-workers [141], who found that the turbulent breakup rate is much higher in the near nozzle region than that due to the aerodynamic wave growth. However, the turbulent primary atomization process does not yield smaller SMD_{min} than that produced by the aerodynamic primary atomization model. Instead, the droplet sizes formed from the turbulent breakup process scale with the turbulent integral length scale, L_t, which results in droplets that are larger than Λ_{KH}. These droplets are therefore unstable, undergo subsequent KH secondary breakup, and ultimately result in SMD_{min} which scale with Λ_{KH}, as opposed to L_t. Therefore, the details of primary atomization in the near nozzle region appear to have minimal effect on SMD_{min} in the downstream portion of the spray. This scaling yields good agreement among the KH and KH-ACT model predictions and available USAXS measurements along the spray centerline, as shown in Figure 5.4(a) and (b) for ρ_f/ρ_g less than 100. This agreement suggests that the experimentally measured SMD_{min} scales with Λ_{KH} for ρ_f/ρ_g less than 100, and is ultimately controlled by secondary droplet breakup and may not be sensitive to the details of the primary atomization process. These results are consistent with the findings from Wu and Faeth [18], who found that droplet distributions within the merged aerodynamic primary and secondary breakup regime ($\rho_f/\rho_g < 500$ and $\tau_R/\tau_b > 4$) were controlled by secondary droplet breakup processes, as shown in Figure 1.14.

In general, while the KH-Faeth model SMD_{min} predictions, shown in Figure 5.4(c), exhibit similar trends with respect to changes in injection and ambient conditions, the KH-Faeth model predicts smaller SMD_{min} than either the KH or KH-ACT models for ρ_f/ρ_g less than 100. Indeed as previously shown in Figure 5.2(a), the KH-Faeth primary atomization model produces relatively smaller droplets in the first few millimeters from the nozzle exit. These findings are to be expected based on the

employed scaling from the Faeth correlation, where droplet sizes formed from the primary atomization process were reasoned to exist within the inertial subrange of the turbulence spectrum [18]. This is in contrast to the scaling of larger droplets from the KH-ACT model, which scale with the integral length scale [45, 74]. For ρ_f/ρ_g less than 100, the droplets formed from the primary atomization process are smaller than Λ_{KH}, and are therefore stable to KH instabilities that would promote further droplet breakup. However at ambient conditions where ρ_f/ρ_g is greater than 100, as shown in Figure 5.2(b), the KH-Faeth primary atomization model produces droplets that are larger than Λ_{KH}. As a result, these droplets are unstable to KH instabilities and undergo subsequent droplet breakup. For ρ_f/ρ_g greater than 100, the KH-Faeth predictions for SMD_{min} generally scale with Λ_{KH} and closely match those predicted by the KH and KH-ACT models, as illustrated in Figure 5.2(b) and Figure 5.4.

It is important to note that for the lowest ambient densities considered in this study ($\rho_f/\rho_g = 620$), particularly for the Spray D cases, the stable droplet size and SMD_{min} in the central region of the spray are formed at distances greater than 60 mm from the injector nozzle. One of the important reasons SMD_{min} is a critical response metric is because of its potential relationship to the secondary droplet breakup process. However, the link between droplet breakup and SMD_{min} becomes complicated if the effects of droplet interactions, such as collisions and coalescence, are important. Over the span of 60 mm or more (greater than 300 nozzle diameters for the Spray D injector nozzle), it is possible that droplet interactions could influence the size of droplets measured along the spray centerline. However, as the spray disperses and entrains more ambient gas, the liquid volume fraction, and therefore droplet number density, will decrease with distance from the injector. As the droplet number density decreases, the average distance between droplets will increase, resulting in a decreased probability of droplet interaction [66]. As a result, it is likely that SMD_{min} may still be correlated with the secondary droplet breakup process.

In summary, SMD_{min} is determined by a competition between the primary atomization and subsequent droplet breakup length scales. As expected, the predicted SMD_{min} by the KH model scales with Λ_{KH} across all injection and ambient conditions. Even with the addition of a turbulence-induced primary atomization mechanism to the KH model, the droplet sizes formed from the KH-ACT primary atomization model are larger than Λ_{KH} and are therefore unstable and undergo subsequent KH droplet breakup; as a result, the predicted SMD_{min} by the KH-ACT model is the result of KH droplet breakup and therefore scales with Λ_{KH} across all injection and ambient conditions. In contrast, the scaling of SMD_{min} predicted by the KH-Faeth model exhibits a dependence on ambient condition. For ρ_f/ρ_g less than 100, the turbulence-induced primary atomization process, as modeled with the Faeth correlation (Equation 5.2) [18], produces droplets that are smaller than Λ_{KH}. As a result, these droplets are stable and SMD_{min} scales with the Faeth turbulent length scale correlation, as described in Equation 5.2. For ρ_f/ρ_g greater than 100, the turbulent primary atomization process produces droplets that are larger than Λ_{KH}. As a result, these droplets are unstable to KH instabilities and SMD_{min} ultimately scales with Λ_{KH}.

5.3.3 Local Sensitivity Analysis of Peripheral SMD Distributions to Changes in Injection and Ambient Conditions

Similar analysis of the predicted spray structure in the central region of the spray is extended to characterize the predicted droplet size distribution along the periphery of the spray. Comparison of SMD_{periph} across the entire injection and ambient condition space is shown in Figure 5.5 as predicted by the (a) KH, (b) KH-ACT and (c) KH-Faeth primary atomization models. Similar to $\overline{SMD}_{min}$, SMD_{periph} at each condition is normalized by SMD_{periph} predicted by the KH model at the reference condition at $\rho_f/\rho_g = 620$ and $P_{inj} = 50$ MPa for Spray D with a nozzle diameter of 186 μm, to

yield $\overline{SMD}_{periph}$. This normalization allows for the relative influence of injection and ambient conditions to be evaluated on the peripheral droplet size distribution among the three primary atomization models. For all of the models, with a fixed nozzle diameter and P_{inj}, the predicted $\overline{SMD}_{periph}$ (and therefore SMD_{periph}) increases with increasing ρ_f/ρ_g. Additionally, all models predict an increase in SMD_{periph} when the nozzle diameter is increased, for a fixed P_{inj} and ρ_f/ρ_g.

The SMD_{periph} predicted by the KH-Faeth model exhibits a much smaller sensitivity to changes in nozzle diameter than is predicted by either the KH or KH-ACT model. As previously noted, in the absence of droplet-droplet interactions, droplet size distributions across the width of the spray provide indirect validation of the primary atomization process. The droplets formed from the KH-Faeth primary atomization model scale with turbulent eddies within the inertial subrange. This scaling differs from that employed in the KH-ACT model, where droplets formed form the primary atomization process scale with turbulent eddies within the energy-containing range of the turbulence spectrum, which have a larger dependence on geometric features of the flow, such as nozzle diameter [91].

The difference in sensitivity of SMD_{periph} to changes in nozzle diameter predicted by the three spray models is amplified at ambient conditions where ρ_f/ρ_g is greater than 100. At these conditions, the length and time scales characterizing aerodynamic breakup become insensitive to changes in ρ_f/ρ_g. This insensitivity is exhibited by the relatively constant predictions of SMD_{periph} by the KH and KH-ACT models in Figure 5.5(a) and (b) for ρ_f/ρ_g greater than 100 and for all nozzle diameters and P_{inj} considered. As a result, these higher ρ_f/ρ_g conditions present a prime set of experimental conditions where droplet sizing measurements along the periphery of the spray should be focused. Quantifying the measured response of SMD_{periph} to changes in nozzle diameter and ρ_f/ρ_g at these conditions may help identify modeling inaccuracies of existing spray models. These measurements also show promise of

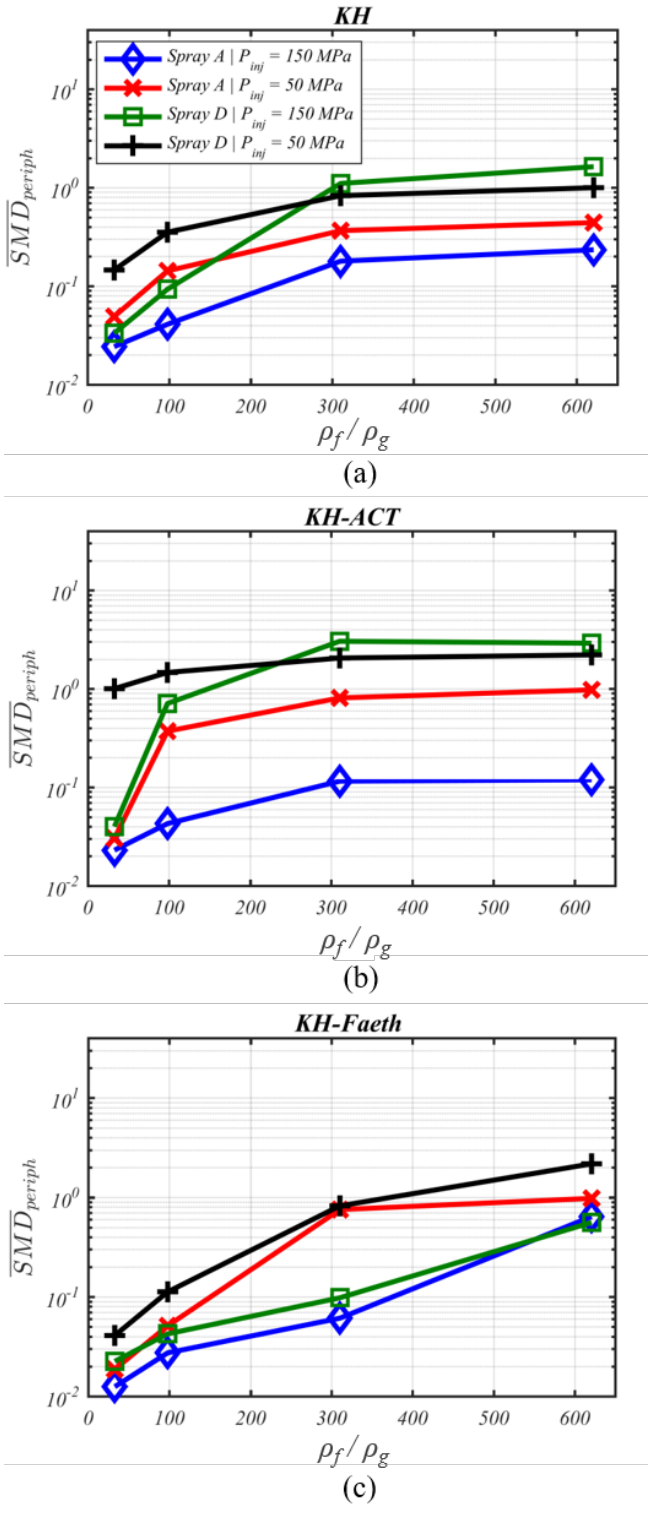

Figure 5.5: *Comparison of $\overline{SMD}_{periph}$ as predicted by (a) KH, (b) KH-ACT, and (c) KH-Faeth models over a range of ρ_f/ρ_g, P_{inj}, and nozzle diameters.*

shedding light on an appropriate primary atomization mechanism that can unify the spray breakup modeling approach across the entire range of ambient conditions. However, the link between primary atomization and SMD_{periph} becomes complicated if the effects of droplet interactions, such as collisions and coalescence, are important.

Differences also exist between the response of the predicted SMD_{periph} to changes in P_{inj} for a fixed nozzle diameter and ρ_f/ρ_g. For example, for the Spray A nozzle conditions shown in Figure 5.5, all of the models predict an increase in SMD_{periph} when P_{inj} is decreased from 150 MPa (blue line) to 50 MPa (red line) across all ρ_f/ρ_g conditions. This relationship between SMD and P_{inj} is consistent with the predicted trends for SMD_{min} for all models, as shown in Figure 5.4. For the Spray D nozzle, the KH-Faeth model predicts a similar trend for SMD_{periph} across all ρ_f/ρ_g conditions: when P_{inj} is decreased from 150 MPa (green line) to 50 MPa (black line), SMD_{periph} increases. This trend is also exhibited for the KH and KH-ACT spray predictions at ρ_f/ρ_g conditions less than 100 for the Spray D nozzle. However for ρ_f/ρ_g greater than 100, the trend is reversed: decreases in P_{inj} result in smaller predicted SMD_{periph} by the KH and KH-ACT models.

Although this trend contradicts the response of SMD_{min} to changes in P_{inj}, the relationship can be better understood by evaluating sample two-dimensional SMD distributions for the Spray D nozzle as predicted by the KH-ACT model. The KH-ACT predicted spray structure is shown in Figure 5.6, at a condition of $\rho_f/\rho_g = 310$ and (a) $P_{inj} = 50$ MPa and (b) $P_{inj} = 150$ MPa. As P_{inj} is increased, the primary atomization timescale remains approximately constant, as illustrated by the similar rates of SMD decrease along the spray centerline in Figure 5.6(a) and (b). Additionally, the atomization process is noted to be relatively longer than that observed at lower conditions (Figure 5.3(a)). More specifically, the computational parcels have only decreased in size by less than 5% within the first 3 mm from the nozzle. As a result, computational parcels across the width of the spray are expected to un-

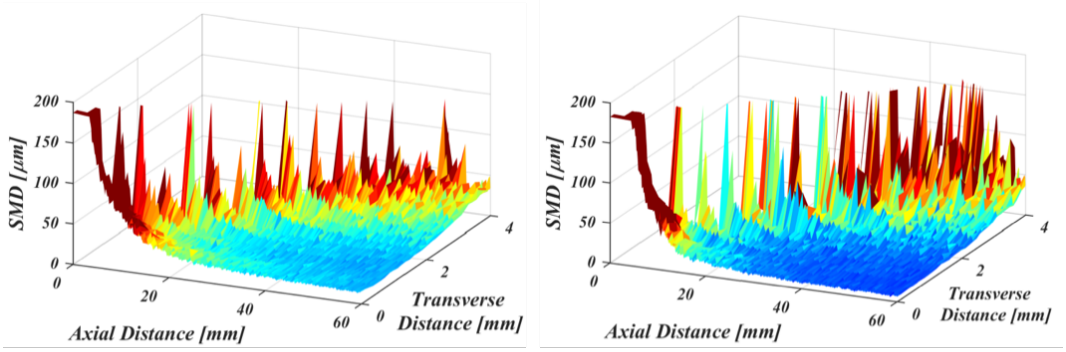

(a) (b)

Figure 5.6: *Sample 2-D time-averaged SMD map as predicted by the KH-ACT model for the Spray D nozzle at ambient and injection conditions of (a)* $\rho_f/\rho_g = 310$*,* $P_{inj} = 50$ *MPa and (b)* $\rho_f/\rho_g = 310$*,* $P_{inj} = 150$ *MPa. Only half of the spray is shown in order to clearly illustrate the difference in predicted SMD between the central and peripheral regions of the spray.*

dergo different local flow conditions as they continue to decrease in size due to the development of the spray velocity profile, which produces a non-uniform droplet size distribution downstream. This predicted non-uniform spray structure is consistent with the sample droplet size distribution predicted by the KH model for the Spray A nozzle, as previously shown in Figure 5.3(b) for the Case 7 condition ($\rho_f/\rho_g = 620$, $P_{inj} = 150$ MPa).

For the lower injection pressure case in Figure 5.6(a), a stable droplet size is achieved along the central region of the spray between 40 to 60 mm from the nozzle exit. The corresponding peripheral region shows a wide range of SMD, ranging from 25 μm to 150 μm. As P_{inj} is increased, the transit time of the computational parcel decreases and high momentum computational parcels from the edge of the primary atomization region convect downstream at a faster rate than at the lower P_{inj} condition. As a result, a higher probability of SMD greater than 100 μm can be seen at the higher P_{inj} condition along the periphery of the spray in Figure 5.6(b). This effect is amplified by the low relative velocities of droplets along the periphery of the spray, which does not promote KH secondary breakup. As a result, the timescale for secondary droplet breakup approaches infinity and causes a nearly "frozen" SMD

distribution along the periphery. This trend is also observed in the SMD predictions by the KH model. The presence of larger SMD_{periph} with increases in P_{inj} is not observed in the model predictions at lower ρ_f/ρ_g conditions due to the combined effect of faster primary atomization, and increased inertia of the ambient gas acting on the droplets, which serves to decrease the momentum of droplets along the periphery. Additionally, this trend is not observed for Spray A conditions due to the combined effects of a faster primary atomization process and production of smaller droplets, which have relatively lower momentum than those formed from the Spray D injector nozzle.

5.4 Summary

An informed pathway towards predictive spray models is only possible through detailed characterization of the predicted spray structure from existing spray models, in concert with comparison and validation against quantitative droplet sizing measurements throughout the spray. In this computational study, the influence of the primary atomization model on the predicted spray structure was explored through evaluation of two existing spray models in the literature, namely the KH and KH-ACT models, and a newly developed KH-Faeth model. A wide range of injection and ambient conditions for two different ECN nozzles (Spray A and Spray D) were studied in this work. Comparison between predicted spray structure among the three primary atomization models and against available spray measurements revealed:

1. For all three primary atomization models, the predicted droplet sizes in the central and peripheral regions of the spray exhibited different sensitivities and responses to changes in injection and ambient conditions considered in this study. As a result, unique response metrics were identified for the central and peripheral droplet size distributions to comprehensively characterize the influence of

the spray primary atomization model on the predicted spray structure. The minimum SMD (SMD_{min}) along the spray centerline was used to characterize droplet sizes in the central region of the spray, and provided a direct comparison with available USAXS measurements. The mean SMD along the spray periphery (SMD_{periph}) was used to characterize droplet sizes in the peripheral region of the spray, and will enable a direct comparison with two-dimensional maps of the SMD distribution when peripheral droplet sizing measurements become available.

2. Comparison of predicted SMD_{min} among the three models revealed that the droplet sizes along the central region of the spray are determined through a competition between the size of droplets formed from the primary atomization and secondary droplet breakup processes. For ρ_f/ρ_g greater than 100, secondary droplet breakup, as modeled with the KH instability mechanism, was observed to control the size of droplets in the central region of the spray. For ρ_f/ρ_g less than 100, the KH and KH-ACT models both predict SMD_{min} that scale with the KH length scale. However, the KH-Faeth model predicts the formation of droplets that are smaller than the droplet breakup length scale for ρ_f/ρ_g less than 100. As a result, droplets in the central region of the spray remain stable in size and instead scale with the Faeth primary atomization length scale. However, comparison with available USAXS measurements for ρ_f/ρ_g conditions less than 100 revealed that the Faeth turbulent primary atomization scaling predicted a more intense breakup process than indicated in the measurements. Potential calibration of the KH-Faeth model will be explored in the future when additional droplet size measurements are available in the central and peripheral regions of the spray.

3. Comparison of predicted SMD_{periph} among the three models revealed that the

droplet sizes along the spray periphery are highly dependent upon the details of the primary atomization process, particularly the atomization timescale. A fast primary atomization process results in SMD_{periph} that largely scale with SMD_{min}. For elongated primary atomization processes, SMD_{periph} generally scale with the characteristic atomization length scale. This observed relationship presents motivation for utilizing droplet sizing measurements along the periphery of the spray as an indirect characterization of the unobservable primary atomization process.

This computational study has demonstrated different scalings and sensitivities of droplet sizes in the central and peripheral regions of the spray to changes in injection and ambient conditions. Results from future joint computational and experimental studies show promise of yielding insight into the appropriate physics that should be included to model diesel-like sprays over a wide range of operating conditions. In Chapter 6, centerline SMD profiles measured by Argonne researchers using the US-AXS technique are evaluated. Comparison with modeling results from Section 5.3.2 are utilized to inform recommendations for an improved hybrid spray breakup model that can represent the contributions of aerodynamics and turbulence on the primary atomization process in diesel sprays.

CHAPTER 6

RECOMMENDATIONS FOR A HYBRID SPRAY BREAKUP MODEL FORMULATION

As discussed in Chapter 4, under conventional diesel operating conditions ($\rho_f/\rho_g < 100$), an aerodynamic wave growth model, namely the KH spray breakup model, was shown to adequately represent the measurable spray quantities for the non-cavitating Spray A injector. However, work by Faeth and co-workers has shown that the influence of aerodynamic forces on the spray breakup process is likely suppressed when ρ_f/ρ_g is increased above 500, and that the droplet formation process is entirely controlled by turbulence-induced breakup [18, 47]. For n-dodecane at room temperature, this proposed transition would occur for ambient densities less than 2.0 kg/m^3. This chapter details controlled experimental studies that were conducted under $\rho_f/\rho_g > 300$ conditions to evaluate the applicability of the findings from Wu and Faeth to diesel sprays. Under such conditions, spray modeling results from Section 5.3.2 suggest that regardless of the primary atomization model employed, the centerline SMD distributions is predicted to be controlled by secondary droplet breakup in downstream portions of the spray. As a result, comparison of model predictions with USAXS data would allow for further evaluation of the Wu and Faeth regime map, and its relevance to diesel sprays, through assessessment of the role of secondary droplet breakup under conditions suggested to be governed by non-aerodynamic primary breakup [18,49]. These findings can then be used to guide recommendations for how turbulence-induced primary breakup should be represented in a hybrid breakup model for diesel sprays. This work has been detailed in publications by the author, and are shown here for posterity [87, 88].

6.1 Experimental Characterization of Diesel Injector and Spray Parameters

Detailed experimental characterization of the injector geometry and spray structure in the near-nozzle region is critical for better understanding the link between internal nozzle flow phenomena and spray atomization. Controlled experiments under non-vaporizing atmospheric-like conditions show promise of isolating the role of nozzle-generated turbulence on the primary spray breakup process. Case $9-10$ and $13-16$ conditions in Table 2.3 using the ECN Spray D injector were selected to study the response of the spray structure of non-vaporizing diesel sprays to changes in injection and ambient conditions. The ECN Spray D injector nozzle #209133 is a well characterized injector, which features a single-orifice diesel injector with a nominal diameter of 180 μm [113]. Discussion of the experimental data sets can be found below. It should be noted that all experimental measurements were evaluated during the steady portion of the injection event, when the injector needle is fully lifted and the injection velocity has reached a nominally constant value.

6.1.1 X-Ray Tomography of ECN Spray D

Injector nozzle tomography measurements were performed by Argonne researchers at the 7-BM beamline at the APS [115]. Details regarding the x-ray tomography measurement technique can be found in Section 2.2.2.1. Key features from the computed tomography are compared to nominal manufacturer's specifications, as shown in Table 6.1. Although the actual nozzle outlet diameter is reasonably close to the nominal specification, the manufacturing process resulted in a more cylindrical nozzle orifice profile than specified, as indicated by the smaller measured K-factor,

$$K = \frac{d_{inlet} - d_{outlet}}{10} \tag{6.1}$$

Table 6.1: *Comparison of ECN Spray D #209133 injector nozzle geometry dimensions, as measured by x-ray tomography conducted at the Argonne APS [94], with manufacturer's specifications [113].*

	Nozzle Outlet Diameter [μm]	K-Factor	Mean Inlet Radius of Curvature [μm]
Nominal Specifications	180	1.5	–
ECN Spray D #209133	186 ± 2	0.8	207 ± 4

where the nozzle orifice inlet and outlet diameters, d_{inlet} and d_{outlet}, respectively, are defined in microns.

Evaluation of the reconstructed internal nozzle geometry of the Spray D #209133 injector, as shown in Figure 2.4(a), reveals unique features in the nozzle orifice. In particular, a groove can be seen that runs along the length of the nozzle orifice, and results in an eccentric nozzle outlet profile, as shown in Figure 2.4(b). If conditions exist where the resultant spray is sensitive to asymmetries in the internal nozzle geometry, spray asymmetries could influence the ability to characterize the spray structure using projected line-of-sight measurements from a single viewing angle. Evaluation of measurements capable of characterizing the underlying spray structure, such as diffused-back illumination (DBI), can help identify conditions where the spray may be sensitive to these features in the internal nozzle geometry, and where the approximation of symmetry is valid for characterizing the spray structure.

6.1.2 Diffused-Back Illumination Imaging

DBI imaging was conducted by a colleague using the high-pressure spray facility at the Spray Physics and Engine Research Laboratory at Georgia Tech. The details of the experimental technique are provided in Section 2.2.4.2. Using the DBI measurements, the implicit assumption of symmetry when utilizing a single viewing angle of the spray

to characterize the spray structure is examined, and potential limitations of this approximation are identified. Figures 2.12(a)-(b) show examples of time-averaged 2D extinction maps produced for the Case 10 and 16 conditions (P_{inj} of 50 MPa and P_{amb} conditions of 2 MPa and 0.1 MPa), respectively, with the injector nozzle centered at 0 mm in the axial and transverse coordinates. In general, high levels of optical thickness can be seen along the spray centerline, which has been shown to correlate with high droplet number densities [84]. With increasing radial distance from the spray centerline, the spray becomes more diffuse and the optical thickness decreases. Evaluation of the 2D extinction maps reveals that the spray appears more asymmetric at the lower P_{amb} condition shown in Figure 2.12(b) in comparison to the higher P_{amb} condition shown in Figure 2.12(a). This trend is likely due to the dependence of entrainment and local mixing on ambient density conditions, which would diffuse the appearance of asymmetric features.

When evaluating sprays injected into nominally constant pressure environments, as is the case for the ambient conditions in the high-pressure spray facility described in Section 2.2.3, asymmetries observed in time-averaged data indicate a consistent asymmetric boundary condition. Asymmetries have been observed by other researchers to be caused by geometric nozzle effects and cavitation [82, 142, 143]. However, measured discharge coefficients for the Spray D injector are greater than 0.8 under these conditions, as noted in Section 2.2.5 and Table 2.2, indicating that cavitation is not strongly influencing the nozzle exit conditions [82,142]. As a result, these results suggest that asymmetries and surface imperfections within the internal nozzle geometry may have a more noticeable influence on the global spray distribution as the ambient environment approaches atmospheric conditions.

To quantitatively characterize the influence of injection and ambient conditions on the asymmetry of the spray, as observed in the DBI measurements in Figure 2.12, transverse distributions of the optical thickness, $\tau(y)$, are evaluated. As shown in

Figure 6.1(a), $\tau(y)$ distributions at a distance of 12 mm from the nozzle exit are compared for two back pressure conditions (0.1 MPa and 2 MPa), and two injection pressures (50 MPa and 150 MPa). Consistent with the observations from Figure 2.12, the transverse optical thickness distributions are more asymmetric for P_{amb} conditions less than 0.2 MPa. To quantify the degree of asymmetry at a given location in the spray, $\tau(y)$ is first decomposed into its symmetric and asymmetric components, $\tau^+(y)$ and $\tau^-(y)$, respectively, as mathematically defined below:

$$\tau(y) = \tau^+(y) + \tau^-(y) \tag{6.2}$$

$$\tau^+(y) = \frac{1}{2}\{\tau(y) + \tau(-y)\} \tag{6.3}$$

$$\tau^-(y) = \frac{1}{2}\{\tau(y) - \tau(-y)\} \tag{6.4}$$

where y is the transverse position at a fixed axial location, x, in the spray. The l^2–norm, $||\tau^+||_2$ and $||\tau^-||_2$, can then be used to quantify the magnitude of $\tau^+(y)$ and $\tau^-(y)$. Employing these definitions, the symmetry of τ, $S(\tau)$, can be quantified as follows,

$$S(\tau) = \frac{||\tau^+||_2}{||\tau^+||_2 + ||\tau^-||_2} \tag{6.5}$$

where $S = 1$ indicates a symmetric distribution and $S = 0$ indicates a perfectly asymmetric distribution.

The degree of asymmetry observed in the DBI measurements can now be quantified throughout the spray for a given condition by evaluating the axial distribution of $S(\tau(y))$, as shown in Figure 6.1(b). For P_{amb} condition of 2 MPa, some variation in S is observed throughout the spray. However, the spray structure, as indicated by the

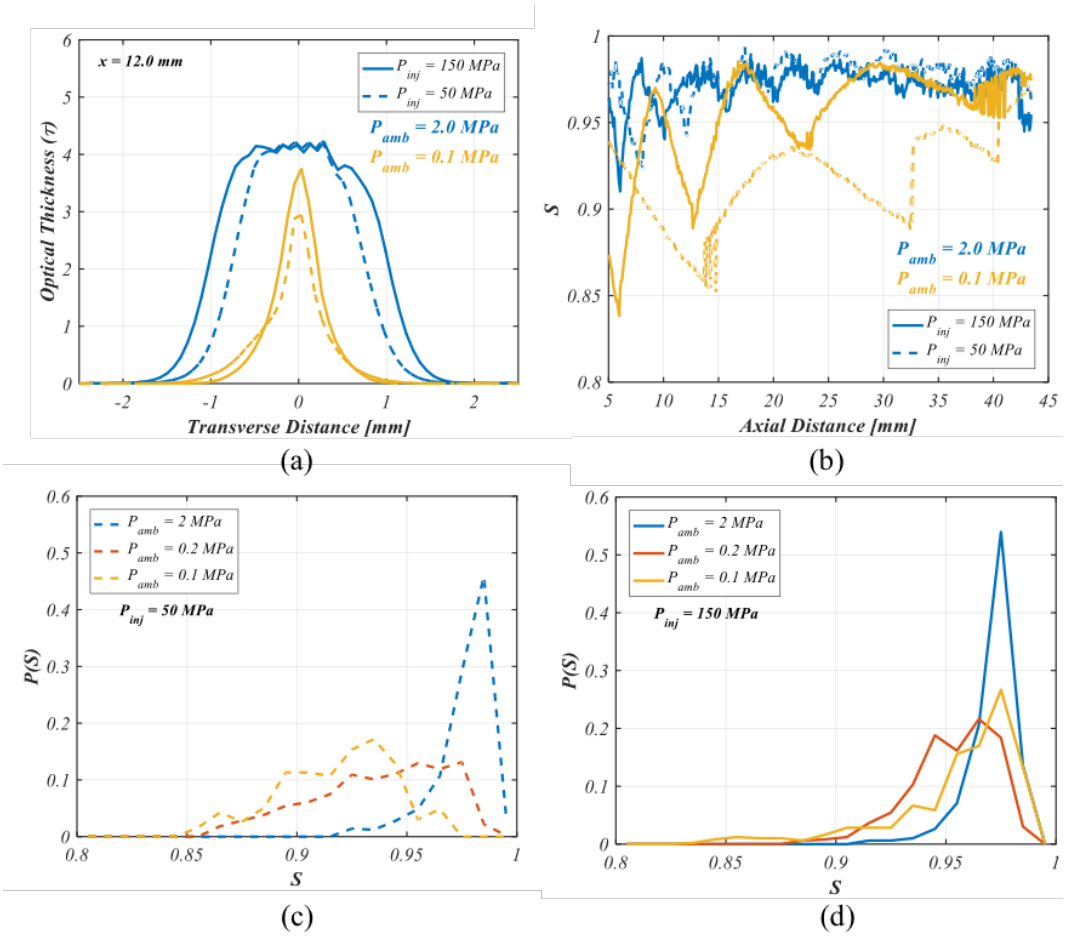

Figure 6.1: *Example transverse distributions of the optical thickness from DBI measurements at a distance of 12 mm from the nozzle exit are shown in (a). The symmetry factor, S, is quantified for each axial slice in the spray and plotted in (b). Probability distributions of S, $P(S)$, throughout the spray are shown for P_{inj} of (c) 50 MPa and (d) 150 MPa.*

optical thickness, is generally symmetric ($S \approx 0.98$). These features are more clearly visualized in the histograms in Figure 6.1(c)-(d) for the P_{amb} condition of 2 MPa and P_{inj} conditions of 50 and 150 MPa. The peak probability of S, $P(S)$, occurs at approximately $S = 0.98$. The probability distributions are also seen to be quite narrow, indicating that the approximation of spray symmetry is valid throughout the spray.

However, for P_{amb} conditions of 0.1 MPa and 0.2 MPa, the distributions appear more asymmetric with greater variability throughout the spray, as shown in Figure 6.1(b)-(d). As shown in Figure 6.1(c), for the back pressure condition of 0.1 MPa and injection pressure of 50 MPa, the most probable S throughout the optical thick-

ness distribution ($S \approx 0.92$) is less than the highest P_{amb} condition. Additionally, the spread of $P(S)$ is observed to be much wider, indicating a more variable degree of asymmetry throughout the spray. At the P_{inj} condition of 150 MPa as shown in Figure 6.1(d), the most probable S for an ambient condition of 0.1 MPa is similar to that observed for the higher P_{amb} condition ($S \approx 0.98$). However, the variability of S throughout the spray is observed to be much higher.

These results indicate that as the back pressure is decreased and approaches atmospheric conditions (0.1 MPa), the assumption of spray symmetry may not be appropriate at many locations throughout the spray. As previously noted, this asymmetry may be due to geometrically asymmetric features within the nozzle, as shown in Figure 2.4. These results suggest potential consequences on the line-of-sight measurements and the resultant SMD. A single viewing angle may not be able to adequately characterize the mean projected quantities and average SMD along the spray centerline. Therefore, the mean SMD may have a larger degree of uncertainty due to these potential uncharacterized effects. As a result, the SMD quantities and their experimentally observed responses to changes in injection and ambient conditions should be interpreted with these factors in mind.

6.1.3 Ultra Small Angle X-Ray Scattering Centerline SMD Measurements

USAXS measurements of SMD along the spray centerline for Spray D #209133 are shown in Figure 6.2, along with curves fitted to the data to illustrate the general trends in droplet size evolution. In general, the measured SMD decreases with increasing axial distance from the nozzle exit, indicating continual breakup of the spray and droplets. The SMD along the spray centerline is also seen to increase with decreasing P_{amb} and P_{inj}. However, the experimental measurements suggest a transition in droplet formation behavior as ρ_f/ρ_g increases beyond 100, which corresponds to P_{amb} less than or equal to 0.2 MPa. For ρ_f/ρ_g greater than 500, Faeth et al. have shown

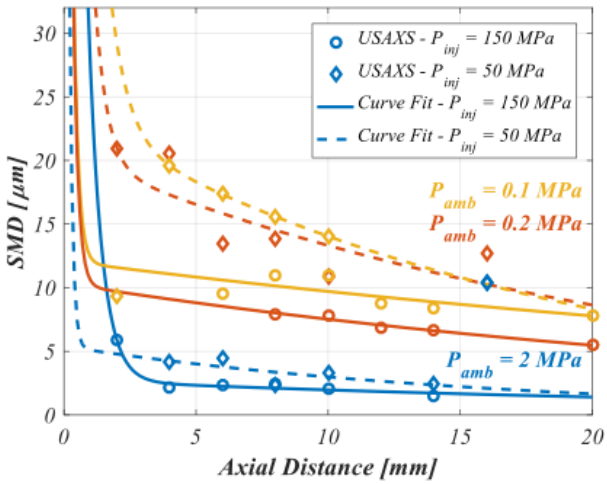

Figure 6.2: *SMD measurements from x-ray measurements conducted at the APS are shown for a range of ambient and injection conditions along the spray centerline. A two-term exponential function is fit to the data (solid and dashed lines).*

that aerodynamic forces do not exert a significant influence on the droplet formation process [18]. The similarity in SMD distributions from the USAXS measurements for P_{inj} of 50 MPa and P_{amb} of 0.1 and 0.2 MPa conditions suggests that changing the aerodynamic inertia by a factor of two does not appreciably change the droplet formation process. However, for P_{inj} of 150 MPa, a larger change in SMD is observed when P_{amb} is increased from 0.1 to 0.2 MPa.

In order to extract more detailed information about the local sensitivity of the SMD to changes in injection and ambient conditions, the axial distribution of SMD is fit to a two-term exponential function for each condition. The curve fit is of the form

$$f(x) = Ae^{Bx} + Ce^{Dx} \tag{6.6}$$

where A, B, C, and D are unique fitting parameters for each condition. An additional point of 186 μm at the nozzle exit ($x = 0$) was added to each data set to capture the rapid decrease in SMD from its initial value of the nozzle outlet diameter. The two-term exponential function captures the data well, with an R^2-value greater than

0.99 for all conditions.

Using these curve fits, the local sensitivity of SMD to changes in injection and ambient conditions can be quantified. The local sensitivities to changes in P_{inj}, $S_{P_{inj}}$, and P_{amb}, $S_{P_{amb}}$, are defined as follows:

$$S_{P_{inj}} = \frac{SMD(P_{inj} = 150\ MPa, P_{amb}, x = x_i)}{SMD(P_{inj} = 50\ MPa, P_{amb}, x = x_i)} \tag{6.7}$$

$$S_{P_{amb}} = \frac{SMD(P_{inj}, P_{amb} = 0.2\ MPa, x = x_i)}{SMD(P_{inj}, P_{amb} = 0.1\ MPa, x = x_i)} \tag{6.8}$$

$S_{P_{inj}}$ and $S_{P_{amb}}$ characterize the relative decrease in SMD as P_{inj} or P_{amb} is increased at a particular axial distance, x_i, from the nozzle exit. S_i equal to unity indicates that the centerline SMD is relatively insensitive to changes in parameter i, assuming all other parameters are held constant. Similarly, S_i approaching zero indicates that the centerline SMD is highly sensitive to changes in parameter i.

The local sensitivities of the measured centerline SMD to changes in P_{inj} and P_{amb} can now be used to better understand the appropriate scaling for the droplet formation process. In particular, an insensitivity to changes in ρ_g, as indicated by $S_{P_{amb}} \approx 1$, would suggest that aerodynamic inertial forces have minimal influence on the resultant SMD and that the droplet formation process is likely controlled by nozzle-generated turbulence. The results of the computed $S_{P_{inj}}$ and $S_{P_{amb}}$ are shown in Figure 6.3 for $x_i = 10$ mm. Indeed, these results confirm previous qualitative observations. At a fixed P_{inj} of 50 MPa, the SMD is not strongly influenced by the change in P_{amb} from 0.1 to 0.2 MPa, as indicated by the high $S_{P_{amb}}$ value of 0.95. However, $S_{P_{amb}}$ appears to have a dependence on P_{inj}, as a higher sensitivity to P_{amb} is indicated for $P_{inj} = 150$ MPa. The measured centerline SMD is also observed to respond to changes in P_{inj}, as evidenced by the $S_{P_{inj}}$ values of 0.58 and 0.68. It should be noted that the reported sensitivities are relatively constant regardless of

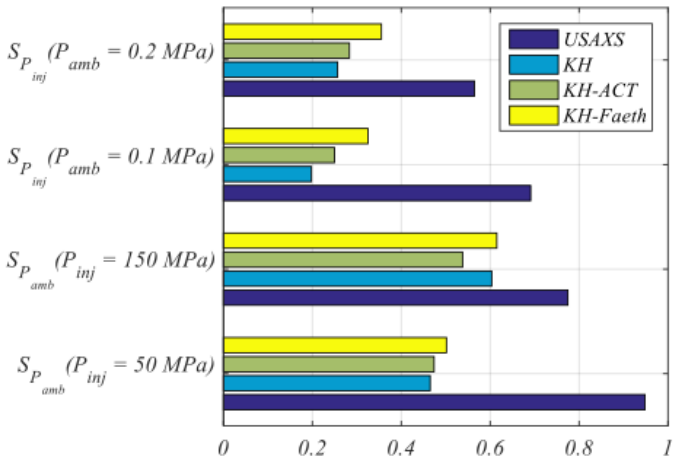

Figure 6.3: *Local sensitivities of SMD to changes in P_{inj} and P_{amb} for ρ_f/ρ_g conditions greater than 300, as indicated by the x-ray measurements and evaluated spray breakup models.*

the x_i selected within the range of the experimental measurement locations.

These results suggest that the critical ρ_f/ρ_g condition defining the transition between non-aerodynamic and aerodynamic primary breakup regimes may occur at a lower ρ_f/ρ_g threshold for diesel sprays than was observed for the idealized nozzles in the studies of Wu and Faeth [18, 47, 49]. Wu and Faeth concluded that aerodynamics had a minimal influence on the resultant size of primary droplets for conditions where $\rho_f/\rho_g > 500$ [18]. However, as noted in Section 1.2.1.2, the $\rho_f/\rho_g \sim 500$ condition defining the non-aerodynamic primary breakup regime boundary was acknowledged by Wu and Faeth to have some uncertainty, and that more experimental work was needed to better define the critical ρ_f/ρ_g condition [18]. The USAXS measurements indicate an insensitivity to changes in ρ_g, and therefore aerodynamic inertial forces, for $\rho_g \leq 2.4$ kg/m^3 ($\rho_f/\rho_g > 300$). However, uncertainty in the critical ρ_f/ρ_g defining this transition was identified based on the dependence of $S_{P_{amb}}$ on P_{inj}. Therefore, the USAXS measurements suggest that the transition between aerodynamic and non-aerodynamic primary breakup may occur between $\rho_f/\rho_g \approx 300-500$ for diesel sprays. However, additional USAXS measurements near this transition would be needed to

more accurately define the critical ρ_f/ρ_g condition. For now, the USAXS measurements conducted under $\rho_f/\rho_g > 300$ conditions are directly compared with proposed scalings within the turbulence spectrum to evaluate potential length scales characterizing the droplet formation process.

6.2 Theoretical Scaling

As previously mentioned, comparison of measured sensitivities from the USAXS measurements with theoretical turbulent scalings can provide clearer insight into the mechanisms driving the turbulent breakup process. For example, the majority of spray models that consider the influence of nozzle-generated turbulence on the spray breakup process assume that the size of primary droplets scales with the largest eddies in the turbulence spectrum, such as the Huh-Gosman and KH-ACT models described in Section 1.2.3 [42–44]. The resultant droplet size scales with the dimension of the flow, and is independent of the Reynolds number and ambient environment properties [91]. This can be demonstrated by evaluating the dependence of the turbulent integral length scale, L_t, on injection and ambient parameters. L_t can be defined using Equation 1.13. Estimations of the turbulent kinetic energy and dissipation rates at the nozzle exit, K_0 and ϵ_0, respectively, can help determine the functional depencies of L_t. Equations 1.22 and 1.23 can then be inserted into the integral scaling as defined in Equation 1.13 to yield a relationship between L_t and the injection and nozzle parameters:

$$L_t \propto \frac{d_j}{(L/d_j)^{0.5}}[\frac{1}{c_d^2} - K_c - (1-s^2)]^{0.5} \tag{6.9}$$

Equation 6.9 provides some interesting information regarding the physical dependencies of the size of eddies within the energy-containing range. If cavitation does not influence the flow conditions at the nozzle exit, c_d will remain nominally constant

across all P_{inj} and P_{amb} conditions [81, 82]. Therefore, L_t is independent of U_{inj} or ρ_g, and is only a function of geometric features of the nozzle, such as the L, d_j, and s of the nozzle, as well as the inlet nozzle radius of curvature. Other researchers have noted that for a fixed flow configuration, increases in U_{inj} (Re_{fd}) do not largely affect integral scales, but do increase the available kinetic energy to distort the liquid-gas interface [49, 144, 145].

As a result, the size of droplets formed from the largest eddies within the energy-containing range would be insensitive to changes in P_{inj} and P_{amb}, which would yield $S_{P_{inj}}$ and $S_{P_{amb}}$ equal to 1.0. This theoretical scaling suggests larger insensitivities with respect to changes in the injection and ambient conditions than indicated by the USAXS measurements in Figure 6.3. Therefore, the centerline distributions of SMD are not likely formed due to turbulent eddies within the energy-containing range. As a result, any turbulent breakup model that assumes that the resultant droplets are proportional in size to the integral length scale, such as the Huh-Gosman or KH-ACT spray models [42–44], is not likely able to predict the experimentally observed trends for diesel sprays, particularly for injection into ambient environments deviating from conventional diesel operating conditions ($\rho_f/\rho_g > 100$).

The experimental measurements conducted by Wu and Faeth suggest that droplet-forming eddies do not exist within the energy-containing range of the turbulence spectrum [18, 49]. For injection into conditions where $\rho_f/\rho_g > 500$, the size of primary droplets were observed to decrease in size as U_{inj} was increased, although the large scale disturbances on the jet surface were observed to be similar in size for the range of evaluated injection conditions [49]. Based on their analysis of the measured liquid surface ligament and droplet properties at the onset of turbulent breakup from holographic imaging, Wu and Faeth developed an empirical correlation to relate the size of droplet-forming eddies, L_{Faeth}, to nozzle exit turbulence properties, as defined in Equation 5.2 [18]. By estimating U_{inj} using the Bernoulli equation, a relationship

among L_{Faeth}, P_{inj} and P_{amb} can be approximated with the following relation:

$$L_{Faeth} \propto We_{f\Lambda}^{-1/3} \propto U_{inj}^{-2/3} \propto (P_{inj} - P_{amb})^{-1/3}. \tag{6.10}$$

Using the relation in Equation 6.10, $S_{P_{inj}}$ and $S_{P_{amb}}$ can be calculated to characterize the response of the Wu and Faeth correlation for non-aerodynamic primary breakup to changes in injection and ambient conditions. For a fixed P_{inj} of 50 MPa or 150 MPa, $S_{P_{amb}}$ is approximately equal to 1.0, suggesting a slightly larger insensitivity of the centerline SMD to changes in P_{amb} than is indicated by the measurements in Figure 6.3. However, a three-fold increase in P_{inj} at a fixed P_{amb} of 0.1 MPa or 0.2 MPa results in $S_{P_{inj}}$ of approximately 0.69. Comparison with $S_{P_{inj}}$ of the USAXS measurements, as shown in Figure 6.3, reveals improved agreement between the measured and predicted sensitivities. Although the estimated $S_{P_{inj}}$ and S_{Pamb} show some small discrepancies with the experimentally observed sensitivities, it is important to consider potential uncertainty in the measured SMD sensitivity. In particular, as previously noted, spray asymmetries exhibited at low P_{amb} conditions may influence the ability to characterize the mean projected quantities and average SMD along the spray centerline from a single viewing angle. Discrepancies in the predicted and measured sensitivities may be due to the uncharacterized influence of asymmetries in the spray distribution on the centerline SMD. It is therefore possible for a properly calibrated L_{Faeth} correlation, as defined in Equation 5.2, that neglects the effects of secondary droplet breakup, to well characterize the experimentally observed sensitivities of SMD to changes in injection and ambient conditions for $\rho_f/\rho_g > 300$.

Although Wu and Faeth's phenomenological framework for characterizing turbulent primary atomization was developed from a database of sprays issued from idealized nozzles, with long L/d_j to ensure fully-developed turbulent flow at the nozzle exit, comparisons between the empirical correlations from Wu and Faeth and the diesel SMD measurements in Figure 6.2 suggest that the geometric differences with

practical diesel injector hardware do not strongly influence the resultant spray atomization process. These results are in agreement with experimental findings from Wu and co-workers, where the condition at the onset of turbulent breakup and the size of primary and secondary droplets were found to be relatively independent of L/d_j for ρ_f/ρ_g conditions greater than 100 [50]. As a result, the empirical correlations from Wu and Faeth may serve as a foundation for representing turbulent primary atomization in diesel spray breakup models.

Spray modeling predictions can help provide further insight into the governing physics and likely breakup regimes characterizing the various measurement conditions. More specifically, for $\rho_f/\rho_g < 500$ conditions within the merged aerodynamic primary breakup regime, Wu and Faeth noted that the measured droplet sizes were governed by droplet breakup processes due to the relatively short timescales characterizing secondary breakup [18]. This behavior contrasts the findings within the non-aerodynamic primary breakup regime ($\rho_f/\rho_f > 500$), where droplet breakup was not observed to influence the droplet sizing measurements. USAXS measurements conducted within the non-aerodynamic primary breakup regime should therefore scale directly with the length scales characterizing the primary atomization process and should not be influenced by secondary droplet breakup. The spray model predictions presented in Section 5.3.2 for the ECN Spray D injector under $\rho_f/\rho_g > 300$ conditions can help provide insight into the physics governing the experimentally measured SMD distribution. As previously noted, the droplet size distributions predicted by the KH, KH-ACT and KH-Faeth spray models were all determined to be governed by secondary droplet breakup along the spray centerline. If the experimentally observed sensitivities are shown to be inconsistent with the predicted sensitivities to changes in P_{inj} and P_{amb}, then further justification can be provided that that the experimentally measured SMD are directly related to the primary breakup process, and likely exist within the non-aerodynamic primary breakup regime.

6.3 Comparison of Measured and Predicted Sensitivities

Using the droplet size predictions for the KH, KH-ACT, and KH-Faeth spray models discussed in Chapter 5, the ability of different atomization models to capture the experimentally observed trends can be evaluated. Instead of focusing on the ability of well-calibrated models to quantitatively match the experimental measurements, the sensitivities of measured and predicted SMD are compared for changes in injection and ambient conditions. To allow for direct comparison with the USAXS measurements, the sensitivity of the predicted SMD_{min} along the spray centerline is evaluated for changes in injection and ambient conditions to calculate S_i defined in Equations 6.8 and 6.7. The predicted sensitivities of the three models are shown in Figure 6.3.

Comparison between the predicted and measured sensitivities of the centerline SMD distribution to changes in injection and ambient conditions reveals several discrepancies. Predicted $S_{P_{amb}}$ by each model at a fixed P_{inj} indicates a stronger influence of P_{amb} on the centerline SMD ($S_{P_{amb}} < 0.6$) than is observed experimentally. Additionally, all spray breakup models exhibit larger sensitivities to P_{inj}, and therefore smaller $S_{P_{inj}}$ ($S_{P_{inj}} < 0.4$), than is indicated by the USAXS measurements.

As previously noted in Chapter 5, in the absence of droplet interactions, predicted droplet sizes within the central region of the spray are determined through a competition between the primary atomization and secondary droplet breakup length scales. All evaluated spray models employ an identical KH secondary droplet breakup model. Therefore, droplets that are larger than the wavelength of the fastest growing KH surface wave, Λ_{KH}, are unstable to KH instabilities and subsequently breakup. For $\rho_f/\rho_g > 100$, the KH, KH-ACT, and KH-Faeth primary atomization models produced droplets that were larger than Λ_{KH}, and therefore underwent subsequent droplet breakup. As a result, for low ambient density conditions, the SMD_{min} pre-

dicted by each of the models was strongly influenced by the secondary droplet breakup process, and the predicted sensitivities were observed to scale with the KH mechanism representing the droplet breakup [87,88]. This finding is confirmed by the similar $S_{P_{inj}}$ and $S_{P_{amb}}$ predicted by the KH and hybrid spray breakup models, as shown in Figure 6.3.

Comparison between the predicted and measured sensitivities suggests that the experimentally measured SMD along the spray centerline are not likely controlled by secondary breakup processes under low ambient density conditions ($\rho_f/\rho_g > 300$). Therfore, the experimental measurements conducted under $\rho_f/\rho_g > 300$ conditions may exist within the non-aerodynamic primary breakup regime, where Wu and Faeth have proposed that turbulent eddies generated within the injector directly govern the size of the measured SMD distribution [18, 49].

6.4 Recommendations for an Improved Hybrid Spray Breakup Model Formulation

Findings from the experimental and computational investigations presented in Chapters 4, 5, and 6 are now synthesized to provide recommendations for an improved hybrid spray breakup model that can represent both aerodynamic and turbulent breakup mechanisms in diesel spray primary atomization. As presented in Chapter 4, experimentally measured droplet size distributions under conventional diesel conditions ($\rho_f/\rho_g < 100$) were well predicted when spray breakup was represented with a KH primary and secondary breakup model [17]. However, for conditions outside of conventional diesel conditions ($\rho_f/\rho_g > 300$), the measured droplet size distribution showed good theoretical agreement with empirical correlation developed by Wu and Faeth to describe turbulent primary atomization [18]. Comparison with spray model predictions presented in Chapter 5 led to the conclusion that the measured droplet size

distribution was not likely influenced by secondary droplet breakup. These findings inform recommendations for the hybrid spray breakup model and are organized into two regimes, defined similarly as those proposed from Wu and Faeth [18]: 1) non-aerodynamic primary breakup, where turbulence governs the primary atomization process in isolation, and 2) merged aerodynamic secondary and primary breakup, where aerodynamic and turbulent primary atomization is accompanied by aerodynamic secondary droplet breakup.

6.4.1 Non-Aerodynamic Primary Breakup Regime

Conditions Defining Boundary of Regime: $\rho_f/\rho_g \gtrsim 300$

Primary Breakup: *Turbulent mechanism in isolation determines predicted breakup rate at each time instant for an individual computational parcel*

Droplet Size [18]: $\frac{L_{Faeth}}{\Lambda} = C_{sx}(\frac{x}{\Lambda We_{f\Lambda}^{1/2}})^{2/3}$

Breakup Time [18]: $\tau_{Faeth} = C_\tau\sqrt{\rho_f \frac{L_{Faeth}^3}{\sigma}}$

Secondary Breakup: *Neglected*

For conditions where $\rho_f/\rho_g > 300$, non-cavitating diesel sprays are proposed to undergo non-aerodynamic primary breakup. The size of primary droplets formed from this process are hypothesized to be determined by the characteristic length scale of turbulent eddies with sufficient energy to overcome surface tension energy at the liquid-gas interface. This characteristic turbulent length scale is defined using the empirical correlation developed by Wu and Faeth [18], as previously defined in Equation 5.2. The time required to form a droplet, τ_{Faeth}, scales with the time required for a droplet to form from a ligament of size L_{Faeth}, according to the Rayleigh instability mechanism, as defined in Equation 5.1. Analysis of the SMD measurements along the spray centerline did not indicate a strong influence of secondary droplet breakup; as a result, secondary breakup is not recommended to be included in a spray model under such conditions. The definition for the boundary of the regime,

and the recommended breakup length and time scales, can be assessed in further detail when additional droplet sizing measurement become available near the proposed ρ_f/ρ_g transition.

6.4.2 Merged Aerodynamic Secondary and Primary Breakup Regime

Conditions Defining Boundary of Regime: $\rho_f/\rho_g \lesssim 300$

Primary Breakup: *Either aerodynamic or turbulent mechanism dictates the primary atomization process at each time instant for an individual computational parcel, based on the mechanism with the fastest predicted breakup rate*

Turbulent Primary Breakup [18]:

Droplet Size: $\frac{L_{Faeth}}{\Lambda} = C_{sx}(\frac{x}{\Lambda We_{f\Lambda}^{1/2}})^{2/3}$

Breakup Time: $\tau_{Faeth} = C_\tau\sqrt{\rho_f \frac{L_{Faeth}^3}{\sigma}}$

Aerodynamic Primary Breakup [17]:

Droplet Size: $r_c = B_0\Lambda_{KH}$

Breakup Time: $\tau_{KH} = \frac{3.726B_1a}{\Lambda_{KH}\Omega}$

Secondary Breakup [17]:

Droplet Size: $r_c = B_0\Lambda_{KH}$

Breakup Time: $\tau_{KH} = \frac{3.726B_1a}{\Lambda_{KH}\Omega}$

For conditions where $\rho_f/\rho_g < 300$, the primary breakup process for non-cavitating diesel sprays is proposed to be governed by both aerodynamic and turbulence-induced breakup mechanisms. As formulated in the newly KH-Faeth spray model developed and presented in Chapter 5, similar to the KH-ACT formulation by Som and Aggarwal [45], the competition between aerodynamic and turbulent breakup mechanisms in driving the droplet formation process is hypothesized to be determined by the mechanism with the fastest predicted breakup rate. To allow for continuous spray breakup behavior across the two regimes, the turbulent breakup process should be modeled consistently with the formulation within the non-aerodynamic primary

breakup regime, using the empirical correlations from Wu and Faeth [18] for L_{Faeth} and τ_{Faeth}, as defined above. As discussed in Chapter 4, due to the demonstrated success of a well-calibrated aerodynamic wave growth model in representing the spray structure under conventional diesel conditions, the aerodynamic breakup process is modeled using the KH spray model formulation from Beale and Reitz [17], as described in Section 1.2.3.1, where a primary droplet of size r_c is formed in a breakup timescale of τ_{KH}. As indicated in the modeling results in Chapter 4, the resultant spray structure was largely influenced by secondary breakup processes, and displayed good agreement with available experimental measurements when the droplet breakup process was modeled with the KH instability mechanism. As a result, for conditions where $\rho_f/\rho_g < 300$, it is recommended for spray models to include the effects of secondary droplet breakup as represented by the KH model [17].

CHAPTER 7

CONCLUSIONS

This chapter summarizes the main conclusions and contributions from the work presented in this thesis. Recommendations for future investigations are also provided.

7.1 Thesis Contributions

Injection strategies in advanced engine concepts are resulting in the injection and atomization of fuel under a wide range of operating conditions. However, the physics governing the breakup of an injected liquid fuel jet into droplets under these conditions have not been well studied or experimentally characterized to date. If computational design tools are to be used to guide the use of direct injection strategies for cleaner and more fuel efficient engines, the physics underpinning primary atomization must be better understood to ensure the development of predictive simulations of fuel-air mixing and vaporization within the engine.

The central aim of this thesis was to improve the physical representation of spray breakup physics within today's engine computational fluid dynamics (CFD) packages to enable the exploration of fuel injection strategies for future engine designs. The main conclusions and contributions of this thesis are divided among four sections. The first section details the development of a new droplet sizing measurement technique for characterizing sprays under a broad range of ambient and injection conditions. Using droplet sizing data obtained from the newly developed measurement technique and measurements provided by Argonne National Laboratory from the ultra-small angle x-ray scattering (USAXS) technique, critical assessment of existing aerodynamic spray breakup model formulations are presented in the second section. In the third

section, experimental and computational findings are summarized that enabled the identification of turbulent scalings that could characterize the measured droplet size distributions. The final section provides an outline of the recommendations for an improved hybrid spray breakup model that includes the influence of both nozzle-generated turbulence and aerodynamics on the breakup process in diesel sprays.

7.1.1 New Droplet Sizing Measurement Technique

Direct observation of the primary breakup process in diesel sprays has not been possible due to the current limitations of imaging technology in providing the simultaneous temporal and spatial resolution required to resolve primary droplets produced from high pressure fuel sprays. In the absence of sufficiently resolved images to visualize spray development, droplet sizing spray measurements are needed to characterize the outcomes of the spray breakup process. However, a database of droplet sizing measurements, capable of guiding a comprehensive and critical assessment of existing spray model predictions, has been missing.

To complement newly available droplet sizing data provided by researchers at Argonne, a new measurement technique was developed to characterize the average size of droplets along the periphery of the spray, as detailed in Chapter 3. Using a ratio of path-integrated x-ray and visible extinction signals, the theoretical capability of the scattering absorption measurement ratio (SAMR) technique to quantify the Sauter mean diameter, SMD, of the droplet size distribution within the measurement volume was derived. The SMD was determined by employing theoretical Mie-scatter calculations to determine the number-weighted mean extinction cross section and number-weighted mean droplet volume that yields the theoretical measurement ratio. Optical properties of the spray were related to SMD by exploring a range of assumed droplet size distributions; however, within the range of SMD expected in diesel sprays (greater than 1 μm), the resultant relationship was determined to be

largely insensitive to the details of the assumed droplet size distribution. The relationship between the measurement ratio and the SMD of the droplet size distribution was determined to be theoretically valid when the visible extinction measurement signal was dominated by single and independent scattering events. A recommendation for characterizing such signals was provided using a threshold of 2 for the maximum interpretable optical thickness signal, τ.

The practical application of the derived measurement technique was tested by evaluating the use of joint x-ray radiography and visible laser extinction measurements to quantify the SMD within the spray. X-ray radiography measurements were conducted by researchers at Argonne at the Advanced Photon Source. Visible laser extinction measurements were performed at the Spray Physics and Engine Reseach Laboratory at Georgia Institute of Technology using the experimental set-up detailed in Chapter 2. In regions where errors in the laser extinction signal due to multiple scattering were sufficiently suppressed ($\tau < 2$), the x-ray radiography and visible laser extinction were jointly processed to yield a measured measurement ratio. Using the theoretically determined relationship between the measurement ratio and SMD of the droplet size distribution in the measurement volume, SMD profiles were determined.

SAMR measurements of SMD were cross-validated through comparison with available USAXS data. In general, SAMR measurements indicated larger SMD values but similar radial gradients in SMD along the spray periphery than the USAXS measurements. These discrepancies were deemed to be related to: 1) uncertainties in measurement position within the spray and relative injector orientation between the x-ray radiography and laser extinction measurements, due to the execution of these measurements at two different experimental facilities; and 2) multiple scattering errors in regions where optical thickness is greater than unity, which serve to artificially increase the SMD calculated from the SAMR technique. Future work should focus on reducing these uncertainties and better quantifying multiple scattering errors in

the current measurement system.

Unique features of the spray were identified by evaluating the joint USAXS and SAMR measurements. For example, transverse SMD profiles suggested a bi-modal shape in the transverse SMD distribution, with a local maximum occuring some distance from the spray centerline. SMD distributions along the periphery of the spray measured from USAXS and SAMR measurement techniques indicated a larger sensitivity to changes in injection pressure than was observed from the centerline SMD measurements from USAXS. Evaluation of the USAXS measurements revealed two key features. Firstly, in the near-nozzle region, a rapid decrease in SMD was measured, and is likely related to the initial breakup of the spray into droplets. Second, at the highest injection studied in this work (150 MPa), a stable droplet size was formed in the downstream portion of the spray. Available measurements suggest that the minimum SMD is insensitive to changes in ambient density. These identified features were recommended as targets for model calibration and validation to ensure faithful representation of the spray.

7.1.2 Assessment of Existing Aerodynamic Spray Breakup Model Predictions

To help shed light on experimental trends and features seen in the USAXS and SAMR SMD measurements, a computational study was conducted to investigate the possible spray and droplet phenomena governing the measured spray structure under conventional diesel operating conditions, characterized by low liquid-to-gas density ratios ($\rho_f/\rho_g < 100$) and high injection pressures ($P_{inj} = 50 - 150$ MPa). For the first time, as detailed in Chapter 4, spray model predictions were able to be directly compared with SMD measurements in the near-nozzle and downstream regions of the spray to ascertain the capabilities and shortcomings of models employed in today's engine CFD codes. In particular, the appropriateness of the commonly employed

spray breakup model based on the growth of aerodynamic surface waves due to the Kelvin Helmholtz (KH) instability was evaluated. Additionally, the ability of selected droplet phenomena, namely secondary droplet breakup and droplet collisions represented using the KH-Rayleigh Taylor (KH-RT) and O'Rourke with Post outcomes collision models, respectively, to explain experimentally observed trends in the spray structure was explored.

The KH primary spray breakup model demonstrated success in matching the key spray features identified in the USAXS and SAMR measurements. For the KH spray breakup model, careful calibration of the spray breakup time constant, B_1, resulted in good agreement for the initial rate of droplet size decrease and length of the near-nozzle spray breakup region, while calibration of the primary droplet size constant, B_0, resulted in good agreement for the stable droplet size formed in downstream portions of the spray for ambient densities between $7.6 - 22.8$ kg/m^3 and injection pressures between $50 - 150$ MPa. Comparison between predicted and measured droplet sizes across the width of the spray revealed that the spray structure was best predicted when the primary breakup process is represented with a slower time constant ($B_1 = 60$) and larger KH primary droplet sizes ($B_0 = 1$) than conventionally recommended for diesel spray models.

A range of spray sub-models were employed to evaluate the influence and physical appropriateness of including secondary breakup, collisions, and coalescence in modeling diesel sprays for accurate predictions of spray structure. Although collision models may replicate experimentally observed trends in SMD at a single condition, the inclusion of such models generally resulted in the overprediction of coalescence events and droplet sizes in downstream portions of the spray. Additionally, secondary breakup via the RT instability mechanism was seen to have a marginal effect on the predicted droplet size distribution at high ambient density conditions (22.8 kg/m^3), and may not be an influential mechanism for controlling droplet sizes for diesel sprays

under typical engine-relevant conditions with high ambient densities ($\rho_f/\rho_g < 100$). Instead, it was determined that the KH primary and secondary breakup model governed the predicted spray structure, and could well represent the experimentally observed trends of SMD throughout the spray within the merged aerodynamic regime proposed by Wu and Faeth.

While the predicted SMD distributions resulting from a carefully calibrated KH model matched experimental trends and measurements over the range of evaluated conditions for downstream portions of the spray, the initial rate of droplet size decrease in the near-nozzle region was not well matched at the lower ambient density condition (7.6 kg/m^3). These results suggest that while the KH primary breakup model can successfully predict spray structure in the downstream portions of the spray, aerodynamic-induced breakup cannot completely characterize the primary breakup process for non-cavitating diesel sprays. Particularly for the range of ambient and injection conditions characterizing advanced engine concepts, it was determined that the KH primary breakup mechanism cannot represent the initial spray breakup process in isolation, and other mechanisms, such as turbulence generated inside the nozzle, likely augment and enhance the primary breakup process. Therefore, existing CFD codes employing KH spray breakup in isolation may not be able to yield predictive results for injection into lower ambient density environments away from conventional top-dead center conditions. These results motivated the need for a hybrid spray breakup model formulation that could account for both turbulence and aerodynamics on the spray formation process across a wide range of injection and ambient conditions relevant for advanced engine concepts.

7.1.3 Identification of Appropriate Scalings for Turbulence-Induced Breakup in Diesel Sprays

In order to build a hybrid spray breakup model that can accurately represent the role of turbulence in the primary atomization process, the length and time scales characterizing the turbulence-induced breakup process must be known. Faeth and co-workers were able to develop empirical correlations describing the characteristic droplet size and time scale of the turbulent primary atomization process by identifying conditions where droplet formation is entirely controlled by turbulence-induced breakup ($\rho_f/\rho_g > 500$). However, under diesel-relevant conditions, conditions defining this regime and the corresponding turbulent scales had not been identified. Therefore, comparison between droplet sizing measurements and turbulent primary atomization model predictions are needed to identify the appropriate scalings for representing turbulence-induced breakup in diesel sprays.

In order to identify the strengths and deficiencies of existing spray breakup models, the response of predicted spray structure to changes in injection and ambient conditions from purely aerodynamic (KH) and hybrid turbulent and aerodynamic (KH-ACT) breakup models were evaluated. In order to better understand the influence of the scaling assumed in the turbulent primary breakup model on the predicted spray structure, a new hybrid spray model, called the KH-Faeth model, was developed. Building off of the hybrid spray breakup formulation in the KH-ACT model, the existing turbulent droplet size and breakup time scales were replaced with empirical correlations developed by Wu and Faeth.

Across the wide range of ambient density ($1.2-22.8$ kg/m^3) and injection pressure ($50-150$ MPa) conditions considered for the Engine Combustion Network (ECN) Spray A and Spray D injectors, two distinct behaviors were identified for the predicted centerline SMD distribution among all three of the models. The minimum SMD, SMD_{min}, along the spray centerline was determined through a competition between

the primary atomization and subsequent droplet breakup length scales. As expected, the predicted SMD_{min} by the KH model scales with KH breakup scale (Λ_{KH}) across all injection and ambient conditions. However, even with the addition of a turbulence-induced primary atomization mechanism to the KH model, the droplet sizes formed from the KH-ACT primary atomization model were also observed to scales with Λ_{KH} across all injection and ambient conditions. This trends occurs because the turbulent breakup process as represented in the KH-ACT model creates droplets that are larger than Λ_{KH} in the near-nozzle region. These drops are therefore unstable and undergo subsequent KH droplet breakup, and scale with Λ_{KH}.

In contrast, the scaling of SMD_{min} predicted by the KH-Faeth model exhibits a dependence on ambient condition. For ρ_f/ρ_g less than 100, the turbulence-induced primary atomization process, as modeled with the Wu and Faeth correlations, produces droplets that are smaller than Λ_{KH}. As a result, these droplets are stable and SMD_{min} scales with the Faeth turbulent length scale correlation, as described in Equation 5.2. For ρ_f/ρ_g greater than 100, the turbulent primary atomization process produces droplets that are larger than Λ_{KH}. As a result, these droplets are unstable to KH instabilities and SMD_{min} ultimately scales with Λ_{KH}. Therefore, regardless of the primary atomization model employed, the centerline SMD distributions were predicted to be controlled by secondary droplet breakup in downstream portions of the spray under conditions where $\rho_f/\rho_g > 100$.

The response of the SMD measurements from USAXS to changes in injection and ambient conditions was evaluated to identify the potential spray and droplet breakup phenomena governing the measured SMD distribution along the spray centerline. The centerline SMD profile formed from the spray breakup process were found to be largely insensitive to changes in ambient density for $\rho_g \leq 2.4$ kg/m^3, suggesting that these conditions may exist within the non-aerodynamic primary breakup regime. Comparison between the predicted and measured sensitivities in-

dicated that the experimentally measured SMD along the spray centerline was not likely controlled by secondary breakup processes under low ambient density conditions ($\rho_f/\rho_g > 300$). Therefore, the critical ρ_f/ρ_g condition defining the transition between non-aerodynamic and aerodynamic primary breakup regimes may occur at a lower ρ_f/ρ_g threshold for diesel sprays ($\rho_f/\rho_g > 300$) than was observed for the ideal nozzles in the studies of Wu and co-workers ($\rho_f/\rho_g > 500$). However, the $\rho_f/\rho_g \sim 500$ condition defining the non-aerodynamic primary breakup regime boundary was acknowledged by Wu and Faeth to have some uncertainty, and that more experimental work was needed to better define the critical ρ_f/ρ_g condition [18]. Indeed, additional USAXS measurements conducted close to this transition region could help provide more information to confidently define the transition into non-aerodynamic primary breakup for diesel sprays.

The USAXS measurements conducted under $\rho_f/\rho_g > 300$ conditions were then directly compared with proposed scalings within the turbulence spectrum to evaluate potential length scales chararacterizing the droplet formation process. Using the turbulent breakup theory underpinning the Huh-Gosman and KH-ACT model, a theoretical relationship was derived to relate the characteristic turbulence length scale to ambient, injection and nozzle parameters. For a non-cavitating diesel spray, the turbulence length scale in the Huh-Gosman and KH-ACT model was found to be independent of injection and ambient conditions, and only a function of the nozzle geometry. In comparison to the USAXS measurements, the theoretical turbulence scaling suggested larger insensitivities with respect to changes in injection and ambient conditions than was experimentally observed. Therefore, it was determined that the integral scaling underpinning the Huh-Gosman and KH-ACT predictions is not likely able to characterize the turbulent primary atomization process in diesel sprays.

Using the empirical correlations from Wu and Faeth, a theoretical relationship between the characteristic turbulence length scale to ambient, injection and nozzle

parameters was also derived. The proposed turbulence length scale was found to be highly insensitive to changes in ambient density, but suggested a dependence on the fuel injection pressure that was observed to be consistent with the USAXS measurements. It was therefore concluded that the empirical correlations from Wu and Faeth may serve as a foundation for representing turbulent primary atomization in diesel sprays.

7.1.4 Recommendations for an Improved Hybrid Spray Breakup Model

Findings from the experimental and computational investigations presented in Chapters 4, 5, and 6 were synthesized to provide recommendations for an improved hybrid spray breakup model, capable of representing both aerodynamic and turbulent breakup mechanisms in diesel spray primary atomization. Recommendations for the hybrid spray breakup model were organized into two regimes, defined similarly as those proposed by Wu and Faeth: 1) non-aerodynamic primary breakup, where turbulence governs the primary atomization process in isolation, and 2) merged aerodynamic secondary and primary breakup, where aerodynamically-enhanced turbulent primary atomization is accompanied by aerodynamic secondary droplet breakup.

For conditions where ρ_f/ρ_g are approximately greater than 300, non-cavitating diesel sprays are proposed to undergo non-aerodynamic primary breakup. The size of primary droplets formed from this process are hypothesized to be determined by the characteristic length scale of turbulent eddies with sufficient energy to overcome surface tension energy at the liquid-gas interface. This characteristic turbulent length scale is defined using the empirical correlation developed by Wu and Faeth, as previously defined in Equation 5.2. The time required to form a droplet, τ_{Faeth}, scales with the time required for a droplet to form from a ligament of size L_{Faeth}, according to the Rayleigh instability mechanism, as defined in Equation 5.1. Analysis of the SMD measurements along the spray centerline did not indicate a strong influence of

secondary droplet breakup; as a result, secondary breakup is not recommended to be included in a spray model under such conditions. The definition for the boundary of the regime, and the recommended breakup length and time scales, can be assessed in further detail when additional droplet sizing measurement become available under $\rho_f/\rho_g \sim 300$ conditions.

For conditions where ρ_f/ρ_g are approximately less than 300, the primary breakup process for non-cavitating diesel sprays is proposed to be governed by both aerodynamic and turbulence-induced breakup mechanisms. As formulated in the newly developed KH-Faeth spray model, presented in Chapter 5, the competition between aerodynamic and turbulent breakup mechanisms in driving the droplet formation process is hypothesized to be determined by the mechanism with the fastest predicted breakup rate, similar to the KH-ACT formulation by Som and Aggarwal. To allow for continuous spray breakup behavior across the two regimes, the turbulent breakup process should be modeled consistently using the empirical correlations from Wu and Faeth for L_{Faeth} and τ_{Faeth}, as previously defined. Due to the demonstrated success of a well-calibrated KH primary breakup model in representing the spray structure under conventional diesel conditions, as discussed in Chapter 4, the aerodynamic breakup process is modeled using the KH spray model formulation from Beale and Reitz, as described in Section 1.2.3.1, where a primary droplet of size r_c is formed in a breakup timescale of τ_{KH}. As indicated in the modeling results in Chapter 4, the resultant spray structure was largely influenced by secondary breakup processes, and displayed good agreement with available experimental measurements when the droplet breakup process was modeled with the KH instability mechanism. As a result, for conditions where $\rho_f/\rho_g < 300$, it is recommended for spray models to include the effects of secondary droplet breakup as represented using the KH model.

7.2 Recommendations for Future Work

Recommendations are provided to extend the experimental and computational research presented in this thesis. These recommendations are organized into future experimental and computational investigations that can provide further insight into the relationship between internal nozzle flow development and spray formation processes, and how these physics should be represented within the spray modeling framework in current engine modeling packages.

7.2.1 Recommended Experimental Investigations

The SAMR technique demonstrated the ability to yield a measurement that quantifies the SMD within a probed measurement volume using joint x-ray radiography and laser extinction measurements. Although the laser extinction experimental set-up employed in this thesis ensures careful collection of the forward scattered light, the measurement technique is time-intensive as two-dimensional distributions of optical thickness are built up from succesive raster-scanned measurements. A promising alternative diagnostic that could accelerate the acquistion of two-dimensional distributions of optical thickness for use in the SAMR technique is diffused-back illumination (DBI), as previously descrcribed in Section 2.2.4.2. DBI quantifies transmission of light through the spray by illuminating the entire spray, as opposed to a small measurement volume. Processing of the DBI images yields a two-dimensional map of optical thickness, instead of a single point for laser extinction, which accelerates the data collection process and allows for higher spatial resolution of the spray. Preliminary comparison between the DBI and laser extinction measurements is shown in Figure 7.1. Although the comparison is conducted under a single condition, the consistent quantification of the transverse optical thickness profile provides encouragement that DBI can also be used with the SAMR technique for quantifying SMD

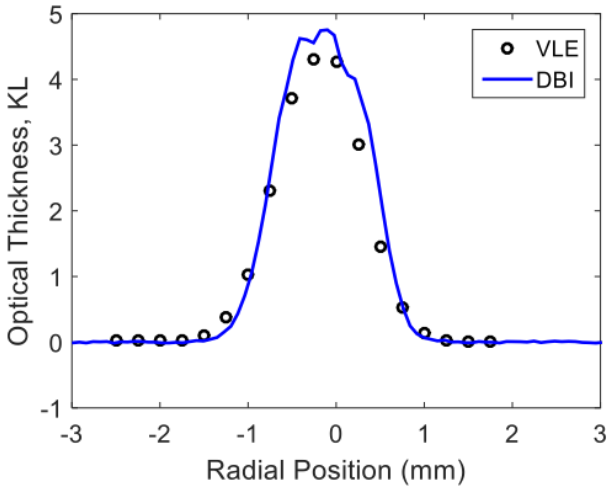

Figure 7.1: *Comparison between laser extinction measurements (VLE) and DBI extinction of Spray A under the Case 1 condition at an axial location of 7.5 mm from the injector tip. Overlap of data indicates consistent measurements.*

distributions.

Regardless if DBI or laser extinction measurements are employed for the SAMR technique, laser extinction, DBI and x-ray radiography measurements all represent path-integrated spray quantities. As a result, it is possible to extract additional information about the internal structure of the spray using computed tomography. Such information would be particularly useful for studying asymmetric or multi-hole sprays. A brief discussion is presented here on how tomography can be used to evaluate three-dimensional distributions of SMD within the spray from the SAMR measurement technique.

Generally speaking, tomographic reconstruction is the ability to estimate a field parameter from many independent line-of-sight measurements or projections of the field [146]. The elements of this reconstructed field are called voxels. For example, two-dimensional liquid volume fraction distributions can be reconstructed from several viewing angles of projected density measurements. For x-ray radiography measurements, these projections physically represent the projected distribution of mass at a given spray cross-section. In order to faithfully reconstruct a highly asymmetric

field, many projections are needed. It has been found that the number of viewing angles needed for an optimal tomographic reconstruction must be on the order of the spatial resolution of the measurement [147], which for the x-ray radiography technique can be as high as 100 viewing angles. This often makes high quality tomographic reconstruction infeasible, particularly for point-wise and raster-scanned measurements, due to the vast amount of resources needed.

However, if the spray is shown to be symmetric, the reconstruction of the spray is greatly simplified. For a symmetric object, field projections from all viewing angles are equal and an inverse Abel transform can be employed [146]. Although some accuracy and details may be lost in employing this simplification for a spray, it provides a way to estimate the salient internal spray features. Assuming that all projections of the spray field are identical, the Abel inversion can be used to reconstruct the spray mass distribution and light scattering field. By taking a ratio of the reconstructed measurements, and using the measurement ratio look up table shown in Figure 3.2, one can determine the two-dimensional distribution of SMD. It should be noted that evaluation of the internal structure will be limited due to the errors introduced from multiple scattering, which corrupt interpretation of the measured laser extinction measurement. Overall, employing computed tomography techniques to the SAMR measurement shows promise of providing three-dimensional information about the spray structure. Additionally, if the x-ray and visible extinction measurements are time-resolved, then tomographic reconstruction of the SAMR measurement technique could yield four-dimensional SMD fields, which characterize both the temporally and spatially evolving spray structure.

Future experimental campaigns should employ SAMR and other droplet sizing techniques in order to compile droplet sizing maps and further analyze the response of diesel spray structure to changes in injection and ambient conditions. For example, USAXS measurements presented in Chapter 4 for the ECN Spray A #210675 nozzle

at ρ_f/ρ_g conditions less than 100 showed good agreement with the minimum SMD predicted by the KH model. This agreement suggests that SMD_{min} scales with Λ_{KH} for ρ_f/ρ_g less than 100. However, additional measurements for the larger Spray D nozzle in this range of ρ_f/ρ_g would strengthen arguments for extending this observed scaling to other injectors.

Currently, there are no other SMD measurements for the ECN Spray A and Spray D injectors that can help validate the distinct two-dimensional behaviors observed in the model predictions presented in Chapter 5. However, there are several available experimental techniques that could provide valuable insight into the sensitivity of droplet size distributions in the peripheral regions of the spray to changes in injection and ambient conditions. For example, long distance microscopic imaging can quantify spatial and temporal distributions of droplet size along the periphery of the spray under certain limited conditions [58, 136]. Crua and co-workers have optimized their optical microscopy experimental set-up and have been able to achieve droplet size resolutions down to 2 μm. However, this technique may not be able to quantify droplet sizes for the Spray A nozzle at $\rho_f/\rho_g < 100$ conditions, where model predictions indicate the presence of droplets less than 2 μm along the periphery. However, this measurement technique shows promise of providing valuable information for higher ρ_f/ρ_g conditions for the Spray D nozzle, where droplet sizes along the periphery are predicted to be greater than 4 μm. Additional experimental techniques that can also quantify spatial distributions of the peripheral droplet size distribution are USAXS and SAMR, dual-wavelength extinction [148], and PDPA [61]. Experimental measurements conducted at ρ_f/ρ_g conditions greater than 100 would help address observed modeling discrepancies in the predicted response of SMD_{periph} to changes in ρ_f/ρ_g, P_{inj}, and nozzle diameter, as discussed in Chapter 5. Exploration of the measured sensitivity of peripheral droplet size distributions to changes in injection and ambient conditions would provide critical information in understanding the physics

governing the peripheral droplet size distribution.

Complementary to the peripheral droplet sizing measurements, measurements of the characteristic timescale or axial length of the primary atomization region would yield critical information regarding processes in the near nozzle region and its influence on the peripheral droplet size distribution. To date, there are no existing measurements that can quantify the primary atomization timescale for diesel-like sprays. However, there are some experimental techniques which show promise of characterizing the length of the primary atomization region through quantification of the dense liquid mass distribution expected in this region. In particular, application of computed tomography to x-ray radiography measurements would allow for the characterization of liquid volume fraction distributions, particularly in the dense regions of the spray. In recent work by Duke and co-workers, almost 100 different viewing angles were used to reconstruct the liquid volume fraction distribution of a multi-hole gasoline spray from the measured fuel mass density distributions [149]. As previously discussed, such a large number of viewing angles are required to characterize spray asymmetries and reduce the uncertainty in the computed tomographic reconstruction. For the ECN Spray A and Spray D single-hole injectors, it is likely that fewer viewing angles would be required to achieve adequate measurements of the liquid volume fraction distribution in the near nozzle region. However, to date, the maximum number of viewing angles for x-ray radiography has been limited for high-pressure fuel sprays; for the Spray A injector, the maximum number of reported viewing angles has been four [125]. As improvements are made to the x-ray radiography experimental set-up to optimize data acquisition for high-pressure fuel sprays, this type of measurement may become more feasible in providing such information about the internal structure of the near-nozzle region. Ultimately, experimental characterization of near-nozzle spray formation processes under engine-relevant conditions is necessary to improve understanding for how the spray breakup process should be

modeled.

7.2.2 Recommended Computational Investigations

The hybrid KH-Faeth model was presented in Chapter 5 in order to explore the influence of the assumed primary breakup length scale on the resultant predicted spray structure. Predicted sensitivities of the centerline SMD distribution were found to be inconsistent with experimentally observed sensitivites from available USAXS measurements, presented in Chapter 6, due to the inclusion of secondary droplet breakup physics in the model. Direct comparison between the scaling presented in the Wu and Faeth empirical correlation [18] and the centerline SMD data from USAXS supported the use of these correlations to describe the turbulent length scale characterizing the droplet formation process. In future spray modeling efforts with the KH-Faeth model, secondary drop breakup via the KH mechanism should be removed from the model under $\rho_f/\rho_g > 300$ conditions to validate the model formulation. Additionally, once more experimental data becomes available near the transition between the non-aerodynamic and aerodynamic primary breakup regimes, the ability of the KH-Faeth model to capture the relative influence of aerodynamics and nozzle-generated turbulence on the spray breakup process should be further validated.

This thesis focused on the relative contributions of nozzle-generated turbulence and the growth of aerodynamic induced instabilities to the atomization processes for diesel sprays. However, it is well known that other mechanisms, namely cavitation, influence the diesel spray formation process. This study did not consider the role of cavitation on the spray formation process. The challenge in fundamentally studying cavitation-induced breakup centers on the inability to isolate cavitation phenomenon when using realistic diesel injector geometries. Under conditions where turbulence-induced breakup was determined to be isolated from the influence of aerodynamics ($\rho_f/\rho_g > 300$), the joint role of cavitation and turbulence on the spray breakup process

can be evaluated in the future. More specifically, comparison of measured and predicted spray structure for the ECN Spray C and Spray D injectors could allow for the role of cavitation to be systematically investigated. The ECN Spray C and D injectors were designed to have similar injector geometries, with the only difference being the nozzle conicity, or K-factor. The Spray C injector was designed with a cylindrically-shaped nozzle to enhance the likelihood of cavitation inception, whereas the Spray D injector was designed with a converging nozzle profile. Comparison of the resultant spray structure from the Spray C and D injectors within the non-aerodynamic primary breakup regime would provide the ideal set of conditions to evaluate the assumed scalings within existing cavitation-induced breakup formulations.

REFERENCES

[1] United States Environmental Protection Agency, EPA420-F-03-022, *Fact sheet: diesel exhaust in the United States*, 2003.

[2] C. Genzale, L. Pickett, and S. Kook, "Liquid penetration of diesel and biodiesel sprays at late-cycle post-injection conditions," *SAE International Journal of Engines*, vol. 3, no. 1, p. 479, 2010.

[3] L. Pickett and S. Kook, "Transient liquid penetration of early-injection diesel sprays," *International Journal of Engines*, vol. 4970, 2009.

[4] J. Kodavasal, C. Kolodziej, S. Ciatti, and S. Som, "Cfd simulation of gasoline compression ignition," in *ASME 2014 Internal Combustion Engine Division Fall Technical Conference*, pp. V002T06A008–V002T06A008, American Society of Mechanical Engineers, 2014.

[5] A. B. Dempsey, S. J. Curran, and R. M. Wagner, "A perspective on the range of gasoline compression ignition combustion strategies for high engine efficiency and low nox and soot emissions: Effects of in-cylinder fuel stratification," *International Journal of Engine Research*, 2016.

[6] D. L. Siebers, "Scaling liquid-phase fuel penetration in diesel sprays based on mixing-limited vaporization," *SAE*, vol. 01-0528, no. 724, 1999.

[7] D. Siebers, "Liquid-phase fuel penetration in diesel sprays," *SAE Paper 980809*, 1998.

[8] V. A. Iyer, S. L. Post, and J. Abraham, "Is the liquid penetration in diesel sprays mixing controlled?," *Proceedings of the Combustion Institute*, vol. 28, pp. 1111–1118, jan 2000.

[9] R. D. Reitz and R. Diwakar, "Structure of high-pressure fuel sprays," tech. rep., SAE Technical Paper, 1987.

[10] J. K. Dukowicz, "A particle-fluid numerical model for liquid sprays," *Journal of Computational Physics*, vol. 35, no. 2, pp. 229–253, 1980.

[11] A. A. Amsden, P. O'Rourke, and T. Butler, "Kiva-ii: A computer program for chemically reacting flows with sprays," technical report la-11560-ms, Los Alamos National Laboratory, 1989.

[12] Fluent, *FLUENT 6.2 User's Guide*, 2005.

[13] K. Richards, P. Senecal, and E. Pomraning, *CONVERGE 2.1. 0 Theory Manual, Convergent Science*, 2013.

[14] H. Weller, G. Tabor, H. Jasak, and C. Fureby, "A tensorial approach to cfd using object oriented techniques," *Computers in Physics*, vol. 12, no. 6, p. 620, 1998.

[15] R. Reitz and F. Bracco, "Mechanism of atomization of a liquid jet," *The Physics of Fluids*, vol. 25, no. 10, pp. 1730–1742, 1982.

[16] R. D. Reitz, "Modeling atomization processes in high pressure vaporizing sprays," *Atomization & Spray Technology*, vol. 3, no. 4, pp. 309–337, 1987.

[17] J. C. Beale and R. D. Reitz, "Modeling spray atomization with the kelvin-helmholtz/rayleigh-taylor hybrid model," *Atomization and*, vol. 9, pp. 623–650, 1999.

[18] P.-K. Wu and G. Faeth, "Aerodynamic effects of primary breakup of turbulent liquids," *Atomization and Sprays*, vol. 3, no. 3, pp. 265–289, 1993.

[19] "Sphere lab homepage." http://www.spherelab.gatech.edu, November 2012.

[20] V. Levich, *Physicochemical Hydrodynamics*. Prentice Hall, 1962.

[21] A. Sterling and C. Sleicher, "The instability of capillary jets," *Journal of Fluid Mechanics*, vol. 68, p. 477, 1975.

[22] W. Rayleigh, "On the instability of jets," *Proceedings of London Mathematical Society*, vol. 4, 1878.

[23] C. Weber, "On the breakdown of a fluid jet," *Z.A.M.P.*, vol. 11, p. 136, 1931.

[24] R. Grant and S. Middleman, "Newtonian jet stability," *A.I.Ch.E.*, vol. 12, 1966.

[25] A. Haenlein, "On the disruption of a liquid jet," *N.A.C.A. TM. 659*, 1932.

[26] V. Borodin and Y. Dityakin, "Unstable capillary waves on surface of separation of two viscous liquids," *N.A.C.A. TM.*, 1951.

[27] R. Castleman, "Mechanism of atomization accompanying solid injection," *N.A.C.A. Report 440*, 1932.

[28] R. A. Castleman, *The mechanism of the atomization of liquids*. US Department of Commerce, Bureau of Standards, 1931.

[29] R. Reitz, *Atomization and other breakup regimes of a liquid jet*. PhD thesis, Princeton University, 1978.

[30] P. G. Drazin and W. H. Reid, *Hydrodynamic stability*. Cambridge university press, 2004.

[31] R. D. Reitz and F. Bracco, "Mechanisms of breakup of round liquid jets," *Encyclopedia of fluid mechanics*, vol. 3, pp. 233–249, 1986.

[32] E. Giffen and A. Muraszew, *The Atomization of Liquid Fuels*. John Wiley and Sons, 1970.

[33] W. Bergwerk, "Flow pattern in diesel nozzle spray holes," *Proceedings of Institution of Mechanical Engineers*, vol. 173, p. 655, 1959.

[34] R. Sadek, "Communication to bergwerk," *Proceedings of the Institution of Mechanical Engineers*, vol. 173, 1959.

[35] J. Rupe, "On the dynamic characteristics of free-liquid jets and a partial correlation with orifice geometry," *J.P.L. Technical Report No. 32*, 1962.

[36] P. Hooper and P. Eisenklam, "Ministry of supply dggw report," *EMR/58/JRL/42*, 1958.

[37] M. McCarthy and N. Molloy, "Review of stability of liquid jets and the influence of nozzle design," *The Chemical Engineering Journal*, vol. 7, 1974.

[38] K. DeJuhasz, "Dispersion of sprays in solid injection oil engines," *Transactions of American Society of Mechanical Engineers*, vol. 53, 1931.

[39] P. Schweitzer, "Mechanism of disintegration of liquid jets," *Journal of Applied Physics*, vol. 8, 1937.

[40] G. Sitkei, "On the theory of jet atomization," *Acta Tech. Acad. Sci. Hungaricae*, vol. 25, 1959.

[41] W. Ranz, "On sprays and spraying," *Department of Engineering Research Penn State University Bulletin*, 1956.

[42] S. Som and S. Aggarwal, "Effects of primary breakup modeling on spray and combustion characteristics of compression ignition engines," *Combustion and Flame*, vol. 157, pp. 1179–1193, June 2010.

[43] K. Huh, E. Lee, and J. Koo, "Diesel spray atomization model considering nozzle exit turbulence conditions," *Atomization and Sprays*, vol. 8, no. 4, pp. 453–469, 1998.

[44] K. Y. Huh and A. Gosman, "A phenomenological model of diesel spray atomization," in *Multiphase Flows*, (Tsukuba, Japan), 1991.

[45] S. Som, *Development and Validation of Spray Models for Investigating Diesel Engine Combustion and Emissions*. PhD thesis, University of Illinois at Chicago, 2009.

[46] J. Taylor and J. Hoyt, "Water jet photography-techniques and methods," *Experiments in Fluids*, vol. 1, no. 3, pp. 113–120, 1983.

[47] G. Faeth, L.-P. Hsiang, and P.-K. Wu, "Structure and breakup properties of sprays," *International Journal of Multiphase Flow*, vol. 21, pp. 99–127, 1995.

[48] D. Lee and R. Spencer, "Photomicrographic studies of fuel sprays," *N.A.C.A. Report No. 454*, 1933.

[49] P.-K. Wu, L.-K. Tseng, and G. Faeth, "Primary breakup in gas/liquid mixing layers for turbulent liquids," *Atomization and Sprays*, vol. 2, pp. 295–317, 1992.

[50] P.-K. Wu, R. Mirand, and G. Faeth, "Effects of initial flow conditions on primary breakup of nonturbulent and turbulent round liquid jets," *Atomization and Sprays*, vol. 5, pp. 175–196, 1995.

[51] B. Munson, T. Okiishi, W. Huebsch, and A. Rothmayer, *Fundamentals of Fluid Mechanics*. Hoboken, NJ: John Wiley & Sons, 2013.

[52] A. L. Kastengren, F. Z. Tilocco, C. F. Powell, J. Manin, L. M. Pickett, R. Payri, and T. Bazyn, "Engine combustion network (ecn): Measurements of nozzle geometry and hydraulic behavior," *Atomization and Sprays*, vol. 22, no. 12, pp. 1011–1052, 2012.

[53] C. Dumouchel, "On the experimental investigation on primary atomization of liquid streams," *Experiments in Fluids*, vol. 45, pp. 371–422, jun 2008.

[54] T. Karasawa, M. Tanaka, K. Abe, S. Shiga, and T. Kuruabayashi, "Effect of nozzle configuration on the atomization of a steady spray," *Atomization and Sprays*, vol. 2, pp. 411–426, 1992.

[55] N. Tamaki, M. Shimizu, K. Nishida, and H. Hiroyasu, "Effects of cavitation and internal flow on atomization of a liquid jet," *Atomization and Sprays*, vol. 8, pp. 179–197, 1998.

[56] W. Merzkirch, "Shadowgraph technique." http://www.thermopedia.com/content/1117/, Feb 2011.

[57] G. Borenstein, "The more pixels law: Gigapixel cameras and the 21st century reality effect." http://makematics.com/drafts/more_pixels_law.html, 2012.

[58] C. Crua, M. Heikal, and M. Gold, "Microscopic imaging of the initial stage of diesel spray formation," *Fuel*, vol. 157, pp. 140–150, 2015.

[59] H. Zaheer, "Transient microscopy of primary atomization in gasoline direct injection sprays," Master's thesis, Georgia Institute of Technology, 2015.

[60] T. Behrendt, M. Carl, J. Heinze, and C. Hassa, "Optical measurements of the reacting two-phase flow in a realistic gas turbine combustor at elevated pressures," *Atomization and Sprays*, vol. 16, no. 5, 2006.

[61] V. T. Soare, *Phase Doppler Measurements in Diesel Dense Sprays: Optimisation of Measurements and Study of the Orifice Geometry Influence over the Spray at Microscopic Level.* PhD thesis, Universidad Politecnica de Valencia, 2007.

[62] F. Payri, J. V. Pastor, R. Payri, and J. Manin, "Determination of the optical depth of a di diesel spray," *Journal of Mechanical Science and Technology*, vol. 25, pp. 209–219, mar 2011.

[63] J. Pastor, R. Payri, J. Salavert, and J. Manin, "Evaluation of natural and tracer fluorescent emission methods for droplet size measurements in a diesel spray," *International Journal of Automotive Technology*, vol. 13, no. 5, pp. 713–724, 2012.

[64] A. Kastengren, J. Ilavskya, J. P. Vierab, R. Payri, D. Duke, A. Swantek, F. Z. Tiloccoc, N. Sovis, and C. Powell, "Measurements of droplet size in shear-driven atomization using ultra small angle x-ray scattering," *International Journal of Mulitphase Flows*, 2017.

[65] C. Powell, D. Duke, A. Kastengren, and J. Ilavsky, "Measurements of diesel spray droplet size with ultra-small angle x-ray scattering," in *25th ILASS-Americas conference, Pittsburgh, PA*, 2013.

[66] A. Munnannur, *Droplet Collision Modeling in Multi-Dimensional Engine Spray Computations*. PhD thesis, University of Wisconsin-Madison, 2007.

[67] J. Wang, "X-ray vision of fuel sprays," *Journal of synchrotron radiation*, vol. 12, no. 2, pp. 197–207, 2005.

[68] Y. Yue, C. F. Powell, R. Poola, J. Wang, and J. K. Schaller, "Quantitative measurements of diesel fuel spray characteristics in the near-nozzle region using x-ray absorption," *Atomization and sprays*, vol. 11, no. 4, 2001.

[69] W. Ning, *Development of a next-generation spray and atomization model using an Eulerian-Lagrangian methodology*. PhD thesis, University of Wisconsin-Madison, 2007.

[70] A. Liu, D. Mather, and R. Reitz, "Modeling the effects of drop drag and breakup on fuel sprays," *SAE Paper 930072*, 1993.

[71] S.-C. Kong, Z. Han, and R. Reitz, "The development and application of a diesel ignition and combustion model for multidimensional engine simulations," *SAE Paper 950278*, 1995.

[72] J. Eckhause and R. Reitz, "Modeling heat transfer to impinging fuel sprays in direct injection engines," *Atomization and Sprays*, 1995.

[73] M. Patterson, S.-C. Kong, G. Hampson, and R. Reitz, "Modeling the effects of fuel injection characteristics on diesel engine soot and nox emissions," *SAE Paper 940523*, 1994.

[74] S. Som and S. K. Aggarwal, "Assessment of atomization models for diesel engine simulations," *Atomization and Sprays*, vol. 19, no. 9, pp. 885–903, 2009.

[75] Q. Xue, M. Battistoni, S. Som, S. Quan, P. Senecal, E. Pomraning, and D. Schmidt, "Eulerian cfd modeling of coupled nozzle flow and spray with validation against x-ray radiography data," *SAE International Journal of Engines*, vol. 7, no. 2014-01-1425, pp. 1061–1072, 2014.

[76] M. Bode, F. Diewald, D. O. Broll, J. F. Heyse, and V. L. Chenadec, "Influence of the injector geometry on primary breakup in diesel injector systems," *SAE Technical Paper*, no. 2014-01-1427, 2014.

[77] R. Reitz and F. B. Bracco, "On the dependence of spray angle and other spray parameters on nozzle design and operating conditions," in *SAE Technical Paper Series*, 1979.

[78] H. Hiroyasu and T. Kadota, "Fuel droplet size distribution in diesel combustion chamber," *SAE Technical Paper 740715*, 1974.

[79] A. Yule, S. Mo, S. Tham, and S. Aval, "Diesel spray structure," *Proceedings of the Third International Conference on Liquid Atomization and Spray Systems*, 1985.

[80] S. Som, A. Amirez, S. Aggarwal, and e. a. A.L. Kastengren, "Development and validation of a primary breakup model for diesel engine applications," *SAE Technical Paper 2009-01-0838*, 2009.

[81] F. Payri, V. Bermúdez, R. Payri, and F. Salvador, "The influence of cavitation on the internal flow and the spray characteristics in diesel injection nozzles," *Fuel*, vol. 83, pp. 419–431, mar 2004.

[82] D. P. Schmidt, *Cavitation in Diesel Fuel Injector Nozzles*. PhD thesis, University of Wisconsin - Madison, 1997.

[83] G. M. Magnotti and C. L. Genzale, "A novel approach to assess diesel spray models using joint visible and x-ray liquid extinction measurements," *SAE International Journal of Fuels and Lubricants*, vol. 8, no. 2015-01-0941, pp. 167–178, 2015.

[84] G. M. Magnotti and C. L. Genzale, "A novel spray model validation methodology using liquid-phase extinction measurements," *Atomization and Sprays*, vol. 25, no. 5, 2015.

[85] G. M. Magnotti and C. L. Genzale, "Characterization of diesel spray breakup using visible and x-ray extinction measurements," in *ILASS Americas 28th Annual Conference*, (Dearborn, MI), May 2016.

[86] G. M. Magnotti and C. L. Genzale, "Detailed assessment of diesel spray atomization models using visible and x-ray extinction measurements," *International Journal of Multiphase Flow*, Under Review.

[87] G. M. Magnotti, K. E. Matusik, D. J. Duke, B. W. Knox, G. L. Martinez, C. F. Powell, A. L. Kastengren, and C. L. Genzale, "Modeling the influence of nozzle-generated turbulence on diesel sprays," in *ILASS Americas 29th Annual Conference*, (Atlanta, GA), May 2017.

[88] G. M. Magnotti and C. L. Genzale, "Exploration of turbulent atomization mechanisms for diesel spray simulations," in *Proceedings of the 2017 SAE World Congress*, (Detroit, MI), April 2017.

[89] Q. Xue, "Spray in automotive applications: Part i," *Atomization and Sprays*, 2015.

[90] E. Pomraning, K. Richards, and P. Senecal, "Modeling turbulent combustiong using a rans model, detailed chemistry, and adaptive mesh refinement," *SAE Technical Paper 2014-01-1116*, 2014.

[91] S. B. Pope, *Turbulent Flows*. Cambridge University Press, 2000.

[92] H. Versteeg and W. Malalasekera, *An Introduction to Computational Fluid Dynamics: The Finite Volume Method*. Pearson Education Limited, 2007.

[93] C. Rutland, "Large-eddy simulations for internal combustion engines – a review," *International Journal of Engine Research*, 2011.

[94] K. Matusik, D. Duke, A. Swantek, C. Powell, and A. Kastengren, "High resolution x-ray tomography of injection nozzles," in *28th ILASS-Americas Conference, Dearborn, MI*, 2016.

[95] P. Senecal, S. Mitra, E. Pomraning, Q. Xue, S. Som, S. Banerjee, B. Hu, K. Liu, D. Rajamohan, and J. Deur, "Modeling fuel spray vapor distribution with large eddy simulation of multiple realizations," *Journal of Engineering for Gas Turbine and Power*, 2015.

[96] C. Hawbchi and G. Bruneaux, "Les and experimental investigation of diesel sprays," in *Triennial International Conference on Liquid Atomization and Spray Systems*, (Heidelberg, Germany), 2012.

[97] Q. Xue, M. Battistoni, C. F. Powell, S. Quan, E. Pomraning, P. Senecal, D. P. Schmidt, and S. Som, "An eulerian cfd model and x-ray radiography for coupled nozzle flow and spray in internal combustion engines," *International Journal of Multiphase Flows*, 2015.

[98] S. Pope, "An explanation of the turbulent round-jet/plane-jet anomaly," *AIAA Journal*, 1978.

[99] F. Williams, *Combustion Theory*. Menlo Park, CA: The Benjamin/Cummings Publishing Company, 1985.

[100] H. Gupta and F. Bracco, "Numerical computations of two-dimensional unsteady sprays for application to engines," *AIAA Journal*, 1978.

[101] S. Subramaniam, "Lagrangian-eulerian methods for multiphase flows," *Prog. Energy Combust. Sci*, vol. 39, pp. 215–245, 2013.

[102] P. Senecal, E. Pomraning, K. Richards, and S. Som, "Grid-convergent spray models for internal combustion engine computational fluid dynamics simulations," *Journal of Energy Resources Technology*, vol. 136, no. 1, 2014.

[103] D. P. Schmidt and F. Bedford, "An analysis for the convergence of stochastic lagrangian/eulerian spray simulations," in *29th ILASS-Americas Conference, Atlanta, GA*, 2017.

[104] S. Subramaniam and P. O'Rourke, "Numerical convergence of the kiva-3 code for sprays and its implications for modeling," technical report ur-98-5465, Los Alamos National Laboratory, 1998.

[105] P. O'Rourke and A. Amsden, "The tab method for numerical calculation of spray droplet breakup," *SAE Paper No. 872089*, 1987.

[106] W. A. Sirignano, *Fluid Dynamics and Transport of Droplets and Sprays*. Cambridge University Press, 2010.

[107] P. O'Rourke and F. Bracco, "Modeling of drop interactions in thick sprays and a comparison with experiments," in *I Mech E*, vol. 9, pp. 101–116, 1980.

[108] J. Qian and C. Law, "Regimes of coalescence and separation in droplet collision," *Journal of Fluid Mechanics*, vol. 331, no. 1, pp. 59–80, 1997.

[109] S. Post and J. Abraham, "Modeling the outcome of drop-drop collisions in sprays," *International Journal of Multiphase Flows*, vol. 28, 2002.

[110] NIST, "Thermophysical properties of dodecane." http://webbook.nist.gov/cgi/fluid.cgi?ID=C112403&Action=Page.

[111] J. Kim, K. Nishida, and H. Hiroyasu, "Characteristics of the internal flow in a diesel injection nozzle," *Proceedings of ICLASS 1997*, 1997.

[112] D. Duke, A. Swantek, F. Tilocco, and A. K. et al., "X-ray imaging of cavitation in diesel injectors," *SAE International Journal of Engines*, vol. 7, no. 2, pp. 1003–1016, 2014.

[113] Engine Combustion Network, "Engine combustion network experimental data archive." http://www.sandia.gov/ECN.

[114] R. Payri, F. Salvador, J. Gimeno, and G. Bracho, "A new methodology for correcting the signal cumulative phenomenon on injection rate measurements," *Experimental Techniques*, vol. 32, no. 1, pp. 46–49, 2008.

[115] A. Kastengren, C. Powell, D. Arms, E. Dufresne, H. Gibson, and J. Wang, "The 7bm beamline at the aps: a facility for time-resolved fluid dynamics measurements," *Journal of Synchrotron Radiation*, vol. 19, no. 4, 2012.

[116] A. Kastengren, C. Powell, T. Riedel, S.-K. Cheong, K.-S. Im, X. Liu, Y. Wang, and J. Wang, "Nozzle geometry and injection duration effects on diesel sprays measured by x-ray radiography," *J. Fluids Eng.*, vol. 130, no. 4, 2008.

[117] A. Kastengren, F. Tilocco, D. Duke, C. Powell, X. Zhang, and S. Moon, "Time-resolved x-ray radiography of sprays from engine combustion network spray a diesel injectors," *Atomization and Sprays*, vol. 24, no. 3, pp. 251–272, 2014.

[118] A. Kastengren and C. Powell, "Synchrotron x-ray techniques for fluid dynamics," *Experiments in Fluids*, vol. 55, no. 3, 2014.

[119] J. Ilavsky, P. Jemian, A. Allen, F. Zhang, L. Levine, and G. Long, "Ultra-small-angle x-ray scattering at the advanced photon source," *Journal of Applied Crystallography*, 2009.

[120] J. Ilavsky and P. Jemian, "Irena: tool suite for modeling and analysis of small-angle scattering," *Journal of Applied Crystallography*, vol. 42, no. 2, pp. 347–353, 2009.

[121] B. W. Knox, *End-of-injection effects on diesel spray combustion.* PhD thesis, Georgia Institute of Technology, 2016.

[122] B. W. Knox, M. J. Franze, and C. L. Genzale, "Diesel spray rate-of-momentum measurement uncertainties and diagnostic considerations," *ASME J. Eng. Gas Turbines Power*, vol. 138, no. 3, 2016.

[123] M. Meijer, B. Somers, J. Johnson, J. Naber, S.-Y. Lee, L. M. Malbec, G. Bruneaux, L. M. Pickett, M. Bardi, R. Payri, and T. Bazyn, "Engine com-

bustion network (ECN): Characterization and comparison of boundary conditions for different combustion vessels," *Atomization and Sprays*, vol. 22, no. 9, pp. 777–806, 2012.

[124] J. Manin, M. Bardi, and L. M. Pickett, "Evaluation of the liquid length via diffused back-illumination imaging in vaporizing diesel sprays," in *Proceedings of COMODIA*, 2012.

[125] L. M. Pickett, J. Manin, A. Kastengren, and C. Powell, "Comparison of near-field structure and growth of a diesel spray using light-based optical microscopy and x-ray radiography," *SAE International Journal of Engines*, vol. 7, no. 2014-01-1412, pp. 1044–1053, 2014.

[126] L. M. Pickett, C. L. Genzale, and J. Manin, "Uncertainty quantification for liquid penetration of evaporating sprays at diesel-like conditions," *Atomization and Sprays*, vol. 25, no. 5, 2015.

[127] H. C. van de Hulst, *Light Scattering By Small Particles*. Dover Publications, 1981.

[128] M. Musculus and L. Pickett, "Diagnostic considerations for optical laser-extinction measurements of soot in high-pressure transient combustion environments," *Combustion and Flame*, vol. 141, no. 4, pp. 371–391, 2005.

[129] F. Westlye, K. Penney, S. Skeen, J. Manin, L. Pickett, and A. Ivarsson, "Diffuse back-light illumination setup for high temporal resolution extinction imaging," *Applied Optics*, vol. Submitted, 2016.

[130] J. Falcone, B. Knox, and C. Genzale, "Identifying uncertainties in diesel spray rate-of-momentum transients under elevated back pressure," in *ASME 2015 Internal Combustion Engine Division Fall Technical Conference*, 2015.

[131] Centro Motores Térmicos, "Virtual injection rate generator." http://www.cmt.upv.es/ECN03.aspx#model.

[132] G. L. Martinez, G. M. Magnotti, B. W. Knox, K. E. Matusik, D. J. Duke, A. L. Kastengren, C. F. Powell, and C. L. Genzale, "Quantification of sauter mean diameter in diesel sprays using scattering-absorption extinction measurements," in *ILASS Americas 29th Annual Conference*, (Atlanta, GA), May 2017.

[133] E. Berrocal, D. L. Sedarsky, M. E. Paciaroni, I. V. Meglinski, and M. a. Linne, "Laser light scattering in turbid media Part I: Experimental and simulated results for the spatial intensity distribution.," *Optics express*, vol. 15, pp. 10649–65, aug 2007.

[134] X. Margot, R. Payri, A. Gil, M. Chavez, and A. Pinzello, "Combined cfd-phenomenological approach to the analysis of diesel sprays under non-evaporative conditions," *SAE Technical Paper 2008-01-0962*, 2008.

[135] P. Laven, "MiePlot." http://www/philiplaven.com/mieplot.htm.

[136] C. Crua, M. Heikal, and M. Gold, "Dropsizing of near-nozzle diesel and rme sprays by microscopic imaging," in *12th Triennial International Conference on Liquid Atomization and Spray Systems*, (Heidelberg, Germany), 2012.

[137] T. Lucchini, G. D'Errico, and D. Ettorre, "Numerical investigation of the spray-mesh-turbulence interactions for high-pressure, evaporating sprays at engine conditions," *International Journal of Heat and Fluid Flow*, vol. 32, no. 1, 2011.

[138] C. Baumgarten, *Mixture Formation in Internal Combustion Engines*. Heidelberg: Springer, 2006.

[139] R. Payri, J. Gimeno, J. Cuisano, and J. Arco, "Hydraulic characterization of diesel engine single-hole injectors," *Fuel*, vol. 180, pp. 357–366, 2016.

[140] L. Pickett, C. Genzale, G. Bruneaux, and e. a. L. Malbec, "Comparison of diesel spray combustion in different high-temperature, high-pressure facilities," *SAE Int. J. Engines*, vol. 3, no. 2, pp. 156–181, 2010.

[141] R. Tatschl, C. v. Künsberg-Sarre, and B. v. Eberhard, "Ic-engine spray modeling – status and outlook," in *International Multidimensional Engine Modeling User's Group Meeting at the SAE Congress*, (Detroit, MI), 2002.

[142] D. Schmidt and M. Corradini, "The internal flow of diesel fuel injector nozzles; a review," *International Journal of Engine Research*, vol. 2, no. 1, 2001.

[143] W. Nurick, "Orifice cavitation and its effects on spray mixing," *Journal of Fluids Engineering*, vol. 98, 1976.

[144] G. Ruff, A. Sagar, and G. Faeth, "Structure of the near-injector region of pressure-atomized sprays," *AIAA J.*, vol. 27, pp. 549–559, 1987.

[145] H. Tennekes and J. Lumley, *A First Course in Turbulence*. M.I.T. Press, 1972.

[146] G. T. Herman, *Fundamentals of computerized tomography: image reconstruction from projections*. Springer Science & Business Media, 2009.

[147] A. C. Kak and M. Slaney, *Principles of computerized tomographic imaging*. IEEE, 1988.

[148] J. Labs and T. Parker, "Two-dimensional droplet size and volume fraction distribution from the near-injector region of high-pressure diesel sprays," *Atomization and Sprays*, vol. 16, no. 7, pp. 843–855, 2006.

[149] P. Strek, D. Duke, and e. a. A. Kastengren, "X-ray radiography and cfd studies of the spray g injector," *SAE Technical Paper 2016-01-0858*, 2016.